Thesis for the degree of Doctorate of Philosophy

Microstructure and high temperature properties of $Mo(Si,Al)_2$

- The effect of particle strengthening and alloying

AINA EDGREN

Department of Physics

Chalmers University of Technology

Gothenburg, Sweden 2024

Microstructure and high temperature properties of $Mo(Si,Al)_2$
- The effect of particle strengthening and alloying
AINA EDGREN
ISBN 978-91-8103-013-6

Acknowledgements, dedications, and similar personal statements in this thesis, reflect the author's own views.

Doktorsavhandlingar vid Chalmers tekniska högskola
Ny serie nr 5471
ISSN0346-718X

Department of Physics
Chalmers University of Technology
SE-412 96 Gothenburg
Sweden
Telephone + 46 (0)72-231 9801

Cover: From left to right, top to bottom: Backscatter electron (BSE) image, electron backscatter diffraction (EBSD) grain reference orientation deviation (GROD) map, energy dispersive X-ray spectroscopy (EDS) map, EBSD phase map, EBSD grain orientation spread (GOS) map, and electron probe microanalysis/wavelength dispersive spectroscopy (EPMA/WDS) Al map, of $Mo(Si,Al)_2$-based materials. For scale bars and colour interpretations, see Figures 5.20, 5.6, 5.20, 5.10(b), 5.5(b), and 5.18(c), respectively.

Printed by Chalmers Reproservice
Gothenburg, Sweden 2024

Microstructure and high temperature properties of $Mo(Si,Al)_2$
- The effect of particle strengthening and alloying

AINA EDGREN
Department of Physics
Chalmers University of Technology

Abstract

High temperature heating processes within the steel industries result in significant emissions of CO_2, primarily due to the combustion of fossil fuels. Electrification of these processes, such as through the implementation of resistive heating elements, holds great promise for reducing emissions. However, a bottleneck in the transition to a more environmentally friendly industry is related to the materials used for these heating elements.

$Mo(Si,Al)_2$ is a ceramic material commonly used for heating elements in various high temperature furnaces and is being considered for large-scale industrial-scale applications. While its oxidation properties have been extensively studied, its mechanical properties, which are crucial when increasing the size of the heating elements, have received limited attention. In this thesis, the high temperature deformation behaviour of $Mo(Si,Al)_2$-based materials, and potential routes for their improvement, have been investigated.

This work has shown that diffusion-driven grain boundary sliding is the main deformation mechanism in polycrystalline $Mo(Si,Al)_2$, particularly in fine-grained materials. In coarse-grained materials, the slip of dislocations also contributes to deformation. Moreover, coarse-grained $Mo(Si,Al)_2$ relaxes through the formation of low-angle grain boundaries and dynamic recrystallization. The addition of Al_2O_3 particles, to achieve particle strengthening, results in a competition between a negative effect from grain refinement at low fractions (up to 15 wt.%), and a positive effect from inhibition of grain boundary sliding at higher fractions.

Also alloying with W, Nb, Ta, and V has been studied, among which W was the most promising alternative. The solid solubility of W in $Mo(Si,Al)_2$ was high, and it also led to a slight improvement in high temperature strength. The solubility of the alloying elements Nb, Ta, and V was found to be low in $Mo(Si,Al)_2$. Instead, these elements were enriched in secondary phases. Additionally, Y alloying has been explored to investigate its effect on oxidation behaviour. However, the oxide adhesion was adversely affected.

Keywords: $Mo(Si,Al)_2$, high temperature mechanical properties, particle strengthening, alloying, microstructure, oxidation

Preface

The research work presented in this Doctoral thesis was carried out in the Division of Microstructure Physics at the Department of Physics, Chalmers University of Technology, during the time period October 2019 - March 2024, under the supervision of Docent Magnus Hörnqvist Colliander (Chalmers University of Technology) and Doctor Erik Ström (Kanthal AB).

This research was funded by the Swedish Foundation for Strategic Research (SSF) and Kanthal AB, through the industrial PhD student grant ID18-0064.

Appended papers

This thesis is based on the work contained in the following papers:

I. *High temperature deformation of polycrystalline C40 $Mo(Si,Al)_2$*
Aina Edgren, Erik Ström, Lars Frisk, Farid Akhtar, Magnus Hörnqvist Colliander
Materials Science & Engineering A 849 (2022) 143387

II. *High temperature compression of $Mo(Si,Al)_2$-Al_2O_3 composites*
Aina Edgren, Erik Ström, Lars Frisk, Farid Akhtar, Magnus Hörnqvist Colliander
Materials Science & Engineering A 865 (2023) 144583

III. *Competing deformation mechanisms in $Mo(Si,Al)_2$-Al_2O_3 composites*
Aina Edgren, Erik Ström, Magnus Hörnqvist Colliander
Submitted to Metallurgical and Materials Transactions

IV. *Alloying of C40-structured $Mo(Si,Al)_2$ with Nb, Ta and V*
Aina Edgren, Erik Ström, Anand Rajagopal, Magnus Hörnqvist Colliander
Materials Letters 353 (2023) 135219

V. *Influence of Yttrium Doping on the Oxidation of $Mo(Si,Al)_2$ in Air at 1500 °C*
Aina Edgren, Lars-Gunnar Johansson, Erik Ström, Magnus Hörnqvist Colliander
Oxidation of Metals 98 (2022) 415–427

My contributions to the appended papers

I. I synthesised the $Mo(Si,Al)_2$ material and prepared the specimens. I developed, conducted and analysed the high temperature compression tests with assistance from Dr. Farid Akhtar and Lars Frisk. I performed the microstructure analysis. I am the principal author.

II. I synthesised the $Mo(Si,Al)_2$-Al_2O_3 composites and prepared the specimens. I developed, conducted and analysed the high temperature compression tests with assistance from Dr. Farid Akhtar and Lars Frisk. I performed the microstructure analysis. Docent Magnus Hörnqvist Colliander performed the COMSOL analysis. I am the principal author.

III. I synthesised the $Mo(Si,Al)_2$-Al_2O_3 composites and performed the microstructural analysis. I performed the analysis of the four-point bending data. I am the principal author.

IV. I performed the microstructural analyses using SEM and SXRD. Dr. Anand Rajagopal performed the EPMA/WDS measurements and I analysed the results. I am the principal author.

V. I performed the oxidation exposures and the microstructural analyses using SEM and XRD. Ren Qiu performed the STEM analysis. I am the principal author.

Contents

CHAPTER 1

Introduction

1.1 A very short summary of the thesis

In this doctoral thesis, molybdenum aluminosilicide ($Mo(Si,Al)_2$) has undergone a comprehensive investigation to enhance our understanding of the ceramic material. The effect of alloying and particle strengthening on the microstructure, high temperature deformation behaviour, and oxidation properties have been evaluated. These findings are important for advancing the development of new and improved $Mo(Si,Al)_2$ products, which are crucial to reducing greenhouse gas emissions from industrial heating processes. This first chapter aims to give a short background to the topic as well as present the important research questions that form the focus of this thesis.

1.2 The need for electrification of industrial processes

Global warming is one of the most difficult challenges facing the world today. Without a significant reduction in greenhouse gas emissions, the global temperature will continue to increase, leading to the melting of polar ice caps and extreme weather events. In 2016, nearly 200 parties signed the Paris Agreement, with the long-term goal of keeping the increase in the global mean

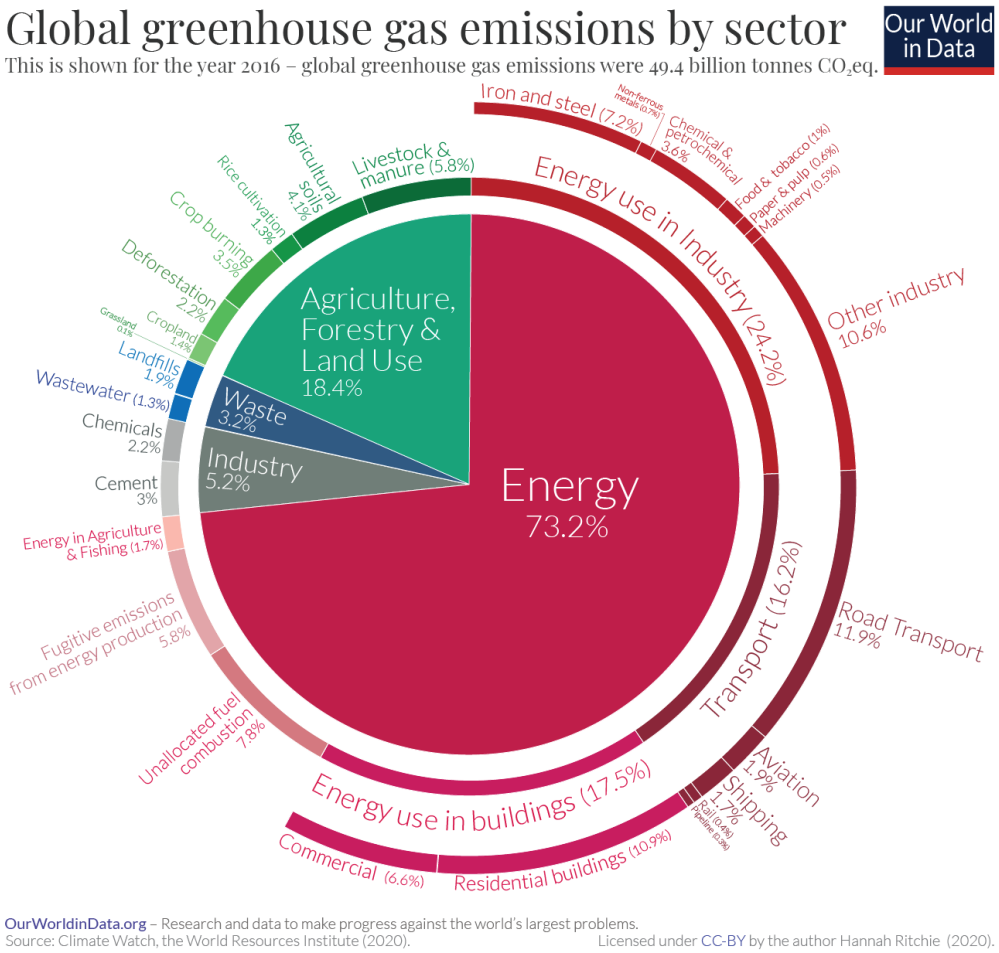

Figure 1.1: Greenhouse gas emissions by sector. Licenced under CC-BY by Hannah Ritchie [2].

temperature below 2 °C, compared to pre-industrial levels [1].

The energy sector is, by far, the largest contributor to greenhouse gas emissions [2]. In 2016, the same year as the Paris Agreement was signed, this sector accounted for nearly three-quarters of the total emissions, see Figure 1.1. The industry sector, comprising 24.2 % of the total emissions, is the largest sub-sector, with the iron and steel sector alone accounting for 7.2 %.

In 2015, 45 % of the total energy used within the industry sector in Europe was consumed as heat, with 18 % dedicated to heating processes at temperatures above 1000 °C [3]. The steel industry, in particular, consumes a substantial amount of energy in non-electric high temperature processes, as illustrated in Figure 1.2. Therefore, the electrification of such processes holds great promise for reducing the emissions of greenhouse gases as it allows the use of sustainable energy sources instead of the combustion of fossil fuels.

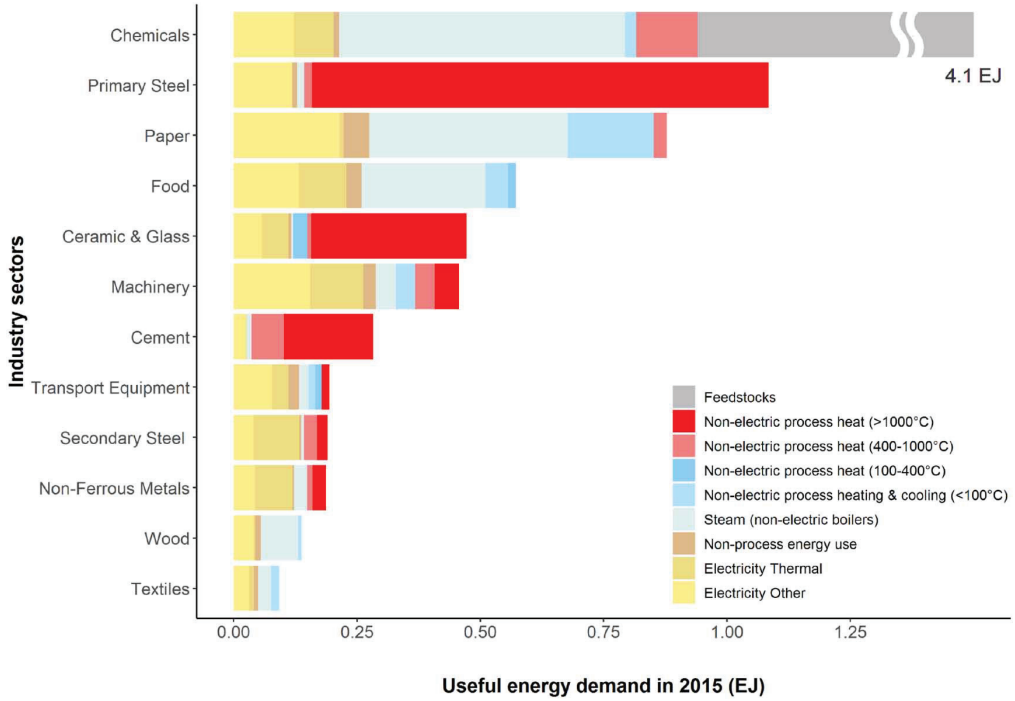

Figure 1.2: Useful energy demand for the industry sectors in 27 EU member states and the United Kingdom (2015). 'Figure 1' by Madeddu et al. [3] licensed under CC BY 4.0.

1.3 Resistive heating as a solution

A mature and popular electricity-driven heating system is resistance (or Joule) heating. This technology is used for a wide range of applications, including both industrial heating processes and household appliances. It requires low maintenance and comes with many advantages such as a rapid heating rate, high efficiency, and precise controllability. A typical heating element is shown in Figure 1.3(a).

A resistance-heated furnace is often equipped with several heating elements positioned vertically in the furnace, as shown in Figure 1.3(b). As the name reveals, the elements have high electrical resistivity and are directly heated by a current running through them. Using Ohm's law,

$$V = IR \tag{1.1}$$

and electrical power equation,

$$P = IV = I^2R \tag{1.2}$$

where V is the applied potential, I the current, R the resistance and P the power, the heat, Q, obtained from a heating element, with area A and length

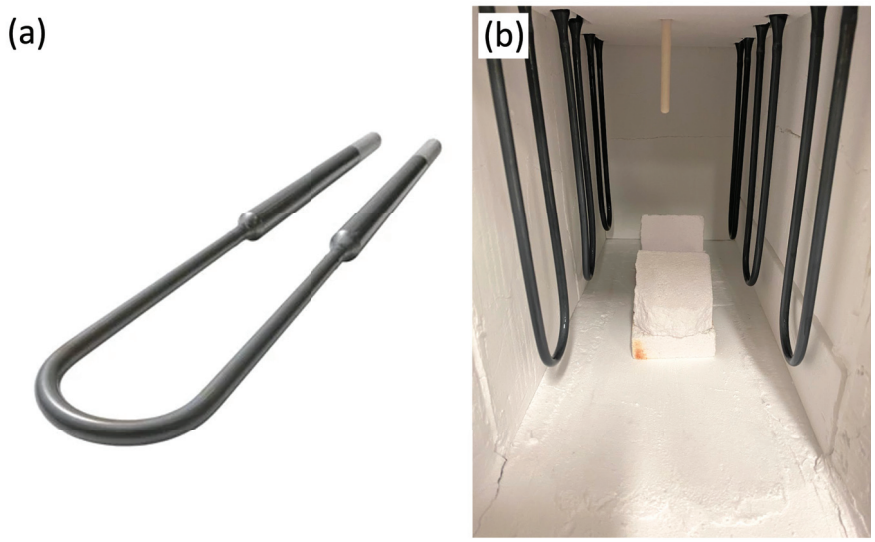

Figure 1.3: (a) A heating element, image from [4], (b) furnace with heating elements.

l, can be expressed as

$$Q = I^2Rt = \rho\frac{l}{A}I^2t \tag{1.3}$$

with ρ being the resistivity of the heating element. The elements heat the furnace through radiation, convection, and conduction.

1.3.1 $Mo(Si,Al)_2$ - a promising material with some challenges

High resistivity is a crucial requirement for a heating element. Figure 1.4 shows the resistivity as a function of temperature for four common heating element materials. The selection of material for a specific application depends on factors such as temperature and atmosphere. For temperatures below 1425 °C, alloys such as FeCrAl or NiCr may be suitable [5], while for higher temperatures, ceramics such as $MoSi_2$ or $Mo(Si,Al)_2$ become preferable [6]. In oxidising environments like dry air, $MoSi_2$ can be used for temperatures up to 1850 °C. However, in atmospheres containing noble gases, hydrogen or nitrogen, where the protective oxide scale on the element may break down, $Mo(Si,Al)_2$ proves a better option. This material exhibits a high melting point and excellent oxidation resistance in various atmospheres. It can be used for temperatures up to 1580 °C.

$Mo(Si,Al)_2$ is often considered a potential candidate material for resistive heating elements in the steel industry, playing an important role in reducing greenhouse gas emissions. However, an inherent challenge lies in the mechanical

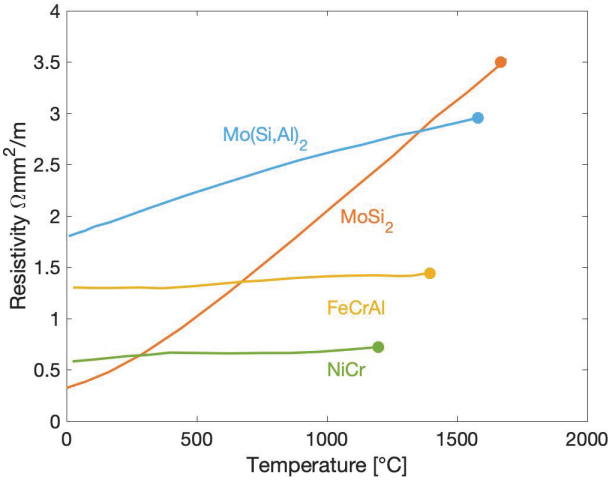

Figure 1.4: Resistivity as a function of temperature of four different heating element types. The filled circles indicate the maximum operating temperature. The figure is based on data from [7] and [6].

properties of $Mo(Si,Al)_2$. Above 1250 °C, the strength is low and decreases rapidly with temperature. Consequently, to prevent deformation due to their own weight, current $Mo(Si,Al)_2$ elements are relatively small. However, the size of the elements needs to be scaled up if being used to heat furnaces operating in the MW range. This increase in mass, in combination with a horizontal, rather than vertical, mounting of the elements in the furnace will potentially lead to excessive deformation. Therefore, the mechanical properties of $Mo(Si,Al)_2$ need to be improved. The larger elements may also affect oxidation-related properties, such as oxide scale adhesion.

1.4 Aim and Research questions

The mechanical properties and deformation mechanisms of polycrystalline C40-structured $Mo(Si,Al)_2$ are not well known. Therefore, the primary aim of this thesis is to answer the following question:

1. How does polycrystalline C40-structured $Mo(Si,Al)_2$ deform at high temperature?

A natural progression of the research is to explore potential ways to improve the mechanical properties. Two methods, particle strengthening and alloying, are investigated in this thesis. In connection with these topics, two questions are addressed:

2. Can the high temperature strength be improved through particle strengthening by adding Al_2O_3?

3. Is quaternary alloying of C40 possible, and how does it affect the strength?

As a final aspect, the oxidation behaviour of $Mo(Si,Al)_2$ is addressed:

4. How does alloying with yttrium affect the high temperature oxidation behaviour of $Mo(Si,Al)_2$?

CHAPTER 2

Structure and properties of $Mo(Si,Al)_2$ and other silicides

In this thesis, $Mo(Si,Al)_2$-based materials have been investigated with a focus on their microstructure, high temperature mechanical properties, and oxidation behaviour. Before presenting how these materials were prepared, tested, and analysed, a background on $Mo(Si,Al)_2$ and other silicides will be provided. This chapter aims not only to summarise previous research on the topic but also to highlight unexplored areas. As will be seen, these areas are closely connected to the Research questions presented in Section 1.4 and will be further addressed in Chapter 5.

2.1 Ceramic materials

$Mo(Si,Al)_2$ is a ceramic material which displays many characteristics typical of ceramics, including high hardness and stiffness. As schematically shown in Figure 2.1, ceramics typically exhibit fracture at low strains without undergoing plastic deformation when tested at ambient temperature, in contrast to metals that often undergo both elastic and plastic deformation before failure.

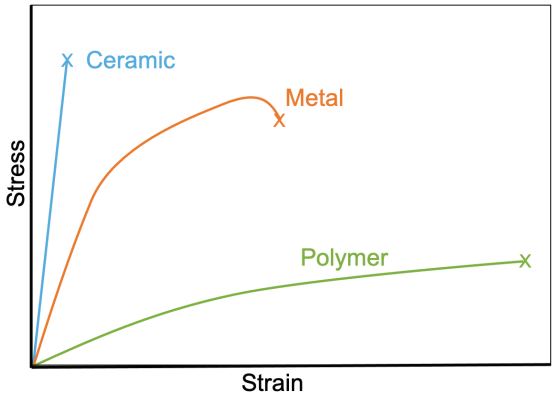

Figure 2.1: Typical stress-strain curves for ceramic, metal, and polymer materials.

The main reason for the different mechanical behaviour of ceramics and metals lies in the constrained dislocation activity in ceramics. When dislocations move through the material, bonds need to be broken and new ones created. In ceramics, characterised by strong and directional bonds of covalent or ionic nature, this process demands substantial energy. In metals, with delocalised electrons and non-directional bonds, dislocations move more readily [8, 9].

Another difference between metals and ceramics is the complexity of the unit cell [8, 9]. While metals typically have simpler unit cells, such as face-centred cubic (fcc) or body-centred cubic (bcc), ceramics generally have larger unit cells with lower symmetry, consisting of at least two types of atoms. Consequently, the Burgers vector ($\mathbf{b}$, describing the direction and magnitude of the slip caused by a dislocation) tends to be large in polycrystalline ceramic materials. Since the strain energy is proportional to the square of the Burgers vector, the energy required for dislocation nucleation in ceramics is generally higher than in metals [8, 9]. Due to the difficulty in activating multiple slip systems, ceramic materials do not usually satisfy the von Mises criterion (five independent slip systems are required to deform a material uniformly), resulting in brittle failure rather than yielding.

2.2 Silicides - crystal structure and chemistry

The term 'ceramics' represents a highly diverse material group and is often divided into subgroups. $Mo(Si,Al)_2$, along with other compounds consisting of a metal and silicon, such as $MoSi_2$, $NbSi_2$, and Mo_5Si_3, belongs to the subgroup 'silicides'. Silicides have been studied for more than 100 years, initially for their application as high temperature corrosion-protective coatings and later as bulk materials [10]. Their high melting point and generally good corrosion resistance make the materials well-suited for high temperature ap-

plications. However, the application of these materials is constrained by their mechanical properties. Similar to other ceramics, the large and complex unit cells affect the mechanical properties of silicides. In Table 2.1 and Figure 2.2, some selected silicides, which will be discussed in the following sections, and their crystal structures, are shown. For size and complexity comparisons, bcc-structured Mo is included in the table.

Table 2.1: Crystal structure, lattice parameters and melting point of selected silicides. *This work. **Calculated using Thermo-Calc by Thomas Helander, Kanthal AB.

Material	**Crystal structure**	**Lattice parameters (Å)**	**Melting point (°C)**
$Mo(Si,Al)_2$	**C40** (hexagonal) < 3 at.% Al: $C11_b$ (tetragonal) [11] > 33 at.% Al: C54 (orthorhombic) [12]	$a = 4.73$, $c = 6.59$*	∼1800**,[13]
$MoSi_2$	**$C11_b$** (tetragonal) Above 1900 °C: C40 (hexagonal)	$a = 3.21$, $c = 7.85$ [14]	2020 [11]
$NbSi_2$	C40 (hexagonal)	$a = 4.80$, $c = 6.59$ [14]	1920 [11]
$CrSi_2$	C40 (hexagonal)	$a = 4.43$, $c = 6.37$ [14]	1438 [15]
VSi_2	C40 (hexagonal)	$a = 4.57$, $c = 6.38$ [14]	1677 [16]
$TaSi_2$	C40 (hexagonal)	$a = 4.78$, $c = 6.57$ [14]	2040 [16]
WSi_2	$C11_b$ (tetragonal)	$a = 3.21$, $c = 7.83$ [14]	2160 [11]
Mo_5Si_3	$D8_m$ (tetragonal)	$a = 9.64$, $c = 4.91$ [17]	2180 [11]
Mo_5Si_3C	$D8_8$ (hexagonal)	$a = 7.29$, $c = 5.04$ [18]	2100 [18]
Mo	bcc (cubic)	$a = 3.15$ [19]	2620 [19]

The focus of this thesis is on a $Mo(Si,Al)_2$ material with an approximate chemical composition of 34:37:29 at.% Mo:Si:Al. This material is C40-structured, the crystal structure can be seen in Figure 2.2(a). However, the structure of $Mo(Si,Al)_2$ depends on the Si and Al content. At low Al contents, below 3.2 at.%, or $Mo(Si_{1-x}Al_x)_2$ with $x \leq 0.05$, it has been reported that the material adopts the $C11_b$ structure of $MoSi_2$ (see Figure 2.2(b)) [11, 20]. In the range of $0.2 \leq x \leq 0.5$, a monolithic C40-structure has been reported, while $C11_b$ and C40 coexist for $0.08 \leq x \leq 0.15$. Al contents exceeding $x = 0.5$ (33 at.%), result in a duplex microstructure comprising C40 and C54 (Figure 2.2(c)) [20]. The formation of a monolithic C54 microstructure at higher Al content has been debated. In [12], monolithic C54 was observed for $x = 0.6$, while in [20], the duplex C40+C54 structure persisted at high Al content. Conversely, in [21] it was reported that an Al content of $x = 0.65$ yielded a microstructure primarily consisting of C54-structured $Mo(Si,Al)_2$, with smaller amounts of $Mo_5(Si,Al)_3$ and Mo_3Al_8. Traces of $Mo_5(Si,Al)_3$ ($D8_m$-structured,

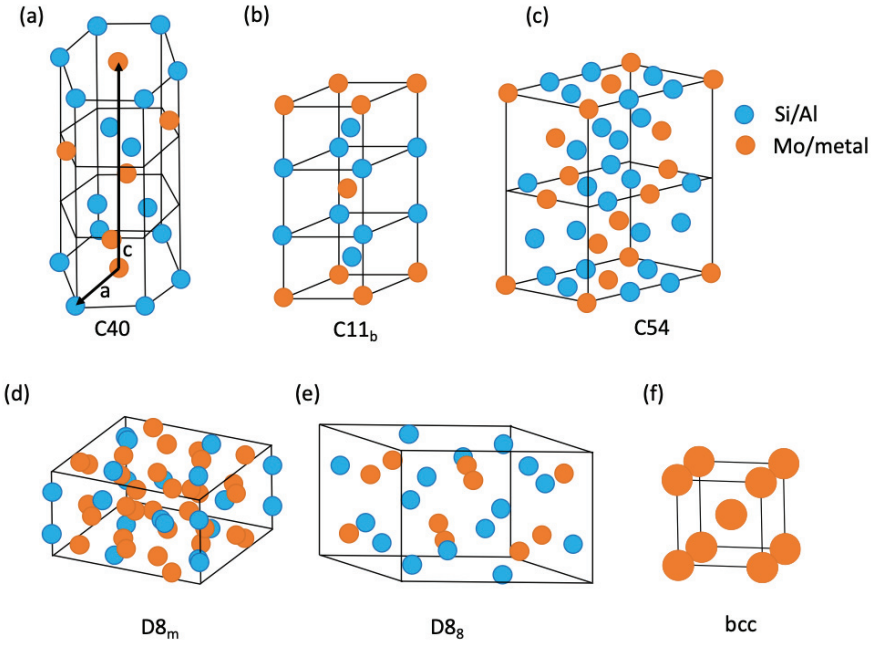

Figure 2.2: Crystal structures of (a) C40, (b) $C11_b$, (c) C54, (d) $D8_m$, (e) $D8_8$, (f) bcc. The crystallographic a and c-axes are indicated in C40. The unit cells are not to scale.

Figure 2.2(d)) are usually present in all $Mo(Si,Al)_2$ materials, regardless of Al content [20].

Despite having different crystal structures, the arrangements of atoms on the close-packed planes are relatively similar in the three $Mo(Si,Al)_2$ structures. The main difference between the different structures is the stacking sequence of these planes [16].

The materials investigated in this thesis were prepared from elemental powders which were heated to initiate a self-propagating reaction leading to the formation of $Mo(Si,Al)_2$. The synthesis will be further described in Chapter 3. However, due to local chemical variations and contamination by O and C, small amounts of Al_2O_3 and $Mo_5(Si,Al)_3$ ($D8_m$ and $D8_8$-structured, see Figure 2.2(d) and (e), respectively) were formed. Due to the low volume fractions of $D8_m$ and $D8_8$, these phases are just briefly mentioned in this thesis.

2.3 High temperature deformation of silicides

'High temperature' is a context-dependent term and requires clarification. In this thesis, 'high temperature' refers to a temperature above 1250 °C, which corresponds to the ductile to brittle transition temperature (DBTT) of poly-

crystalline $Mo(Si,Al)_2$ [22]. The following sections provide a review of the available, albeit limited, research on high temperature mechanical properties of $Mo(Si,Al)_2$ and other C40-structured materials.

2.3.1 C40-structured $Mo(Si,Al)_2$

2.3.1.1 Single crystalline $Mo(Si,Al)_2$

The deformation behaviour of single crystalline C40-structured $Mo(Si,Al)_2$ has been studied by Inui et al. [23–25]. In their work [23], it was demonstrated that $Mo(Si,Al)_2$ exhibits plastic deformation by the activation of a single slip system, $(0001)\langle 1\bar{2}10\rangle$, with a Burgers vector of $\frac{1}{3}\langle 1\bar{2}10\rangle$-type. The onset temperature for this slip system is 1200 °C for $Mo(Si_{0.8}Al_{0.2})_2$ and 1100 °C in the case of the Al-leaner material $Mo(Si_{0.85}Al_{0.15})_2$, see Figure 2.3(a). Above the onset temperature, the yield stress decreases rapidly with increasing temperature [23]. Stress-strain curves from compression testings of $Mo(Si_{0.8}Al_{0.2})_2$ at different temperatures can be seen in Figure 2.3(b). Below the onset temperature, $Mo(Si,Al)_2$ does not undergo plastic deformation [23]. For crystals oriented in a manner that prevents the $(0001)\langle 1\bar{2}10\rangle$ slip system from operating, no plastic deformation takes place regardless of temperature [23].

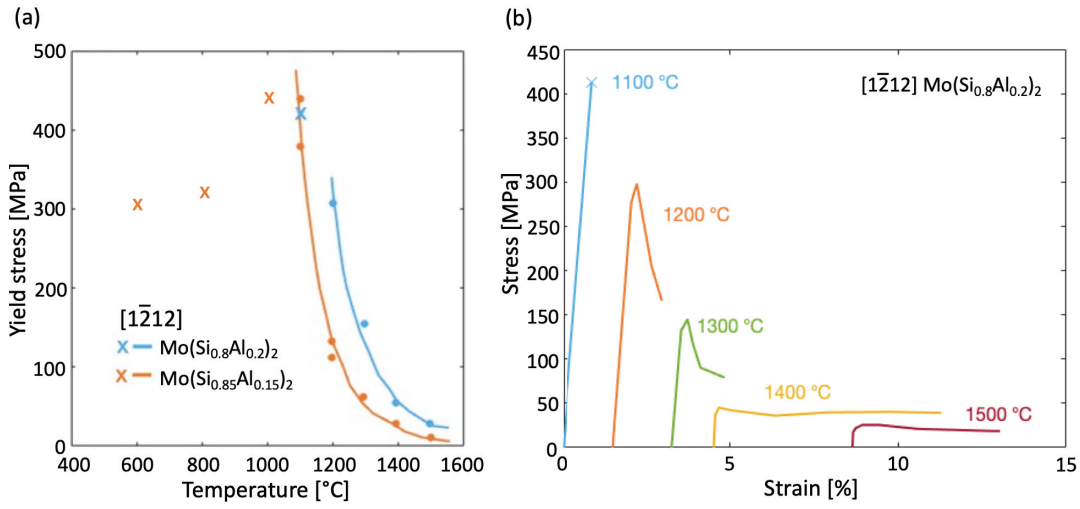

Figure 2.3: (a) Yield stress as a function of temperature for $Mo(Si_{0.85},Al_{0.15})_2$ and $Mo(Si_{0.80},Al_{0.20})_2$ single crystals, oriented with the $[1\bar{2}12]$ direction along the compression axis. X indicates the stress at which failure occurred without any plastic flow. (b) Stress-strain curves obtained from a $[1\bar{2}12]$ oriented $Mo(Si_{0.80}Al_{0.20})_2$ single crystal tested in compression at elevated temperatures. The figures are based on data from [23].

$Mo(Si,Al)_2$ deforms through a synchroshear mechanism, which was studied

in [23]. The predominant dislocation type, characterised by a Burgers vector of $\frac{1}{3}[1\bar{2}10]$ was shown to dissociate into two synchro-partials with identical Burgers vectors, $\frac{1}{6}[1\bar{2}10]$, hereafter denoted as $\mathbf{b}_1$, with a stacking fault in between. Subsequently, these synchro-partials further dissociate into two additional partials on adjacent atomic planes, facilitating synchronous shearing of the crystal. Figure 2.4(a) illustrates the synchroshear resulting in the total displacement of $\mathbf{b}_1$ [23]. The Burgers vector $\mathbf{b}_1$, as well as $\mathbf{b}_2$ and $\mathbf{b}_3$ which will be introduced in the next section, are indicated in Figure 2.4(b).

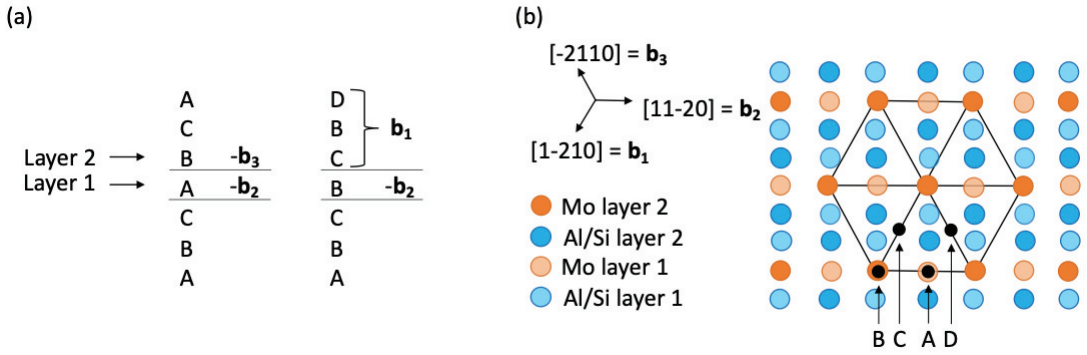

Figure 2.4: (a) Synchroshear mechanism giving rise to the total displacement of $\mathbf{b}_1$ for Layer 2 and all layers above, (b) stacking of C40 basal layers. The bright atoms are positioned in Layer 2 above Layer 1 (faded atoms). Position A, B, C and D indicate possible sites for Mo atoms in layers positioned above Layer B. The possible Burgers vectors for a glide along the basal plane are shown in the top left corner.

The original stacking sequence of atomic layers parallel to the basal plane is shown on the left-hand side in Figure 2.4(a). Layer 1 (L_1), with Mo atoms positioned at A sites (see Figure 2.4(b) for possible Mo-sites), undergoes a displaced of $-\mathbf{b}_2$. The adjacent Layer 2 (L_2), with Mo atoms originally at B positions, as well as all layers above, are displaced by the same vector. Simultaneously, L_2, and the layers above, undergo an additional displacement of $-\mathbf{b}_3$. The resulting sequence is shown on the right-hand side of Figure 2.4(a). The total displacement of L_2, and all layers above, is $\mathbf{b}_1$ ($-\mathbf{b}_2-\mathbf{b}_3 = \mathbf{b}_1$). This constitutes the first, or leading, synchro-partial, which is succeeded by an identical trailing synchro-partial. Figure 2.5(a) shows all partials in the leading and trailing synchro-partial. As indicated on the left-hand side of the figure, the total shear of L_2 is $2\mathbf{b}_1$, equivalent to $\frac{1}{3}[1\bar{2}10]$, the Burgers vector of the full dislocation [23].

Inui et al. investigated the dislocation core using High-Resolution Transmission Electron Microscopy (HRTEM) [23]. The observed displacement of L_1 did not align with that proposed in Figure 2.5(a). Therefore, an alternative synchroshear mechanism was proposed, see Figure 2.5(b) [23]. However, this alternative mechanism exhibited certain drawbacks, involving more complex dislocations, with non-symmetrical synchro-partials and a Burgers vector that

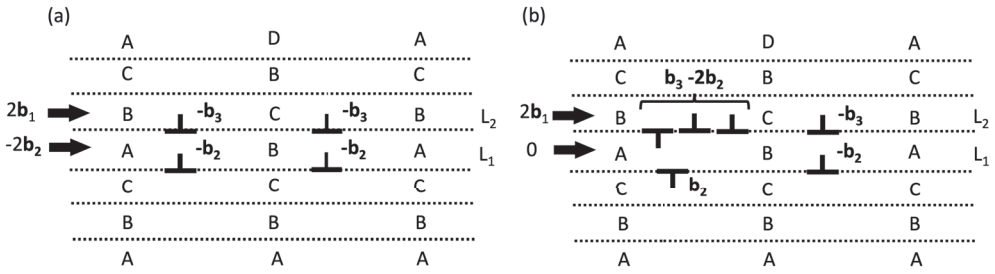

Figure 2.5: Two models of synchro-shear mechanisms giving rise to the total displacement of $\mathbf{b}_1$ of L_2 and the layer above.

could disintegrate into three new partials. Consequently, Inui et al. concluded that the former mechanism (shown in Figures 2.4(a) and 2.5(a)) provides a more accurate description of the deformation, despite the observed discrepancy in the displacement of L_1 with HRTEM observations [23]. Additionally, it was suggested that diffusion of Al could be involved in the deformation of $Mo(Si,Al)_2$ [23].

2.3.1.2 Polycrystals

The high temperature mechanical properties of polycrystalline $Mo(Si,Al)_2$ have not received much attention previously. A DBTT of 1250 °C, has been reported by Hagihara et al. [22] and Umakoshi et al. [16]. The chemical composition of this material was $Mo(Si_{0.75}Al_{0.25})_2$. Consistent with the research on single crystalline $Mo(Si,Al)_2$, $(0001)\langle 1\bar{2}10\rangle$ was the only active slip system, with the yield stress rapidly decreasing above the DBTT, see Figure 2.6.

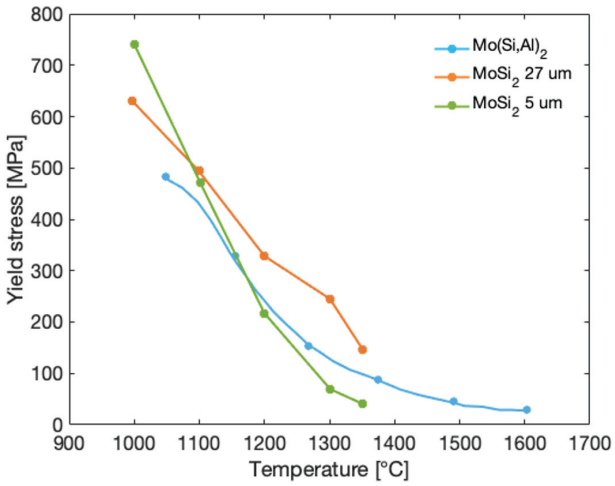

Figure 2.6: Temperature dependence of yield stress in polycrystalline $Mo(Si,Al)_2$ and $MoSi_2$ (grain size: 5 μm and 27 μm). The figure is based on data from [16] and [26].

Unfortunately, neither stress-strain curves nor microstructural investigations of deformed $Mo(Si,Al)_2$ were presented in the studies by Hagihara et al. [22] and Umakoshi et al.[16]. Furthermore, the grain size, which is known to be very important for the strength of other silicides (e.g., $MoSi_2$, see Figure 2.6 [26]), was not provided. Therefore, this thesis aims to address these gaps by presenting stress-strain curves and detailed microstructural investigations of $Mo(Si,Al)_2$ tested in compression and bending, as well as the effect of grain size. The results are presented and discussed in Chapter 5 and the Papers I, II, and III.

2.3.2 Other C40-structured disilicides

As previously discussed, $Mo(Si,Al)_2$ undergoes plastic deformation through a synchroshear mechanism. Another C40-structured silicide that deforms by the same mechanism is $CrSi_2$ [11, 16, 27, 28]. In contrast, other C40-structured silicides, including VSi_2, $TaSi_2$, and $NbSi_2$, deform conventionally without splitting into partials. This influences the onset temperature for plastic flow. Single crystals of VSi_2, $TaSi_2$, and $NbSi_2$ may undergo plastic deformation already at room temperature (corresponding to around 0.3 T/T_m, where T_m is the melting temperature), provided they are oriented so that $(0001)\langle 1\bar{2}10\rangle$ slip system is operative [28–31]. The onset of plastic flow for $Mo(Si,Al)_2$ and $CrSi_2$ requires a higher temperature, close to 0.6 T/T_m [25]. Furthermore, the silicides with the lower onset temperature exhibit an anomalous increase in yield stress at elevated temperatures, see Figure 2.7 [28–31]. This has not been observed in either $Mo(Si,Al)_2$ or $CrSi_2$ [23, 28].

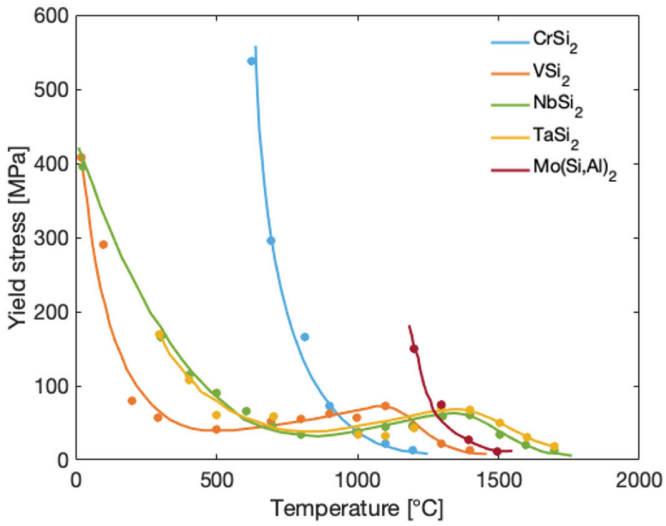

Figure 2.7: Temperature dependence of yield stress in various C40 single crystals. The figure is based on data from [16] and [23].

The deformation behaviour of C40-structured silicides has also been studied using micropillar compression [32]. Interestingly, in microscale testing, $CrSi_2$ exhibited plastic deformation through conventional shear at temperatures as low as room temperature. At 700 °C, this shifted to the synchroshear mechanism operative at high temperatures [32]. However, micropillar compression of $Mo(Si,Al)_2$ has not been conducted.

An additional noteworthy observation regarding the deformation behaviour of C40 silicides was presented in [29]. Even though C40-structured silicides traditionally are said to deform by only one slip system, $\{0001\}\langle 1\bar{2}10\rangle$, four additional slip systems $\{10\bar{1}0\}\frac{1}{3}\langle 1\bar{2}10\rangle$, $\{10\bar{1}1\}\frac{1}{3}\langle 1\bar{2}10\rangle$, $\{10\bar{1}0\}\frac{1}{3}\langle 0001\rangle$ and $\{11\bar{2}Y\}\langle 11\bar{2}X\rangle$, (where X×Y = -6) were found to operate in $NbSi_2$ tested in tension at high temperature. Traces of such slips were observed in regions with high stress concentrations [29].

In order to fully understand the deformation mechanism of $Mo(Si,Al)_2$ and other C40-structured silicides further research is needed. Of particular interest is exploring whether anomalous increases in stress can also be induced in $Mo(Si,Al)_2$, possibly through alloying. Since the alloying of $Mo(Si,Al)_2$ with Nb, Ta, or V has not been explored before, this is one of the objectives of this thesis.

2.3.3 $C11_b$-structured $MoSi_2$

A silicide that has been more thoroughly investigated in terms of mechanical properties is $C11_b$-structured $MoSi_2$. As the crystal structure holds many similarities with C40-structured $Mo(Si,Al)_2$, this material will be used as a reference for comparisons with literature.

The DBTT of $MoSi_2$ has been reported to be within the temperature range of 1000–1300 °C, depending on the level of carbon contamination [26, 31, 33–36]. An important distinction between the two materials lies in the impact of oxygen contamination, leading to the formation of SiO_2 in $MoSi_2$, and Al_2O_3 in $Mo(Si,Al)_2$. At elevated temperatures, the SiO_2 particles soften and form an amorphous SiO_2 film which promotes grain boundary sliding leading to softening of the polycrystalline material [37]. Consequently, as shown in Figure 2.6, coarse-grained $MoSi_2$ demonstrates higher strength than fine-grained material, since the material contains fewer grain boundaries [26].

$MoSi_2$ exhibits very low creep strength at elevated temperatures [38]. In coarse-grained materials (with a grain size of 27 μm), dislocation glide and climb were identified as the dominant creep mechanisms. Conversely, in fine-grained materials (with a grain size of 5 μm), grain boundary sliding, accom-

panied by grain boundary diffusion (Coble-creep), was reported as the primary deformation mechanism [38, 39].

The strength of $MoSi_2$ can be improved by particle strengthening. This can be achieved by C and Al alloying, which reduces the amount of SiO_2 at grain boundaries by the formation of SiC and Al_2O_3, respectively [37, 40]. Notably, SiC and Al_2O_3 also act as grain refiners, reducing the grain size and subsequently reducing the strength. At high SiC fractions (20–30 vol.%), the effect of particle strengthening overcomes the softening attributed to the reduction in grain size, resulting in improved mechanical properties [37, 40].

Particle strengthening of C40-structured $Mo(Si,Al)_2$ has not been investigated previously. Despite the absence of amorphous SiO_2 at grain boundaries in $Mo(Si,Al)_2$, grain boundary sliding probably plays an important role during deformation. In this thesis, the effect of particle strengthening has been investigated in Paper II and Paper III.

The high temperature strength of $MoSi_2$ can also be improved by W alloying. $C11_b$-structured WSi_2 forms a complete solid solution with $MoSi_2$ [41, 42], and the strength in single crystalline $(Mo,W)Si_2$ has been reported to increase with the amount of added W [42]. Moreover, W alloying also increases the onset temperature for plastic flow [42]. In this thesis, the W alloying of $Mo(Si,Al)_2$, a topic previously unexplored in terms of mechanical properties, has been investigated.

Additionally, it has been reported that Nb and Al alloying can improve the high temperature strength of $MoSi_2$ [43]. However, the alloying content needs to be low, as the stability of the $C11_b$ structure diminishes at higher concentrations. As previously discussed, the solubility of Al in $C11_b$ is limited to around 3 at.% Al [11, 20]. In the case of Nb alloying, the maximum solubility is approximately 1.2 at.% in $C11_b$ [43]. Exceeding this concentration was reported to result in a duplex microstructure consisting of $C11_b$ and C40-structured $(Nb,Mo)Si_2$ [43]. However, in [44], it was reported that the solid solubility of Nb in the $C11_b$ phase was high and that $(Mo_{1-x}Nb_x)Si_2$, with $x = 0$, 0.25, 0.5, 0.75, and 1 was successfully prepared. However, the credibility of the paper can be debated as it contains several uncertainties. For example, the authors claimed that all materials, pure $NbSi_2$ included, retained the tetragonal $C11_b$ structure of $MoSi_2$, even though this phase was absent in the XRD diffractograms of the Nb-containing materials. The presence of C40, which, according to the diffractograms was the dominating phase in the Nb-containing materials, was not mentioned.

2.4 Oxidation of $Mo(Si,Al)_2$

$Mo(Si,Al)_2$ was originally developed to improve the oxidation properties of $MoSi_2$ [45, 46]. At temperatures above 1000 °C, a protective and self-healing SiO_2 scale is formed on $MoSi_2$ [47, 48]. However, at intermediate temperatures, (400–700 °C), the material suffers from accelerated oxidation and pesting (the disintegration of $MoSi_2$ into a powder) [49, 50]. However, pesting can be suppressed by Al alloying [51–53]. Due to preferential oxidation of Al, $Mo(Si,Al)_2$ forms Al_2O_3, which offers protection in both oxidising and reducing environments, unlike than SiO_2, which is only protective in oxidising environments [51–54].

Several research groups have investigated the oxidation behaviour of $Mo(Si,Al)_2$ [49, 51–53, 55–59]. Some of the most comprehensive studies were conducted by Ingemarsson et al. [51–53, 59], who studied the oxidation behaviour of the $Mo(Si,Al)_2$ material 'Kanthal Super ER' in the temperature range of 300–1600 °C. Given the similarities between Kanthal Super ER and the reference material used in this work, the studies by Ingemarsson et al. hold particular significance.

At intermediate temperatures (300–1000 °C) $Mo(Si,Al)_2$ forms a mixed oxide scale comprising Al_2O_3, SiO_2 and MoO_3 [51, 52]. The mass gain, attributed to oxygen uptake, increases with temperature up to 500 °C, see Figure 2.8. Between 600 and 700 °C, the mass gain initially rises, followed by a decrease due to the evaporation of MoO_3, but with no occurrence of pesting. At 1000 °C, the scale is primarily composed of Al_2O_3, with only small amounts of SiO_2 [52].

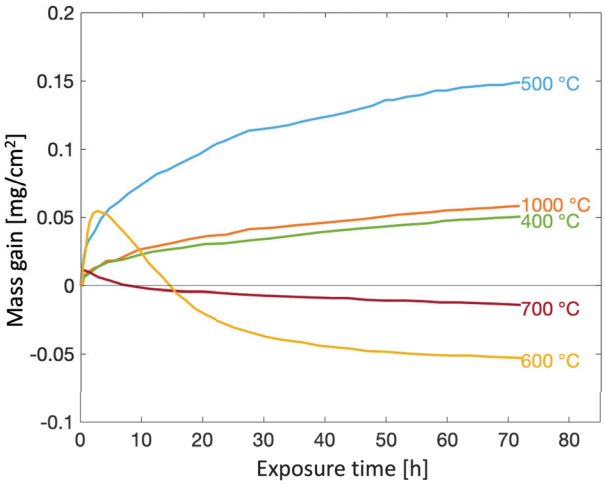

Figure 2.8: The mass gain as a function of exposure time for the $Mo(Si,Al)_2$-based material exposed in synthetic air at different temperatures. Based on data from [52].

At temperatures exceeding 1000 °C, $Mo(Si,Al)_2$ forms a dense and protective Al_2O_3 scale [53, 59, 60]. The oxidation rate increases with increasing temperature. In oxidising environments, the mass gain of $Mo(Si,Al)_2$ is higher than that of $MoSi_2$, see Figure 2.9.

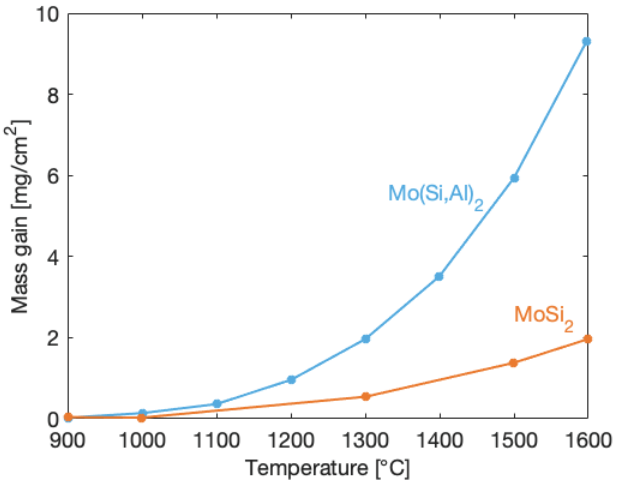

Figure 2.9: Mass gain of $Mo(Si,Al)_2$ and $MoSi_2$ after 72 h oxidation in air as a function of temperature. Based on data from [53].

During oxidation, a phase transformation from $Mo(Si,Al)_2$ to $D8_m$-structured $Mo_5(Si,Al)_3$ occurs at the interface between the oxide scale and $Mo(Si,Al)_2$. This transformation is a consequence of the preferential oxidation of Al, leading to an Al-depleted region which eventually evolves into the $Mo_5(Si,Al)_3$ layer, see Reaction 2.1 [52, 59]. Due to a very low Al content, this layer is denoted as Mo_5Si_3 in Reaction 2.1.

$$(25x + 10)\ \mathrm{MoSiAl} + 10.5\ x/4\ \mathrm{O_2} \rightarrow$$
$$35x/2\ \mathrm{Al_2O_3} + 10\ \mathrm{Mo(Si_{1+x},Al_{1-x})} + 5x\ \mathrm{Mo_5Si_3} \qquad (2.1)$$

The $Mo_5(Si,Al)_3$ layer is porous due to the volume decrease associated with the phase transformation. Additionally, this layer contains Al_2O_3 grains, encapsulated by the inward growth of the $Mo_5(Si,Al)_3$ layer, see Figure 2.10.

The third reaction product of Reaction 2.1, $Mo(Si_{1+x},Al_{1-x})$, shares the same C40-structure as bulk $Mo(Si,Al)_2$ but with a reduced Al content. The lowest Al concentration is observed near the $Mo_5(Si,Al)_3$ layer and increases gradually to its original level in the deeper regions of the material. The Al gradient is compensated by an inverse Si gradient, ensuring the $Mo(Si,Al)_2$ stoichiometry [60].

On some occasions, the oxide scale formed on $Mo(Si,Al)_2$ does not consist of pure Al_2O_3, but also SiO_2 and mullite ($3Al_2O_3{\cdot}2SiO_2$). The Si-containing ox-

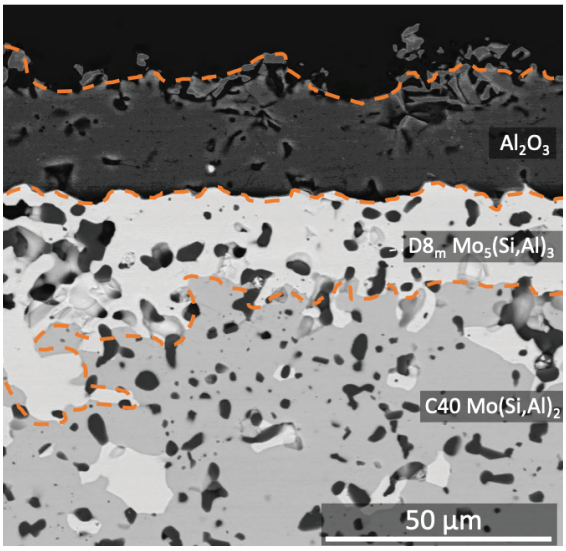

Figure 2.10: Cross-section of an oxidised $Mo(Si,Al)_2$ sample. The $Mo_5(Si,Al)_3$ layer is seen in bright contrast between the oxide and $Mo(Si,Al)_2$.

ides are remnants of a Na-Si-Al-O glass, formed in the early stage of oxidation due to Na contamination from the material synthesis [60].

At elevated temperatures, where the material forms a protective Al_2O_3 scale, spallation of the oxide scale is minimal [60]. Nevertheless, spallation has been observed on a few occasions. In this thesis, the influence of Y doping of $Mo(Si,Al)_2$ on the oxidation properties has been studied. Y, along with other reactive elements, has previously been successfully employed to enhance oxide adhesion in other Al_2O_3-forming materials, such as FeCrAls [61–63].

CHAPTER 3

Materials synthesis - From powder to polycrystalline $Mo(Si,Al)_2$

In this thesis, the microstructure, mechanical behaviour and oxidation properties of $Mo(Si,Al)_2$, modified through either particle strengthening or alloying, have been investigated. Various materials have been synthesised and compared with an unmodified reference material, in which the Mo, Si, and Al contents were chosen to resemble the commercially available 'Kanthal Super ER' (34:35:27 at.% Mo:Si:Al [52]). All materials have been synthesised in the laboratory at Kanthal, Hallstahammar, following similar protocols. The synthesis starts with elemental powders which undergo mixing, reaction, milling, densification, and subsequent sintering to produce dense materials. In the following sections, each step will be explained. The entire process can also be followed in Figure 3.1. All materials synthesised for this thesis are listed in Table 3.1.

Mixing
Elemental Mo (99.9 % purity, Cerac Inc.), Si (99.99 %, Wacker) and Al (99.5 %, GoodFellow) powders were weighed and mixed to obtain a homogeneous powder. For alloyed materials, elemental Nb (99.9 %, H.C. Starck), Ta (99.9 %, H.C. Starck), V (99.5 %, ABSCO Limited), Y (99.9 %, Cerac Inc.) and W (99.9 %, Treibacher Industrie AG) powders were also added in this step. A

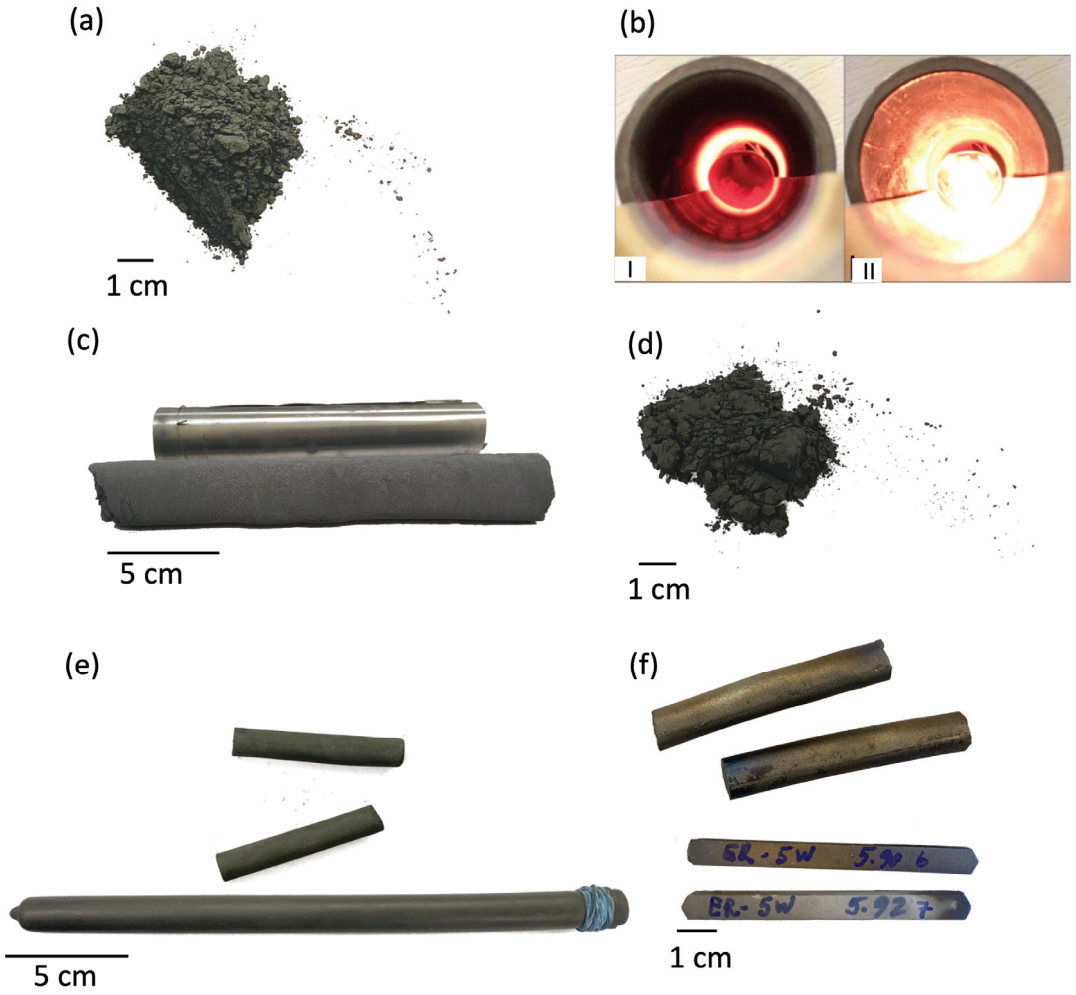

Figure 3.1: From powder to sintered material: (a) mixed powder before reaction, (b) powder before (I), and during (II), the self-propagating reaction in tube furnace, (c) cooled reaction product and Mo-cylinder, (d) reacted powder after milling, (e) CIP mould filled with powder and green bodies after compaction, (f) rod and rectangular $Mo(Si,Al)_2$ after sintering. The scale bars are approximate.

Table 3.1: Summary of materials and synthesised methods.

Material	Added Al_2O_3 (wt.%)	Amount of added element (yX)	Reaction method	Milling method	Compaction method	Sintering temperature (°C)	In paper
$Mo(Si,Al)_2$-Al_2O_3composites							
Reference	0						I, II, III
A5	5						
A10	10			Vial container			
A15	15	-	Large furnace	with gasoline and	CIP	1650	II, III
A20	20			Mo balls			
A25	25						
A30	30						
Quaternary alloyed $(Mo_{1-y},X_y)(Si,Al)_2$							
Reference		-					
5Nb		0.05Nb					
10Ta	3	0.1Ta	Tube furnace	Vibratory disc mill	CIP	1600–1610	IV
5V		0.05V					
10V		0.1V					
Reference		-					
5W	3	0.05W	Tube furnace	Vibratory disc mill	Uni-axial press + CIP	1625	Thesis
25W		0.25W					
50W		0.5W					
Reference		-					
0.1Y		0.01Y					
0.5Y	3	0.05Y	Tube furnace	Vibratory disc mill	CIP	1600	V
1Y		0.1Y					
2Y		0.2Y					

photograph of the powder mixture is shown in Figure 3.1(a).

Reaction

The mixed powders were heated to initiate a self-propagating reaction, leading to the formation of $Mo(Si,Al)_2$, or $(Mo,X)(Si,Al)_2$, where X represents the alloying element. Small amounts of $Mo_5(Si,Al)_3$ (or $(Mo,X)_5(Si,Al)_3$) and Al_2O_3 were also formed in the reaction. Two different types of furnaces were used for the reaction, depending on the amount of powder. The unalloyed material, used as a reference and as the base for all $Mo(Si,Al)_2$-Al_2O_3 composites, was prepared in a larger quantity of 5 kg. It was reacted as one batch in an Ar gas-filled furnace. The furnace was heated, and at approximately 800 °C, the powder ignited, initiating the self-propagating reaction. After the reaction, the product was cooled in an Ar gas atmosphere to prevent oxidation.

For the alloyed materials, smaller batches of around 100 g were reacted in a tube furnace. The powder mixtures were filled in Mo cylinders which were then placed in the furnace. Figure 3.1(b) shows the powder before and during the reaction in the furnace. The reaction product is shown in front of a Mo-cylinder in Figure 3.1(c).

Milling
The reaction product underwent milling to achieve a surface area of approximately 1.8 m^2/g, a value previously demonstrated to yield sintered materials with a comparable grain size to Kanthal Super ER. For the 5 kg reaction used for producing the unalloyed powder, milling occurred in a Mo-lined vial container with gasoline and Mo-balls for 228 hours. The resulting particle size distribution is presented in Figure 3.2. Alloyed materials were milled in a vibratory disc mill for 6x1 min, which resulted in a similar grain size.

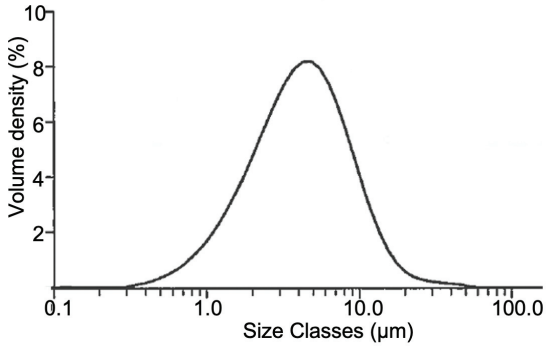

Figure 3.2: Particle size distribution of milled powder.

Addition of Al_2O_3 powder
Al_2O_3 powder (AKP-53, Sumitomo Chemical) was added to all materials except one of the reference materials (the first listed material in Table 3.1). The addition of Al_2O_3 limits grain growth during sintering. 5–30 wt.% Al_2O_3 was added to the Mo(Si,Al)$_2$-Al_2O_3 composites, and 3 wt.% Al_2O_3 was added to the alloyed materials. The powders were milled in the vibratory disc mill for one minute to prevent agglomeration of the Al_2O_3 particles.

Compaction
Following the addition of Al_2O_3, the powders were filled in soft rubber moulds and compacted into green bodies using a cold isostatic press (CIP, EPSI), operating at 2000 bar. Green bodies and a CIP-mould are shown in Figure 3.1(e). The W-alloyed materials prepared for four-point bending were prepressed into rectangular bars using a uniaxial press before final compression in the CIP.

Sintering
The green bodies were sintered in H_2 gas for 30–60 min at 1600–1650 °C depending on the material, see Table 3.1. The time and temperature were chosen to result in materials having as high density as possible. Sintered materials are shown in Figure 3.1(f).

CHAPTER 4

Experiments and analysis

4.1 Mechanical testings

The assessment of mechanical properties in materials entails a range of testing methods, although not all are ideal for ceramic material. For example, machining dog bone-shaped specimens for tensile testing might pose challenges due to the inherent brittleness of ceramics. Moreover, mounting poses difficulties, as even slight misalignment may lead to failure due to stress concentrations. Furthermore, the pores in ceramics lower the stress values measured in tensile testing. Therefore, ceramics are preferably subjected to compression testing, where the impact of pores is less pronounced. Another widely employed test method for ceramics is four-point bending, which exposes the specimen to both compressive and tensile stresses. The specimen geometries for compression and four-point bending are much simpler compared to those required for tensile testing.

In this thesis, both compression and four-point bending were used to evaluate the mechanical properties of $Mo(Si,Al)_2$-based materials at 1300 °C. This temperature was chosen as it falls within the service temperature range of currently available $Mo(Si,Al)_2$ heating elements (1200–1580 °C [6]) and exceeds the DBTT of the material (1250 °C [16, 22]). Although higher test tempera-

tures are of interest, the systems for both compression and four-point bending had a maximum limit of 1300 °C.

4.1.1 Compression

The compressive strength of the $Mo(Si,Al)_2$-A_2O_3 composites was tested using a Gleeble 3800 thermomechanical simulator [64]. Cylindrical test specimens (with a diameter of 8 mm, and height of 12 mm), prepared by grinding of sintered rods (with an initial diameter of approximately 11 mm), were subjected to testing in vacuum at 1300 °C. The specimens were heated by resistive heating and a strain rate of $1{\cdot}10^{-4}$/s was used for the compression.

A photograph of the Gleeble apparatus is shown in Figure 4.1(a). The specimen is positioned in the gap between two anvils, see Figure 4.1(b). Ni-paste and graphite foils are placed between the specimen and the anvils to ensure electrical contact. ISO-T anvils, designed to keep a constant and even temperature, were used in this study. These anvils consist of two cylindrical hard metal (WC-Co) cylinders (a cap and a base) with graphite foils in between, as shown in Figure 4.1(c), and are held in place by two jaws. The jaw on the left-hand side of the specimen in Figure 4.1(a) is movable and connected to a hydraulic servo system, while the jaw on the other side of the specimen is stationary.

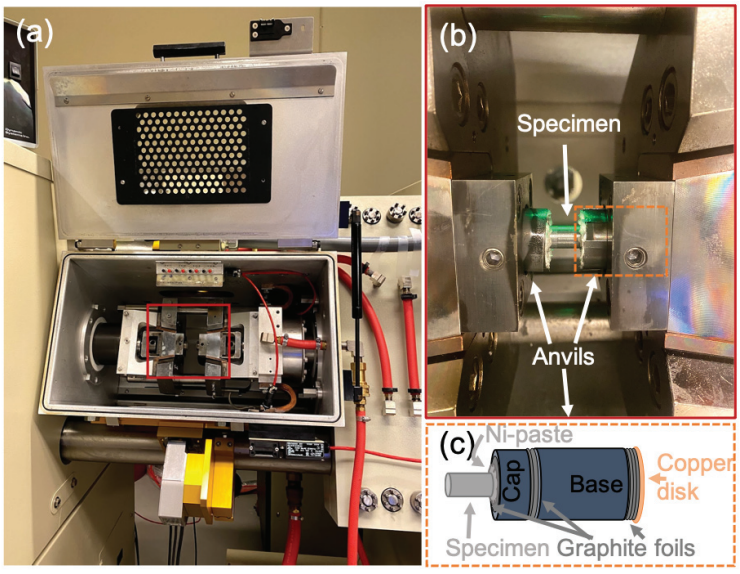

Figure 4.1: (a) The Gleeble system used for compression, (b) close up of the specimen placed between the anvils, (c) schematic figure showing the specimen and one of the ISO-T anvils.

The position of the movable anvil can be controlled and measured by two

separate systems, the stroke and the L-Gauge. The stroke, linked to the hydraulic servo system, is preferably used for compression control. The L-Gauge, measuring the position closer to the specimen, facilitates more precise compression measurements, as it is less influenced by the compliance of the Gleeble apparatus. However, complete separation of the compliance of the jaws, anvils, Ni-paste, and graphite foil, from the actual compression of the specimen is not possible. To minimise this contribution, a low force was applied to compress and secure the Ni-paste and the graphite foils before initiating the testing. The displacement measured by the L-Gauge was used for generating the stress-strain curves presented in Chapter 5 and in Papers I and II.

Temperature control in a Gleeble is typically achieved through the use of thermocouples, either welded to the specimen surface or inserted into holes drilled in the specimen. However, due to the ceramic character of $Mo(Si,Al)_2$, neither drilling nor welding was possible. Attempts to attach thermocouples using high temperature ceramic paste were made but failed as contact between the thermocouple and specimen could not be secured. Since resistive heating was employed to heat the specimen exclusively, a pronounced temperature gradient was expected in the paste. Calibration of the system using a steel specimen revealed that the temperature within the paste was approximately 120 °C lower than the temperature measured directly on the surface.

Instead of using thermocouples, a pyrometer, measuring the thermal radiation emitted from the specimen surface, was employed for temperature control. Any changes in surface properties, such as oxidation, lead to a corresponding change in radiation. Despite being tested in (low) vacuum, the $Mo(Si,Al)_2$ specimen was shown to oxidise to some extent. This affected the temperature reading by the pyrometer and the subsequent temperature control, leading to overshooting of the temperature.

To ensure a consistent specimen temperature, a thin and flexible graphite foil was wrapped around the specimen and secured with Pt-wires. Since the surface of the foil does not change with time, the thermal radiation will stay constant. The pyrometer was calibrated up to 1100 °C using a steel specimen. The temperature difference between thermocouples welded to the surface and that recorded by the pyrometer was found to be within the range of $\pm$ 10 °C. A schematic drawing and a photograph of the specimen wrapped with graphite foil are shown in Figure 4.2.

For higher temperatures, at which the steel specimen could not be used, the reliability of the system was validated using a polycrystalline $MoSi_2$ specimen tested in compression at 1300 °C. A similar experiment was conducted by Mitra et al. in [26]. The stress values measured in the current study matched those presented by Mitra et al.

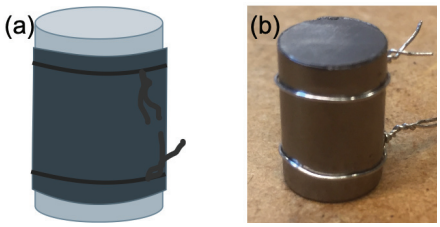

Figure 4.2: (a) Schematic figure, (b) photo of the test specimen with graphite foil and Pt-wires.

Upon validation, a testing protocol was established. Initially, a compressive force of 0.4 kN was applied to ensure secure fixation of the specimen between the anvils. The initial heating took place with a constant power supply. At 450 °C, the temperature control was transitioned to the pyrometer. A heating rate of 50 °C/min was employed to reach 1300 °C, where the specimen was held for 30 seconds to achieve a stable temperature before testing.

The force, F, was measured and converted to stress, σ, by

$$\sigma = F/A \tag{4.1}$$

where A is the specimen area. The displacement measured by the L-Gauge was used to calculate compression in terms of strain, ϵ, using the change in length, ΔL, and the initial length of the specimen, L.

$$\epsilon = \Delta L/L \tag{4.2}$$

A stress-strain curve from a $Mo(Si,Al)_2$ specimen is shown in Figure 4.3.

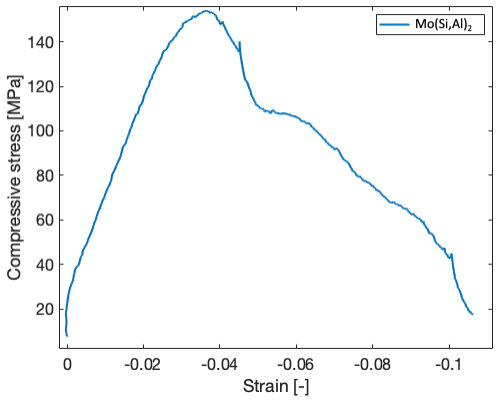

Figure 4.3: Stress-strain curve from a $Mo(Si,Al)_2$ specimen.

4.1.2 Four-point bending

Four-point bending was carried out by Fraunhofer IKTS, Dresden, Germany. The bending bars (43–50 x 3 x 4 mm) were prepared through grinding and the tests were performed following the DIN EN 820-1 standard utilizing a Shimadzu AG-20kNG testing machine. As schematically shown in Figure 4.4(a), the support span was 40 mm, and the loading span was 20 mm.

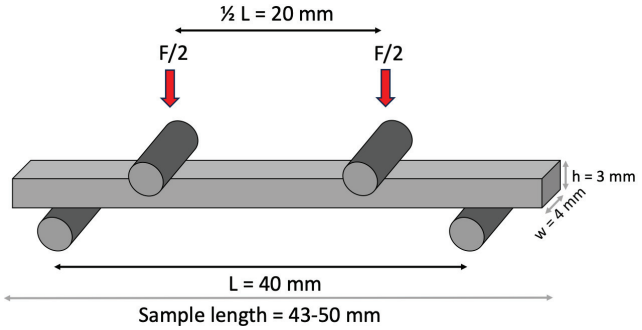

Figure 4.4: (a) Schematic illustration of the four-point bending setup.

The bending tests were carried out in vacuum ($1{\cdot}10^{-5}$ mbar) at 1300 °C. The heating rate was set to 10 °C/min, and the holding time for temperature homogenization was 10 min. The displacement rate, measured at loading points, was 0.5 mm/min. The maximum displacement was limited to approximately 1 mm. The loading force data was recorded and used to plot stress-displacement curves using the following equation,

$$\sigma_{max} = \frac{3}{4}\frac{FL}{bh^2} \tag{4.3}$$

where F is the force, L is the loading span distance, b and h are the width and height of the bending bar.

In contrast to the compression-tested specimens, the specimens subjected to four-point bending underwent external heating rather than resistive heating. The temperature was measured using thermocouples within the furnace. Notably, for the $Mo(Si,Al)_2$-Al_2O_3 composites, it was observed that the temperature fluctuated in a sinusoidal pattern between 1300 °C and approximately 1325 °C, due to problems with the temperature control of the furnace. As can be seen in Figure 4.5, the impact of this variation in temperature on the stress response is evident. To improve the readability of the stress-displacement curves, the data was filtered using a band stop filter (0.05–0.06 Hz). This successfully filtered out the temperature effect on the stress data, see Figure 4.5.

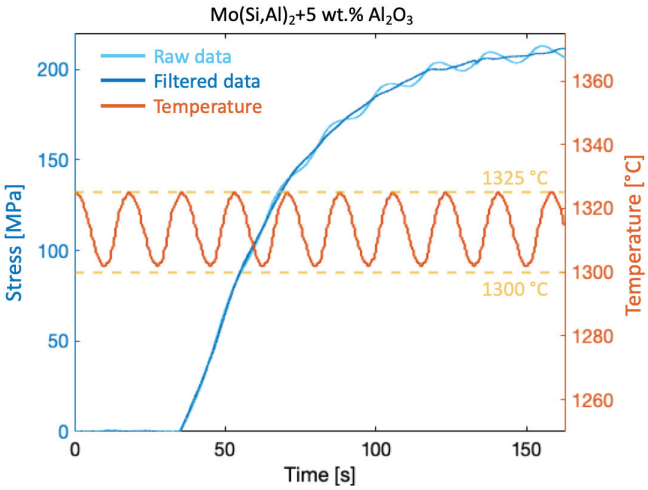

Figure 4.5: Temperature fluctuation and stress as a function of time in four-point bending of $Mo(Si,Al)_2$-Al_2O_3 composite.

The temperature control was improved before the $(Mo,W)(Si,Al)_2$ materials were tested, see Figure 4.6. As can be seen from the close-up in the same figure, the new temperature remained stable at 1300 °C throughout testing. Therefore, no filtering of the stress data was needed.

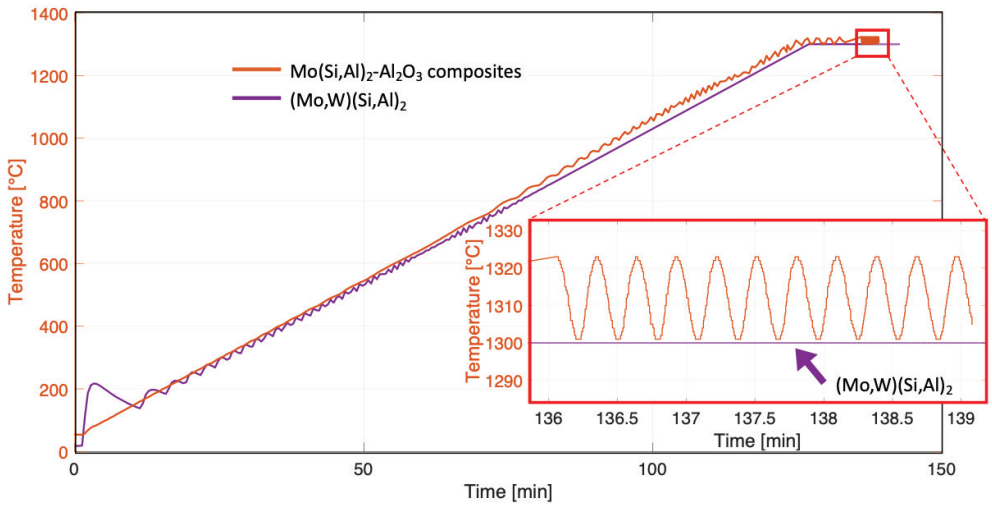

Figure 4.6: Temperature profiles from four-point bending testing of $Mo(Si,Al)_2$-Al_2O_3 composites and $(Mo,W)(Si,Al)_2$ materials.

4.2 Oxidation

The oxidation behaviour of Y-alloyed $Mo(Si,Al)_2$ was investigated by oxidation tests conducted in air at 1500 °C for durations up to 250 hours. Before exposure, the materials underwent grinding with 500 mesh SiC paper and were cut into cylindrical specimens. Three specimens of each composition were prepared and placed in a box furnace, which was then heated to 1500 °C with a ramp time of five hours. After 24 hours, the furnace was turned off. Once the temperature had dropped below 200 °C, the furnace was opened, and one sample of each composition was extracted for microstructure analysis. Simultaneously, another sample from each composition was weighed for a mass-gain study and reintroduced into the furnace. The furnace was subsequently reheated to 1500 °C. After an additional 26 hours, the procedure was repeated. The remaining samples were retrieved after a total exposure time of 250 hours. The procedure is illustrated in Figure 4.7.

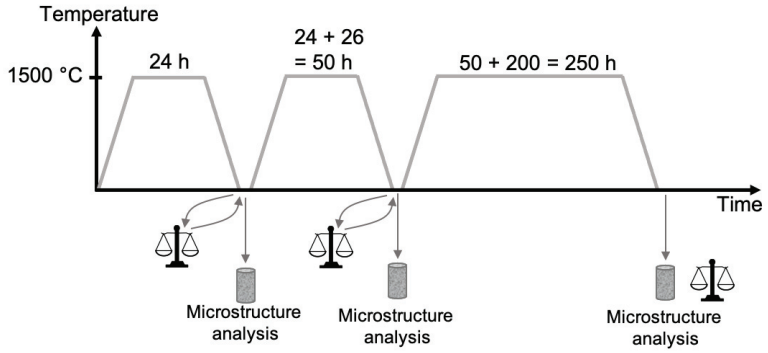

Figure 4.7: Schematic illustration of the oxidation cycle.

4.3 Microstructure analysis

Various methods have been used to investigate the microstructure of the materials studied in this thesis. X-ray diffraction, including synchrotron and laboratory X-rays, has been used to analyse crystal structure-related properties and phase fractions. Scanning electron microscopy (SEM)-based techniques have been employed for imaging, chemical composition analysis, determination of grain size and shape, as well as for deformation studies. The methods are complementary but exhibit overlaps in certain aspects. The subsequent sections, which offer a brief introduction to the methods used, aim to elucidate how and why these methods were employed for the microstructural investigations conducted in this thesis.

4.3.1 Laboratory X-ray diffraction

Laboratory X-ray diffraction (LXRD) has served as the primary method for initial characterisation, focusing primarily on phase identification. X-rays are generated through the interaction of electrons, accelerated from a tungsten filament, with a metal anode (commonly Cu or Mo). The interaction produces a continuous X-ray spectrum, which is then filtered to yield a monochromatic X-ray beam. The beam is directed onto the sample at an incident angle θ, as shown in Figure 4.8.

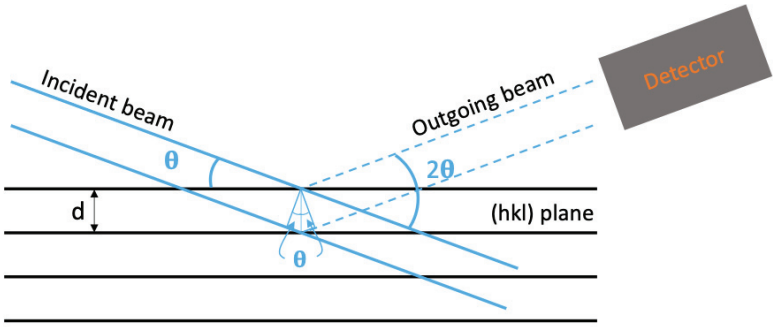

Figure 4.8: The Incident X-ray beam is diffracted by the (hkl)-planes. The incident angle is θ and the d is the interplanar spacing.

If Bragg's law,

$$n\lambda = 2d\sin(\theta) \tag{4.4}$$

where n is an integer and d is the interplanar spacing, is satisfied, the diffracted X-rays generate peaks in an XRD pattern, which can be used for phase identification. Figure 4.9 shows the XRD pattern of a $Mo(Si,Al)_2$ sample.

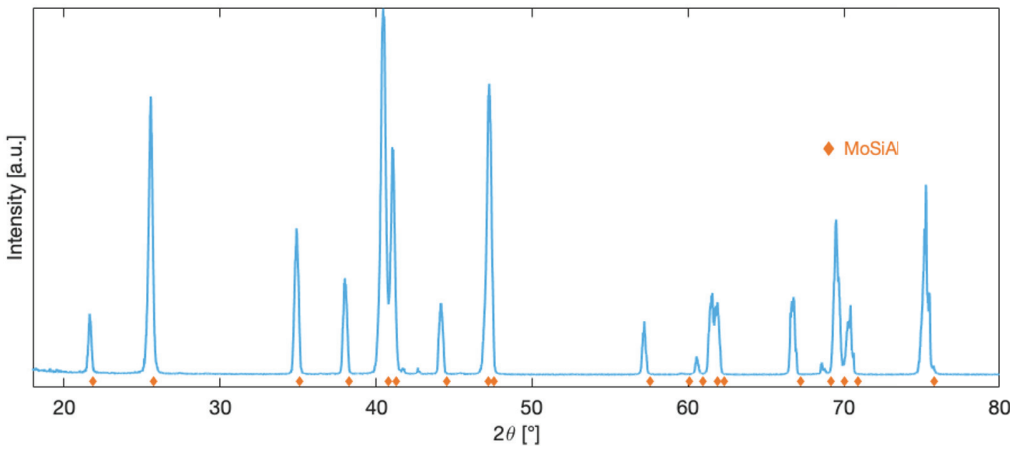

Figure 4.9: XRD pattern of a $Mo(Si,Al)_2$ material. The slight shift in 2θ is due to small differences in the chemical composition of the analysed material and the material on which the XRD card was based (PDF 00-057-0374).

LXRD is a versatile characterisation method. The area illuminated by the X-ray beam is approximately 1 cm^2 or less, and the depth of the investigated region is in the order of a few μm. Due to the relatively large volume investigated, LXRD provides better statistics than electron backscatter diffraction (EBSD), an SEM-based method used for investigating crystal structure-related properties which will be discussed later. LXRD is a rapid method which typically requires no special sample preparation. However, LXRD also has some limitations. For example, in a multi-phased material, only phases with a total volume fraction above 1–2 vol.% can be successfully identified. In the $Mo(Si,Al)_2$ materials investigated in this thesis, the volume fractions of some phases were below this value. Another challenge when investigating the multiphased $Mo(Si,Al)_2$ materials is the overlapping peaks in the diffractograms. These overlaps occur because the materials comprise at least four different phases, which all possess low symmetries.

Three different LXRDs were used in this thesis: a Bruker D8 Discover and two different Bruker D8 Advance systems, all equipped with a Cu anode. The step size, time per step, 2θ range and instrument configurations were varied to best suit the analysis objectives. The following powder diffraction files (PDF) were used for phase identification: C40: PDF 00-057-0374, $D8_m$: PDF 00-017-0415, $D8_8$: PDF 00-029-1362, Al_2O_3: PDF 00-042-1468.

4.3.2 Synchrotron X-ray diffraction

To investigate the low-volume fraction phases, synchrotron X-ray diffraction (SXRD) was employed. A significant advantage of synchrotron diffraction compared to LXRD is the very high flux (photons per second), resulting in a high signal-to-noise ratio. Furthermore, the synchrotron X-ray beam is more monochromatic and parallel, which gives rise to a diffractogram with high resolution. This reduces the problems associated with overlapping peaks in multi-phased materials, see Figure 4.10.

In this thesis, synchrotron experiments were conducted at Petra III, DESY, in Hamburg, Germany. Electrons are accelerated and injected into a storage ring, where they generate X-rays as they pass through periodic magnetic structures. Beamlines, connected to the storage ring, serve as stations where specimens are investigated. The beam is directed onto the specimen using optical devices and the diffracted signal is detected by one or several detectors.

The SXRD experiments in this thesis have been performed at two beamlines, P02.1 and P21.2, in transmission mode, where the specimen is placed in front of the detector(s). Figure 4.11(a) shows the setup used at the P21.2 beamline. The specimen consisted of a 1 mm thick slice cut from the material. Using a

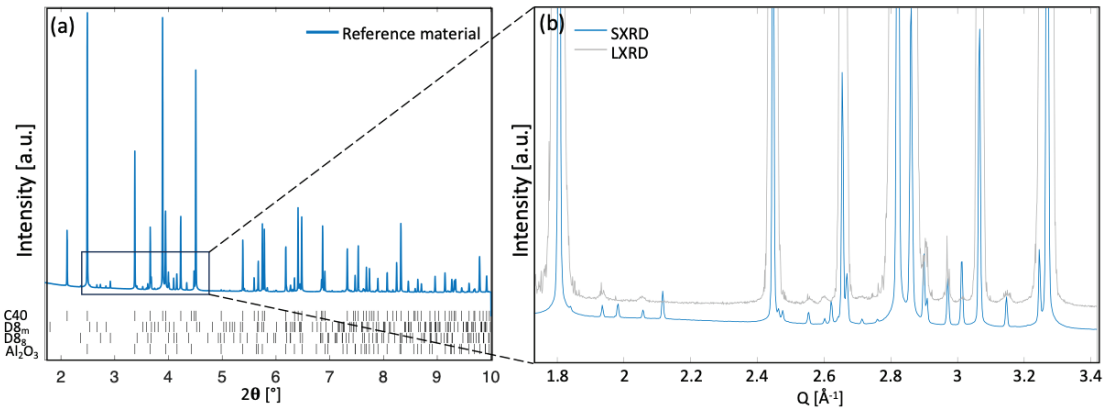

Figure 4.10: (a) Indexed SXRD diffractogram of the reference material (b) Magnified region from (a) and LXRD data plotted as a function of Q.

beam size of 150 x 150 µm, and moving the specimen vertically, diffractograms from different locations were obtained. Diffractograms collected from the centre of the specimens were used in Paper IV. A similar experimental setup was used for the experiment at the P02.1 beamline, but instead of a solid piece of material, a powder-filled capillary was used, see Figure 4.11(b). Site-specific diffractograms could not be achieved from these measurements.

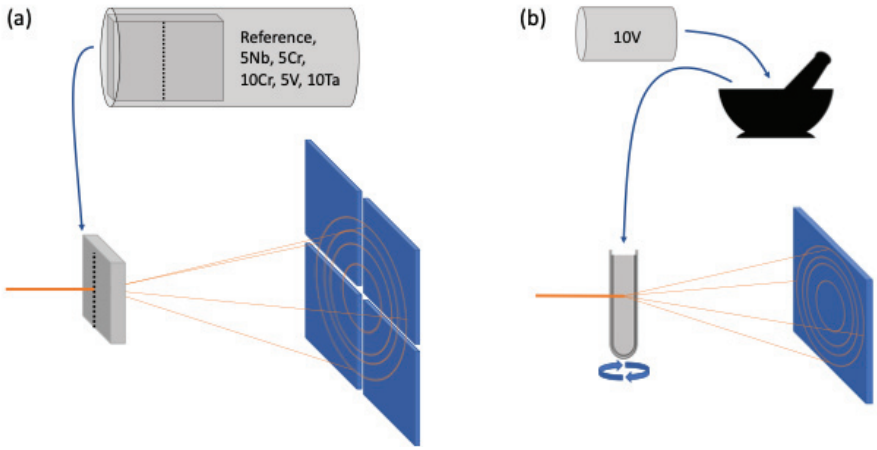

Figure 4.11: Experimental setup used for SXRD at the (a) P21.2 and (b) P02.1 beamline.

4.3.3 Rietveld refinements

The SXRD data were analysed using the Rietveld method, facilitating the extraction of properties such as the volume fraction of phases and the size of the unit cells. As the Rietveld method is based on least squares fitting of experimental data, it is important to note that the calculated values are not

always physically meaningful. To obtain reliable and useful values, care must be taken during the refinement and constraints are often needed.

In paper IV, Rietveld refinement of synchrotron data was employed to obtain the lattice parameters of the C40 phase and the volume fractions of the phases in the materials. Figure 4.12 shows a refinement of the reference material. Due to overlaps, particularly in the case of Al_2O_3, a combination of Rietveld refinement and BSE/SE image analysis was used to obtain the phase volume fractions.

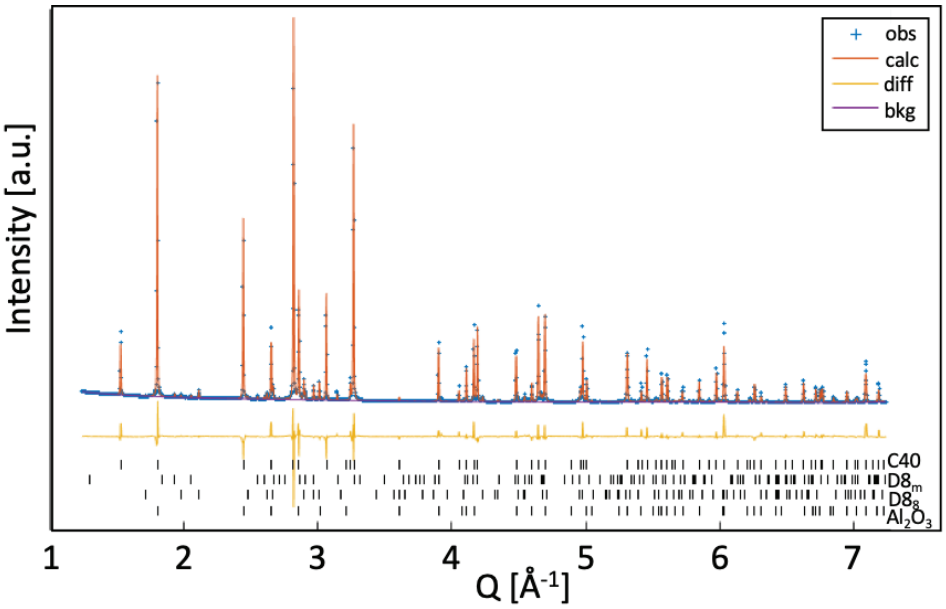

Figure 4.12: Rietveld refinement of $Mo(Si,Al)_2$ using GSAS-II. R_w=2.10 %.

4.3.4 Sample preparation for scanning electron microscopy

To examine the specimen surface in SEM, careful preparation is essential. In this work, specimens were mounted in conducting Bakelite and polished to a mirror-like finish using SiC-paper (up to 4000 grit), diamond suspensions (3 and 1 μm), and oxide polishing (colloidal silica). The oxide polishing step is crucial for EBSD measurements to prevent scratches from previous polishing steps to retain and create artefacts on the EBSD maps. After polishing, the specimens were cleaned in ethanol using an ultrasonic bath. To prevent polishing residues from being trapped in pores, the specimens were placed in plastic caps with the polished surface facing down. A rim, not in contact with the specimen, but with the surrounding Bakelite, separated the specimen from the cap. After drying and gluing onto SEM holders, specimens were stored in a desiccator to avoid oxidation.

4.3.5 Imaging using scanning electron microscopy

When the electron beam in an SEM scans the specimen surface, two types of scattered electrons, secondary electrons (SE) and backscattered electrons (BSE) are generated [65]. The SEs, primarily utilized in this work to study porosity, provide topographic contrast and originate from a sample depth of a few nanometers. In Figure 4.13(a), the pores in a $Mo(Si,Al)_2$-based material are visible as dark regions with bright edges.

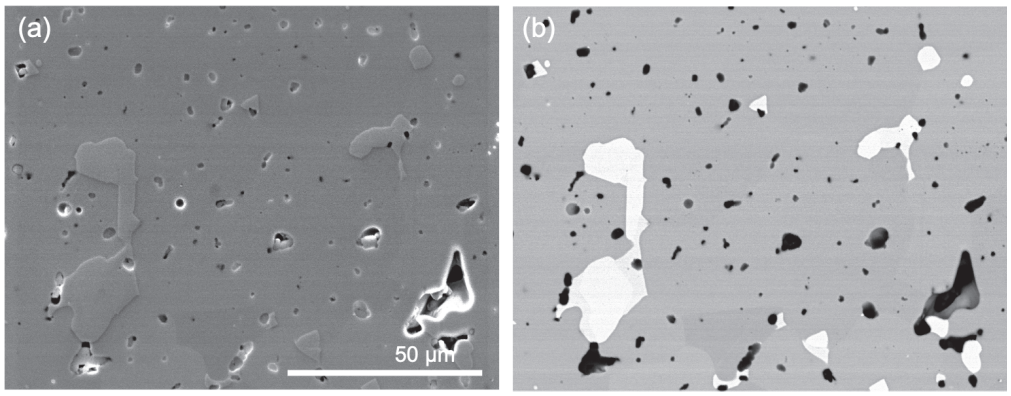

Figure 4.13: (a) SE, and (b) BSE image of a $Mo(Si,Al)_2$ material.

Figure 4.13(b) shows the BSE image of the same region. The contrast in BSE images is related to the atomic number of the elements [65]. The heavier the element, the more it scatters and the brighter the contrast. Lighter elements appear darker due to lower scattering [65]. In Figure 4.13(b), the grey matrix phase is $Mo(Si,Al)_2$, the bright regions are $Mo_5(Si,Al)_3$ grains ($D8_m$- or $D8_8$-structured, similar contrast because of very similar chemical composition), and the dark regions are either Al_2O_3 or pores. The pores appear dark since only a very low signal escapes the voids and hits the detector, while Al_2O_3 is dark due to its low average atomic number. Combining BSE and SE images using software such as GIMP [66] and ImageJ [67], enables the calculation of phase fractions. Unlike SXRD, this method also allows for the estimation of porosity.

4.3.6 Energy dispersive X-ray spectroscopy

Energy dispersive X-ray spectroscopy (EDS) was used to determine the chemical composition of the phases in the materials. The interaction of the electron beam with the specimen surface generates characteristic X-rays, producing an energy spectrum, see Figure 4.14(a), from which the chemical composition can be calculated [65]. Scanning the electron beam over the sample surface allows for the construction of maps showing the occurrence of different elements, see Figure 4.14(c). Since the EDS signal is generated from a larger sample volume,

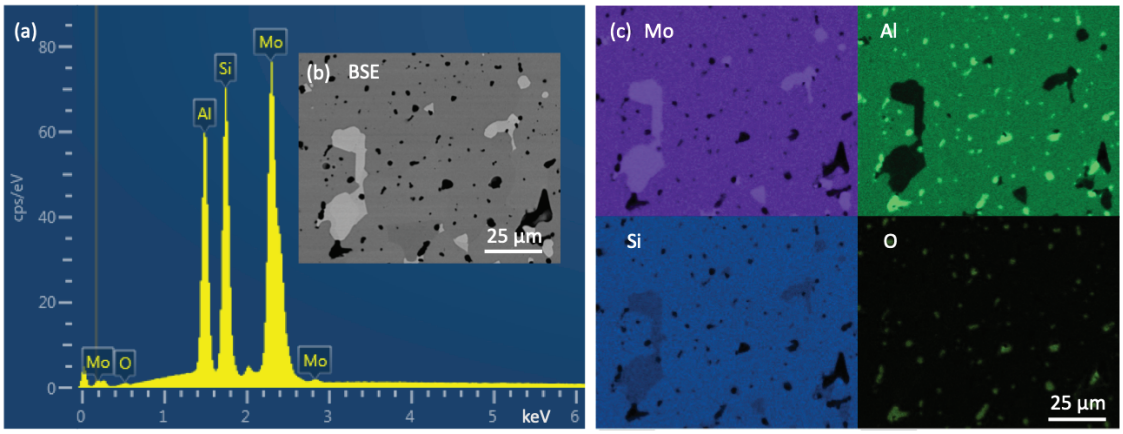

Figure 4.14: (a) Energy spectrum from $Mo(Si,Al)_2$, (b) BSE image, (c) EDS maps (Mo, Al, Si, and O) of the same region.

the resolution of the EDS map is lower than that of SE and BSE images.

EDS is a useful, fast, and easy-to-use technique, and the EDS detector can be attached to many types of SEMs. However, EDS has certain limitations, particularly when qualitatively measuring light elements such as C or N, or when dealing with low concentrations of other elements (below a few at.%).

In the studies conducted for this thesis, an FEI Quanta 200 FEG ESEM microscope, operating at 20 kV, served as the primary instrument for EDS measurements, as well as for SE and BSE imaging.

4.3.7 Electron probe microanalysis/wavelength dispersive spectroscopy

For qualitative measurements of elements present in very low concentrations, electron probe microanalysis/wavelength dispersive spectroscopy (EPMA/WDS) was employed. The X-rays emitted from the specimen are used, but instead of being detected as an energy spectrum, the X-rays are diffracted by a curved crystal, allowing for only one specific X-ray line to reach the detector. Different crystals are used, designed to diffract X-rays originating from different elements. The intensity of the signal from the sample is then compared with a standard of known concentration.

The EPMA/WDS data presented in this thesis was obtained using a JEOL JXA-8530F Plus Hyper Probe equipped with five WDS detectors. The accelerating voltage was set to 10 kV to achieve the necessary overvoltage for efficient excitations of the chosen line for each element. In this work, the following crystals and lines were used: PETH for Mo Lα, Nb Lα and Ta Mα,

TAPL for Si Kα and Al Kα, LDE2H for C Kα, LIFL for Fe Kα, LDE1L for O Kα, and LIFH for V Kα.

Despite its capability to detect light elements and low concentrations, EPMA/WDS has some drawbacks. Unlike EDS, WDS cannot be attached to all SEM systems and is more expensive. Additionally, EPMA/WDS is time-consuming as only one element per crystal can be measured at a time.

4.3.8 Electron backscatter diffraction

EDS and BSE imaging serve the purpose of distinguishing phases with different chemistry from each other. However, identifying individual grains of the same phase can be challenging using these methods. Instead, this can be done using electron backscatter diffraction (EBSD), a technique reliant on crystallographic orientations rather than chemistry.

In contrast to the other SEM-based methods, the sample is mounted on a tilted (typically 70°) stage, see Figure 4.15(a). When the sample is illuminated by the electron beam, a pattern is observed on a detector, comprising a phosphorescent screen and a CCD camera. As the electron beam interacts with the material, electrons are scattered from a point near the surface. Some of these electrons are diffracted by the (hkl)-planes, indicated by the 'x' in Figure 4.15(b), to which they travel at an angle θ. If the diffraction satisfies Bragg's law (Equation 4.4), two diffraction cones, known as Kossel cones, separated by an angle 2θ, are formed [68]. Given the small angle, usually less than 2°, the Kossel cones are detected as two parallel lines on the detector screen, commonly referred to as Kikuchi lines [65, 68]. As the crystal contains different (hkl) planes, a pattern of intersecting Kikuchi lines, rather than just two lines, emerges on the screen. The configuration of these lines changes based on the crystal's orientation. Consequently, EBSD becomes a powerful tool for investigating the orientation of grains in crystalline materials. In Figure 4.16, the patterns corresponding to two C40 grains with different orientations, and one pattern from a $D8_m$ grain are shown.

EBSD is also useful when investigating deformed materials. The presence of geometrically necessary dislocations (GNDs) in a material causes a rotation of the lattice [69]. The local curvature of the lattice influences the diffraction of scattered electrons, enabling EBSD to measure the change in orientation within a grain [65], thus indicating the presence of GNDs. Worth noting is that only GNDs, and not statistically stored dislocations (SSDs, dislocations randomly trapped within the crystal [69]) can be measured by EBSD.

For each pixel in the investigated area, information such as crystal structure,

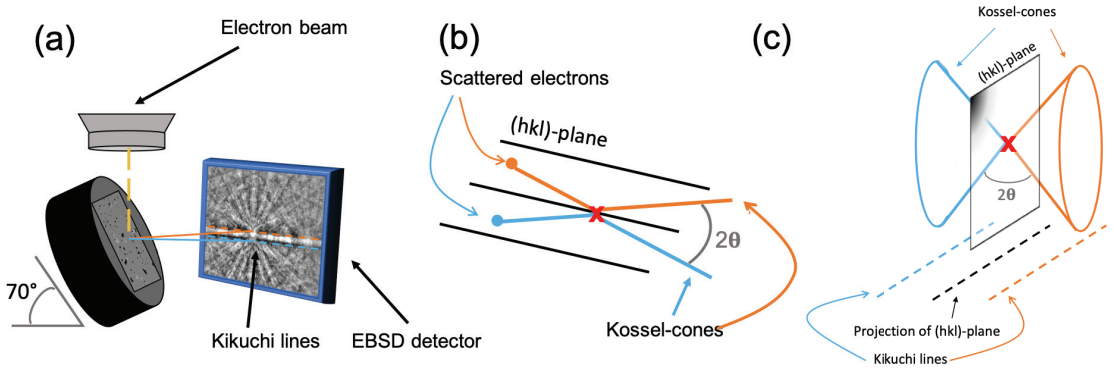

Figure 4.15: (a) The sample is placed on a 70° tilted stage under the electron beam. The Kikuchi patterns are detected by a CCD camera behind the detector. In (b) and (c) the scattering of electrons in the sample and the generation of Kossel cones are shown.

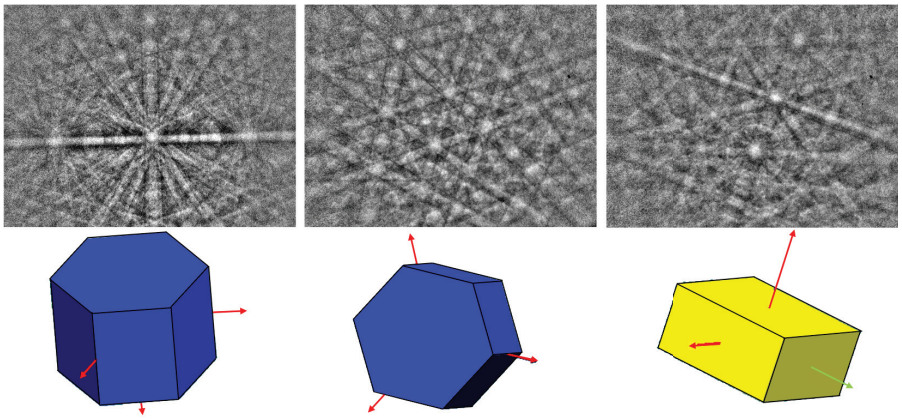

Figure 4.16: The Kikuchi pattern and orientation of two $Mo(Si,Al)_2$ and one $Mo_5(Si,Al)_3$ crystals.

orientation (in Euler angles) and pattern quality is recorded. This data is then used to construct EBSD maps using different software. In the studies presented in this thesis, two software have been used for this purpose, Channel 5 (Oxford Instruments) and the MATLAB-based software MTEX [70].

The maps in Figure 4.17 were generated using MTEX. Figure 4.17(a) shows a band contrast map, which indicates the quality of the pattern. Areas with low quality, such as grain boundaries, pores and highly deformed areas, are assigned a low band contrast value, and appear dark on the map. Unlike SE and BSE images and EDS maps (Figures 4.13 and 4.14, respectively), the EBSD maps allow for easy visualisation of the shape and size of individual grains in the $Mo(Si,Al)_2$ materials investigated in this thesis. Band contrast maps are often utilized as background layers in other EBSD maps.

Figure 4.17(b) and (c) show phase maps of a $Mo(Si,Al)_2$ material. Figure

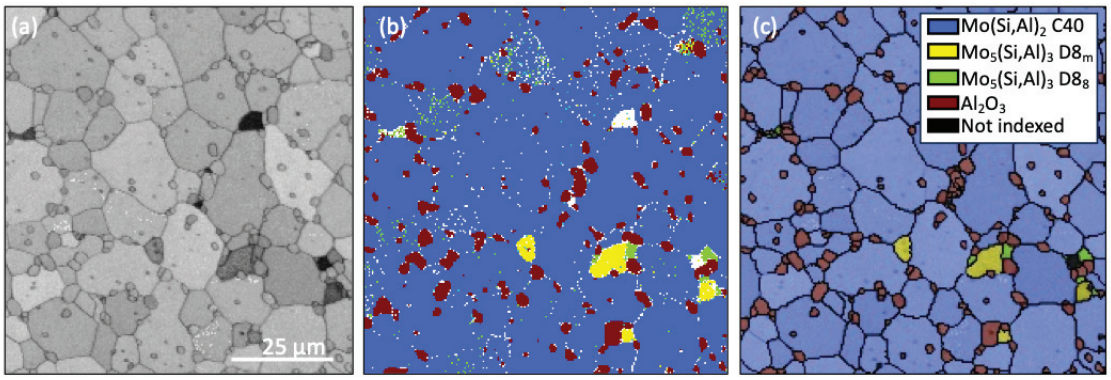

Figure 4.17: EBSD maps of $Mo(Si,Al)_2$: (a) band contrast, (b) phase map before cleaning, (c) phase map after cleaning with the band contrast map as background.

4.17(b) shows the raw indexing from the EBSD-detector in every pixel. White areas represent pixels that could not be indexed, possibly due to the poor quality of the Kikuchi pattern [65]. The map in Figure 4.17(c) shows the same area after cleaning the EBSD data in MTEX. Although the cleaning process varied slightly depending on the software used (MTEX or Channel 5), the cleaning steps were designed to result in similar maps.

The initial cleaning step in both Channel 5 and MTEX involved replacing unindexed or incorrectly indexed isolated pixels with copies of neighbouring pixels. In the next cleaning step, non-index areas comprising more than one pixel, but less than a user-defined value (depending on the software and parameters used for acquisition), were filled with information based on their neighbours. Larger regions, such as pores, were left unindexed. As a third step, grains were calculated and reconstructed using orientation data, employing a threshold misorientation angle of 10° for reconstruction. A pixel threshold value was applied to exclude very small regions (e.g., incorrectly indexed pixels) from being counted as grains, with the specific threshold value varying based on the step size.

In addition to the band contrast and the phase maps shown in Figure 4.17, the EBSD data can be used to generate other types of maps. Examples of maps where the crystal orientation plays an important role are shown in Figure 4.18. The map shown in Figure 4.18(a) is an Inverse Pole Figure (IPF) map, where pixels are coloured based on their orientation relative to a predetermined coordinate system.

Figure 4.18(b) shows a Grain Reference Orientation Deviation (GROD) map. In this map, every pixel has been assigned a GROD value based on the misorientation between the pixel's orientation and the average orientation of the grain to which it belongs. By calculating the average GROD value of all pixels in a grain, a Grain Orientation Spread (GOS) map is generated. A GOS map

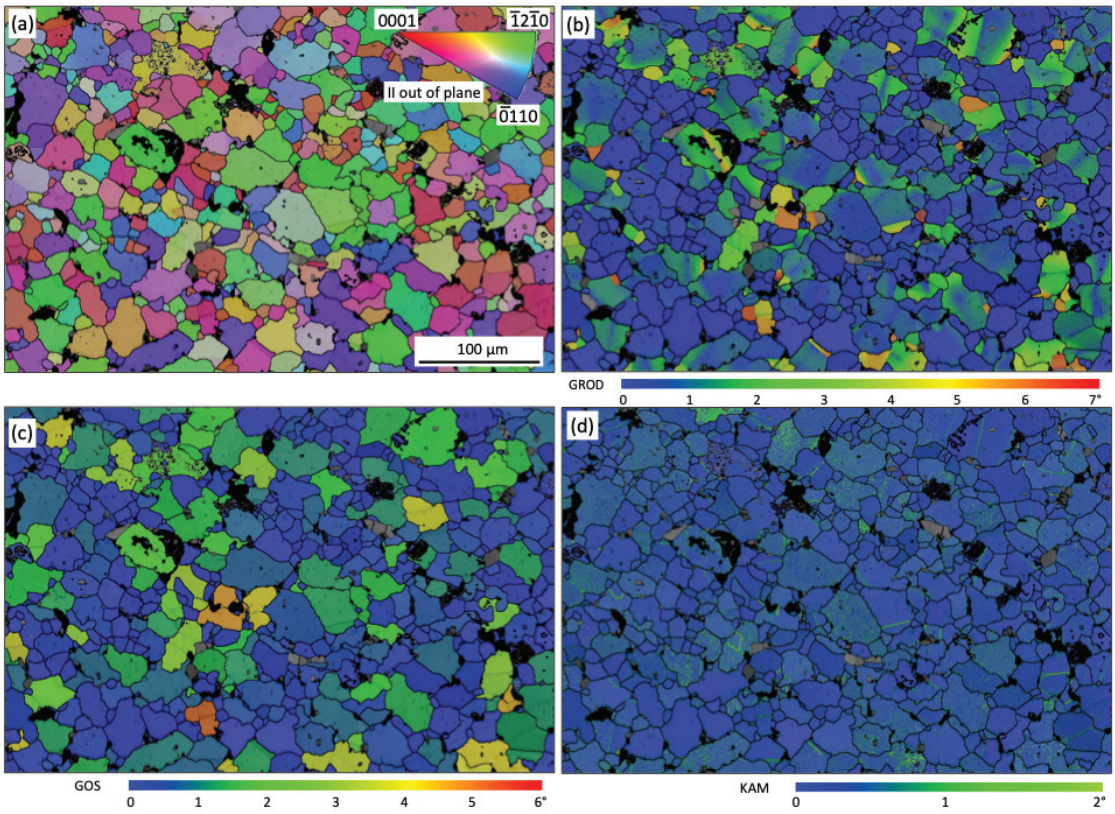

Figure 4.18: EBSD maps with C40 grains coloured based on (a) Inverse Pole Figure, (b) Grain Reference Orientation Deviation, (c) Grain Orientation Spread, (d) Kernel Average Misorientation.

is shown in Figure 4.18(c). Grains with higher GOS values are more deformed than those with lower values.

The map in Figure 4.18(d) is a Kernel Average Misorientation (KAM) map. In this map, the average misorientation between every pixel and its neighbouring pixels (within the same grain) is calculated. This map highlights regions with high local misorientation, such as highly deformed areas with a high density of (GNDs) and low-angle grain boundaries (LAGB).

4.3.9 Scanning transmission electron microscopy

Scanning transmission electron microscopy (STEM) was used to study dislocations in one of the compression-tested specimens. A lift-out of a grain containing a LAGB was prepared using focus ion beam in an FEI Versa 3D instrument equipped with an Omniprobe manipulator. STEM bright field (STEM-BF) investigation was conducted using an FEI Titan 80–300 instrument at 300 keV.

CHAPTER 5

Results and discussion

Research questions

This work has been conducted to answer the research questions presented in the first chapter of this thesis:

1. How does polycrystalline C40-structured $Mo(Si,Al)_2$ deform at high temperature?

2. Can the high temperature strength be improved through particle strengthening by adding Al_2O_3?

3. Is quaternary alloying of C40 possible, and how does it affect the strength?

4. How does alloying with yttrium affect the high temperature oxidation behaviour of $Mo(Si,Al)_2$?

In this chapter, the results from the attached papers, along with unpublished data, will be used to answer the questions one by one.

5.1 Research question 1 - How does polycrystalline C40-structured $Mo(Si,Al)_2$ deform at high temperature?

Before this thesis: Limited attention has been given to the investigation of the deformation behaviour of C40-structured $Mo(Si,Al)_2$ previously. A DBTT of 1250 °C, and a rapid decrease in strength above this temperature have been reported [22], but no stress-strain data or microstructural investigation of deformed materials have been published.

In this thesis: This doctoral thesis comprises three papers focusing on high-temperature mechanical properties of $Mo(Si,Al)_2$: Papers I, II, and III. Among these, Paper I is most significant for answering the first research question as it elucidates both intra- and intergranular deformation mechanisms. Within this paper, both stress-strain data and microstructure analyses of deformed $Mo(Si,Al)_2$ are presented. In Papers II and III, the grain size sensitivity is discussed.

5.1.1 The $Mo(Si,Al)_2$ material before deformation

The material best illustrating the various deformation mechanisms in polycrystalline $Mo(Si,Al)_2$ is the unalloyed material without any addition of Al_2O_3. This material was synthesised as described in Chapter 3, using the large furnace for the reaction and the Mo-lined container with Mo balls for milling. The absence of Al_2O_3 leads to grain growth during sintering, resulting in a coarse-grained material, which was shown to be crucial for intragranular deformation of C40-structured $Mo(Si,Al)_2$. The material had an average grain size of 21 μm and a density of 5.74 g/cm^3, which corresponds to 96 % of theoretical density. The density is affected by pores (approximately 1 vol.%, based on BSE and SE image analysis) and secondary phases.

A BSE image of the microstructure is shown in Figure 5.1(a). As described in Section 4.3.5, the grey phase is C40-structured $Mo(Si,Al)_2$, the bright phase is $Mo_5(Si,Al)_3$, and the dark phase is either Al_2O_3 or pores. The chemical composition of C40 can be seen in Table 5.1. The O content is due to the presence of intragranular nano-sized Al_2O_3 particles, and C is a contamination from synthesis.

Based on Mo-Si-Al phase diagrams and LXRD data, all $Mo_5(Si,Al)_3$ grains were assumed to be $D8_m$-structured in Papers I and II. However, subsequent SXRD experiments indicated the presence of an additional $Mo_5(Si,Al)_3$ phase, $D8_8$, also called 'Nowotny phase', stabilised by C [71, 72]. The higher C content in this phase can be seen in Table 5.1. Also worth noting is that this phase has a slightly higher Al content than $D8_m$. An EBSD map showing all phases

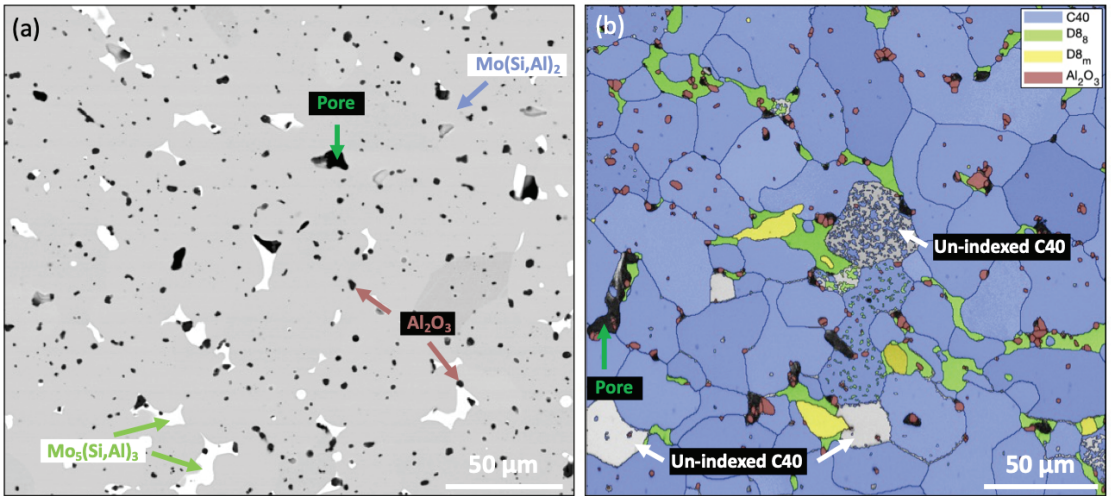

Figure 5.1: (a) BSE image and (b) EBSD map of $Mo(Si,Al)_2$.

Table 5.1: Chemical composition of C40, $D8_m$ and $D8_8$ in $Mo(Si,Al)_2$ (from EPMA-WDS).

Phase	**Chemical composition (at.%)**				
	Mo	**Si**	**Al**	**C**	**O**
C40	31	36	32	0.8	0.7
$D8_m$	61	31	6	1.3	0.5
$D8_8$	57	28	9	6	0.2

in the material can be seen in Figure 5.1(b), and an SXRD diffractogram of the material is shown in Figure 5.2(a).

Table 5.2 presents the phase volume fractions of the material, measured using three different methods: BSE/SE image analysis, EBSD indexing, and Rietveld refinement of SXRD data. Due to the similar chemical composition of $D8_m$ and $D8_8$, it is not possible to differentiate between the two phases using the BSE/SE image analysis. Therefore, the total volume of these two phases is presented. As this method investigates the microstructure on a local scale, several images were combined for better statistics. This data was presented in Paper I.

From the second method, EBSD indexing, the volume fractions of both $D8_m$ and $D8_8$ can be estimated as the two phases possess different crystal structures. Similar to BSE/SE, the investigated area is relatively small (in this study typically 250 x 250 µm). Another drawback with this method is that a well-indexed EBSD map is needed. As can be seen from Figure 5.1(b), the investigated materials had regions with un-indexed pixels, which affects the calculated volume fractions. Additionally, small pores might have been erased

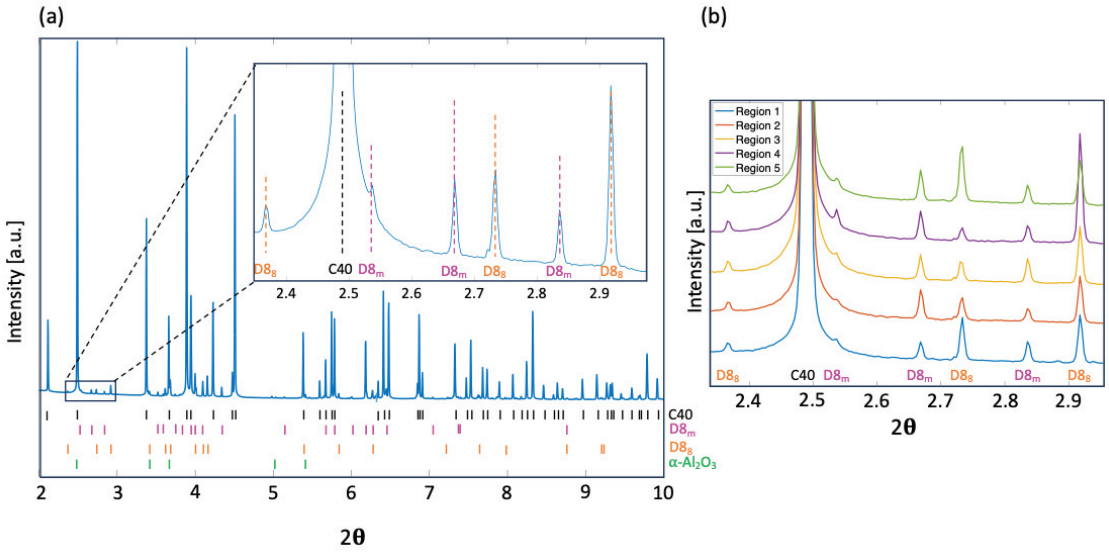

Figure 5.2: (a) SXRD pattern of the $Mo(Si,Al)_2$ material. The magnified region shows the presence of $D8_m$ and $D8_8$, (b) the five individual SXRD patterns used to construct the SXRD pattern shown in (a).

Table 5.2: Phase volume fraction of the $Mo(Si,Al)_2$ material using three methods. *Sum of $D8_m$ and $D8_8$.

Method	**Volume fraction (%)**				
	C40	**$D8_m$**	**$D8_8$**	**Al_2O_3**	**Pores/not indexed**
BSE/SE image analysis	94		3*	2	1
EBSD indexing	85	1	5	2	6
Rietveld refinement	85	2	3	10	-

during the cleaning procedure.

The third method, Rietveld refinement of SXRD data, gives better statistics. The diffractogram used for the volume fraction analysis, presented in Figure 5.2(a), was constructed by combining five synchrotron measurements, each covering a volume of approximately 0.15 x 0.15 x 1 mm (see Section 4.3.2 for details). The five individual diffraction patterns are depicted in Figure 5.2(b). It can be seen that the intensity, and thus the phase volume fractions, varies within the specimen. Combining the data provides a more accurate estimation of the volume fractions, although this method does not allow for the estimation of porosity. The Rietveld refinement yielded a relatively high Al_2O_3 content, possibly overestimated due to overlapping peaks in the diffractogram.

Based on the values presented in Table 5.2 and the discussion above, it is

proposed that the $Mo(Si,Al)_2$ material consists of approximately 90 vol.% C40, along with small amounts of $D8_m$, $D8_8$, Al_2O_3, and pores. The low fractions of the $Mo_5(Si,Al)_3$ phases is not expected to significantly affect the mechanical properties of the material. Hence, these phases will not be further discussed in this section.

5.1.2 Mechanical response

Three $Mo(Si,Al)_2$ specimens underwent compression testing at 1300 °C using the experimental setup described in Section 4.1.1. The resulting stress-strain curves, shown in Figure 5.3(a), are, to the best of the author's knowledge, the first published stress-strain curves of polycrystalline C40-structured $Mo(Si,Al)_2$. Three regions, labelled I, II, and III, with different stress-strain behaviours, have been marked in the figure.

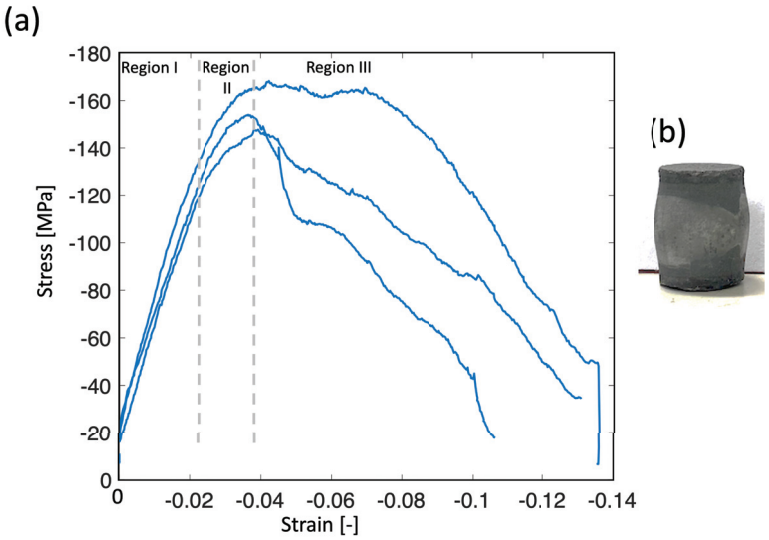

Figure 5.3: (a) Stress-strain curves of three $Mo(Si,Al)_2$ specimens compressed at 1300 °C. The intervals of the three regions are approximate. (b) Photo of a deformed specimen.

The initial linear segment of the curve (Region I) corresponds to elastic deformation. However, due to compliance in the Gleeble system (jaws, anvils, etc., see Section 4.1.1 for details), it was not possible to determine either Young's modulus or a precise yield point from the compression data. In the stress range of 120–140 MPa, the curves deviate from linearity, and the material undergoes plastic deformation and work hardening (Region II). The stress response increases until a strain of around 4 %, where the maximum stress (148–168 MPa) is observed. At higher strains (Region III), the stress decreases, and the material undergoes recovery. A photograph of a deformed specimen is shown in

Figure 5.3(b). No cracks were observed on the specimens after testing.

5.1.3 Intragranular deformation mechanisms

The microstructure of the deformed specimens was analysed using EBSD. It was shown that the grains had undergone plastic deformation during testing. When ellipses were fitted to the grains in the EBSD map of the deformed specimen, the major axis of the ellipses tended to be aligned perpendicular to the loading direction, indicating a typical 'flattening' of the grains under load. A histogram showing the grain shape of the deformed material and the as-sintered material is shown in Figure 5.4.

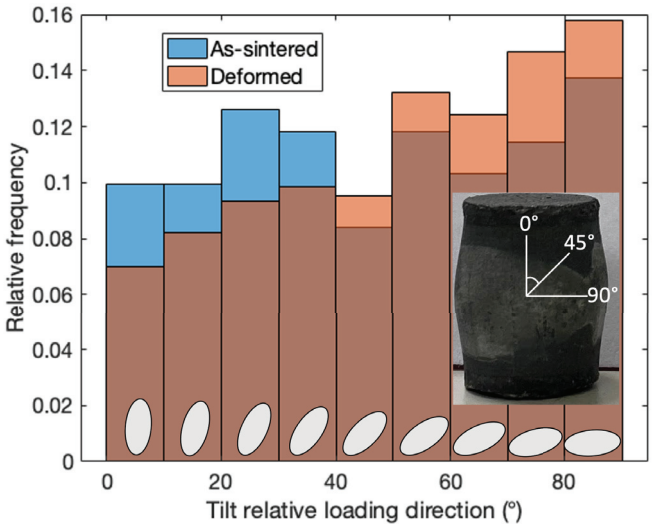

Figure 5.4: Histogram showing the direction (in degrees relative to the compression load axis) of the major axis of ellipses fitted to the grains.

Furthermore, EBSD analysis revealed the involvement of dislocations in the deformation of $Mo(Si,Al)_2$. In Figure 5.5, GOS maps of an as-sintered and a deformed specimen are presented. The low GOS values in the as-sintered material indicate a lattice relatively free from GND-induced rotation. The higher GOS values in the deformed specimen are attributable to plastic deformation.

In the compression-tested specimen, the deformation was inhomogeneous, with some grains more deformed than others. The more highly deformed grains (high GOS values) generally exhibited a high Schmid factor for the $(0001)\langle 1\bar{2}10\rangle$ system, the only slip system reported to be active in C40-structured $Mo(Si,Al)_2$ [23]. Interestingly, some grains with low Schmid factor also demonstrated relatively high GOS values.

Intragranular deformation patterns are evident in the GROD map presented in Figure 5.6. Notably, the deformation does not appear random; instead, the

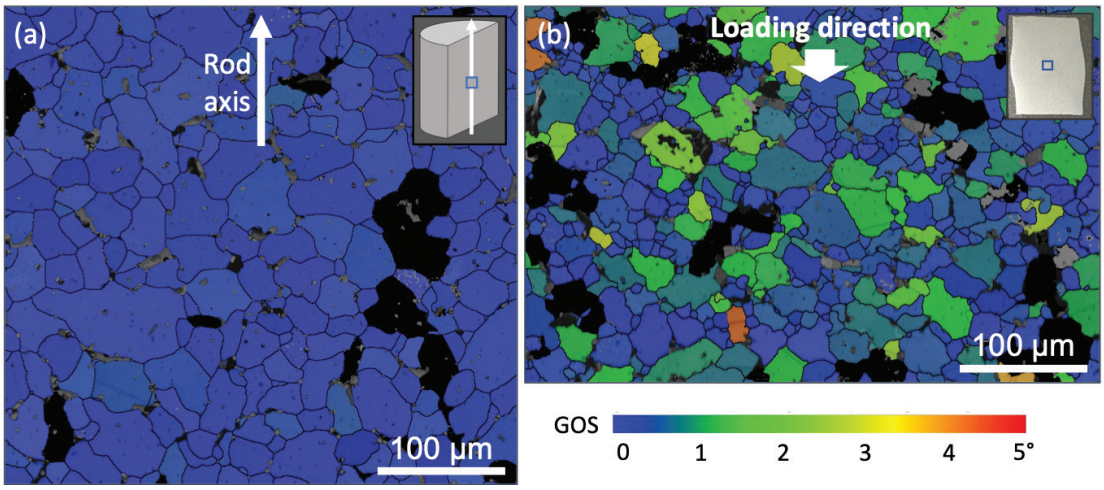

Figure 5.5: EBSD GOS maps of (a) as-sintered material, (b) compression-deformed specimen. The sites investigated by EBSD are indicated by the blue squares on the specimens inserted in the corners. Grains with incorrect indexing have been manually filled in black for clarity.

misorientation tends to increase in specific directions within the grains. This indicates that the deformation of $Mo(Si,Al)_2$ is inhomogeneous also on the intragranular scale.

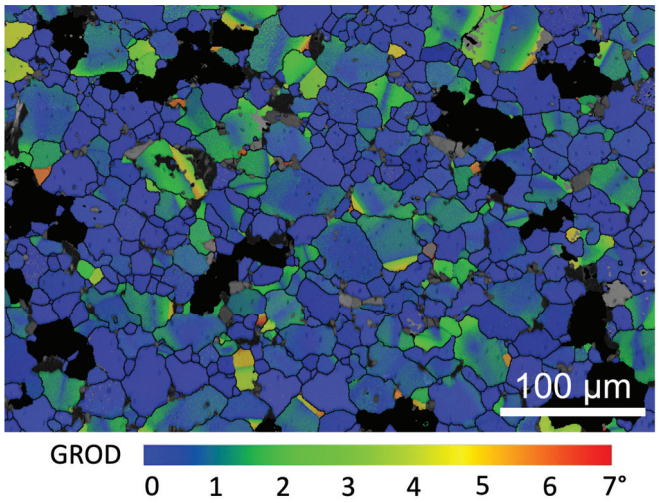

Figure 5.6: GROD map of deformed $Mo(Si,Al)_2$. Grains with incorrect indexing have been manually filled in black for clarity.

The direction in which the misorientation increases is often, though not always, aligned perpendicular to the crystallographic [0001] direction (the c-axis) of the grain, as shown in the misorientation profile of Line 1 in Figure 5.7(a). In contrast, parallel to the c-axis, the misorientation is much smaller and varies around 0.5°, as indicated by Line 2 in Figure 5.7(a).

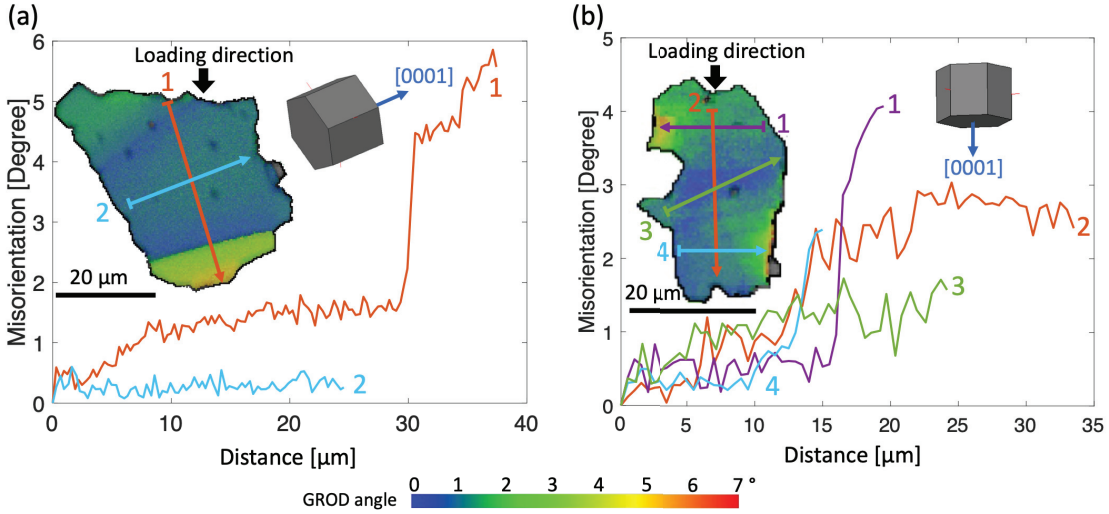

Figure 5.7: GROD maps and misorientation profiles of grain with (a) high Schmid factor and (b) low Schmid factor.

The grain shown in Figure 5.7(b) has a low Schmid value for the $(0001)\langle 1\bar{2}10\rangle$ slip system. The GROD map of this grain reveals a complex deformation pattern. In contrast to the grain in Figure 5.7(a), the change in misorientation parallel to the [0001] direction is relatively large (Line 2 in Figure 5.7(b)). This may indicate either the activation of additional slip systems or that the $(0001)\langle 1\bar{2}10\rangle$ system was activated through high shear forces from neighbouring grains. The activation of additional slip systems has previously been reported in C40-structured $NbSi_2$ in the presence of highly triaxial stress states around cracks [29]. It is possible that the local stress fields due to strain incompatibility between grains could allow activation of new slip systems in $Mo(Si,Al)_2$. Further research, including slip trace analysis using TEM, is required to investigate this.

5.1.4 Recovery processes

5.1.4.1 Formation of low-angle grain boundaries

Line 1 in Figure 5.7(a) exhibits a steep increase in misorientation, observed as a sharp change in colour from blue to yellow in the GROD map. In the KAM map of the same grain presented in Figure 5.8(a), this local change in orientation appears as a straight line with high KAM values, indicating that the build-up of dislocations has led to the formation of a LAGB. While the formation of LAGBs has not been previously reported in C40-structured $Mo(Si,Al)_2$, it has been observed in $C11_b$-structured $MoSi_2$ where it contributes to the recovery of the material [26]. In this work, LAGBs were identified in several

grains, and it is proposed that they contribute to the softening taking place in Region III of the stress-strain curves in Figure 5.3(a).

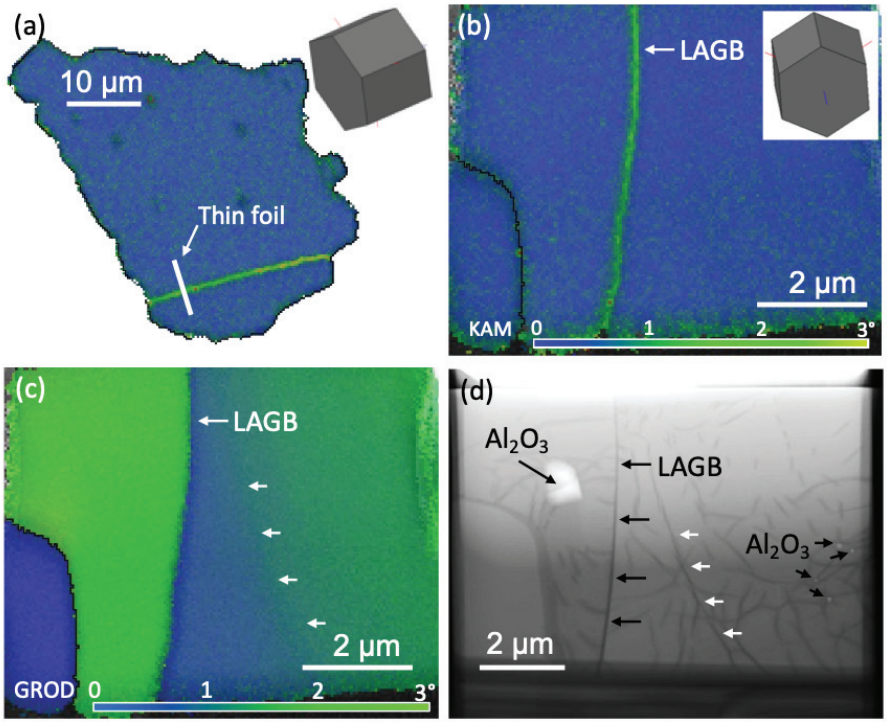

Figure 5.8: (a) KAM map of a grain in the deformed $Mo(Si,Al)_2$ specimen, (b) KAM map of the lift-out, (c) GROD map of the lift-out, (d) STEM-BF image of the lift-out. The KAM colour bar in (b) is valid also for (a).

To explore the LAGB further, a thin-foil lift-out was prepared using FIB (see Section 4.3.9). EBSD analysis of the thin-foil revealed the continuation of the LAGB beneath the sample surface (see Figure 5.8(b)). The corresponding GROD map in Figure 5.8(c) shows the misorientation close to the LAGB. The white arrows indicate a relatively sharp increase in misorientation, which could be an early stage in the formation of a new LAGB.

Figure 5.8(d) shows a STEM-BF image of the thin-foil lift-out. In this image, dislocations forming both the LAGB and the region suggested to develop into a new LAGB can be observed. Individual dislocations are also visible in other parts of the grain. Additionally, Al_2O_3 grains of various sizes are visible in bright contrast. The dislocations appear to be enriched in the vicinity of the Al_2O_3 grains, suggesting a potential particle strengthening effect on the material.

5.1.4.2 Dynamic recrystallization

Another mechanism suggested to contribute to the softening of $Mo(Si,Al)_2$ is dynamic recrystallization (DRX). While this phenomenon has been reported in $C11_b$-structured $MoSi_2$ [73], it has not been reported in C40-structured disilicides. In this work, DRX was indicated by a significantly smaller grain size in the deformed specimen compared to the as-sintered material, as illustrated in the grain size histogram in Figure 5.9(a). In Figure 5.9(b), GOS as a function of grain size is shown. As expected from DRX, the small (recrystallized) grains exhibit much lower deformation levels than the large grains. In the as-sintered specimen, the GOS values are similar for all grain sizes.

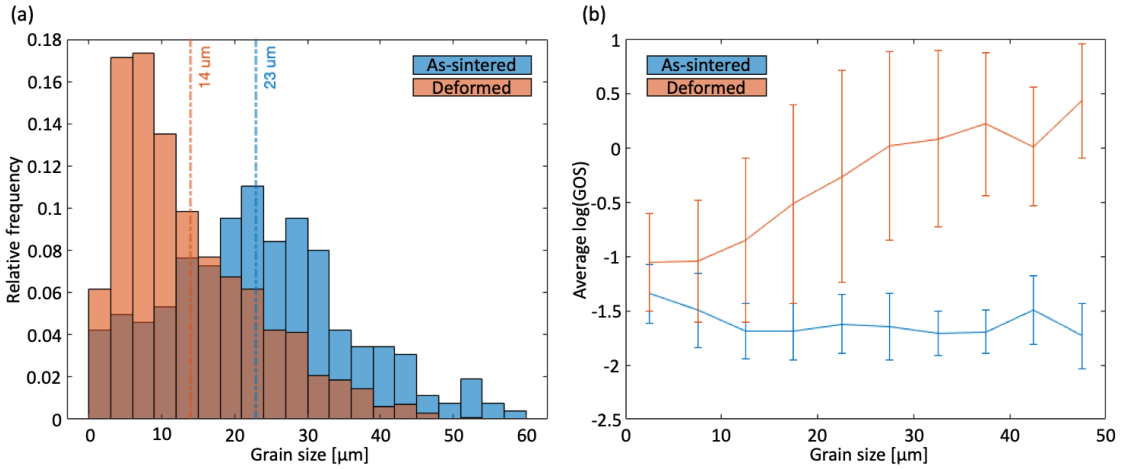

Figure 5.9: (a) Grain size distribution before and after deformation. The dashed lines indicate the average grain size. (b) GOS as a function of grain size.

5.1.5 Grain boundary sliding and grain size sensitivity

The stress levels towards the end of the compression tests are lower than expected from a material having DRX as its dominating softening mechanism. Therefore, it is likely that other deformation mechanisms, such as grain boundary sliding, are active during deformation.

The material discussed so far in this chapter had a coarse microstructure with large grains. However, as will be thoroughly discussed in 'Research question 2' (Section 5.2), the strength of polycrystalline $Mo(Si,Al)_2$ was shown to decrease with a reduction in grain size. This behaviour contradicts the Hall-Petch relationship,

$$\sigma_y = \sigma_0 + \frac{k}{\sqrt{d}} \tag{5.1}$$

in which the yield stress, σ_y, is inversely proportional to the grain size, d (σ_0 and G are material constants). However, the relationship between grain size and strength observed in this thesis exhibits similarities with materials deforming via grain boundary sliding during creep testing. Therefore, it is suggested that in addition to the glide of dislocations, $Mo(Si,Al)_2$ also deforms by grain boundary sliding. Furthermore, this mechanism, accommodated by diffusion of atoms, is suggested to be the dominating deformation mechanism, especially in fine-grained materials where the diffusion distances are short.

5.2 Research question 2 - Can the high temperature strength be improved through particle strengthening by adding Al_2O_3?

Before this thesis: Particle strengthening of C40-structured $Mo(Si,Al)_2$ has not been previously investigated. However, in $C11_b$-structured $MoSi_2$, the addition of C, leading to the formation of SiC particles, has been reported to improve the strength.

In this thesis: The impact of adding Al_2O_3 particles to $Mo(Si,Al)_2$ was explored in Papers II and III. It was shown that small additions resulted in fine-grained materials with lower strength. However, at high Al_2O_3 levels, a partial recovery of the strength was observed.

5.2.1 The $Mo(Si,Al)_2$-Al_2O_3 composites before deformation

In addition to the Al_2O_3-free material discussed in the previous section, six $Mo(Si,Al)_2$-Al_2O_3 composites, containing 5–30 wt.% Al_2O_3, were prepared to investigate the effect of particle strengthening. Table 5.3 provides details on the composites, including their theoretical density and the type of mechanical testing to which they were subjected.

The $Mo(Si,Al)_2$-Al_2O_3 composites were prepared in two batches, one for the compression tests and one for the four-point bending tests, using an identical process (see Chapter 3). Table 5.4 shows the density and phase volume fractions of the sintered composites. It can be seen that the density decreases as the volume fraction of Al_2O_3 increases (Al_2O_3 has a density of 3.99 g/cm^3). The chemical composition of the $Mo(Si,Al)_2$ phase remained the same in all materials (approximately 31 at.% Mo, 36 at.% Si, and 32 at.% Al), as the same $Mo(Si,Al)_2$ powder was used.

Table 5.3: $Mo(Si,Al)_2$-Al_2O_3 composites, density and mechanical testing. *TD = Theoretical density.

Material	**$Mo(Si,Al)_2$ (wt.%)**	**Al_2O_3 (wt.%)**	**TD* (g/cm^3)**	**Compression**	**Four-point bending**
A0	100	0	6.01	X	-
A5	95	5	5.86	X	X
A10	90	10	5.72	X	-
A15	85	15	5.59	X	X
A20	80	20	5.46	X	-
A25	75	25	5.34	X	X
A30	70	30	5.22	-	X

Table 5.4: Density and phase volume fraction in as-sintered $Mo(Si,Al)_2$-Al_2O_3 composites (from EBSD). *TD = Theoretical density.

Material	**Density (g/cm^3) (% of TD*)**	**Volume fraction (%)**			
		$Mo(Si,Al)_2$	**Al_2O_3**	**$Mo_5(Si,Al)_3$**	**Pores**
A0	5.7 (95.3)	95	1.7	3.0	1.1
A5	5.7 (96.9)	85	7.5	6.0	1.7
A10	5.6 (97.9)	81	14	4.7	0.1
A15	5.5 (97.9)	73	21	5.0	1.1
A20	5.3 (97.7)	68	27	4.3	1.5
A25	5.2 (97.4)	63	32	3.4	1.9
A30	5.1 (97.5)	57	38	2.6	1.9

From Figure 5.10(a)–(g), showing EBSD maps and BSE images of the as-sintered materials, it is evident that the grain size is larger in A0 than in the other materials. Figure 5.10(h) shows the grain size as a function of Al_2O_3. The figure clearly shows that even a small addition of 5 wt.% Al_2O_3 leads to a reduction in grain size, from above 20 μm to below 10 μm. This size reduction is a result of a grain boundary pinning effect from the particles during sintering. The same phenomenon has been reported in $MoSi_2$ when adding oxide particles or C, leading to the formation of SiC [37, 40]. In the case of A5, EBSD was employed to investigate four different regions, all located at the centre of the as-sintered rod. As shown in Figure 5.10(h), the average grain size of these regions varies. This indicates that even though the grain size is reduced, an addition of 5 wt.% Al_2O_3 is not enough to obtain a homogeneous microstructure.

Adding higher levels of Al_2O_3 leads to a further decrease in grain size (see A10 in Figure 5.10(h)). However, the decrease appears to saturate around 15 wt.%.

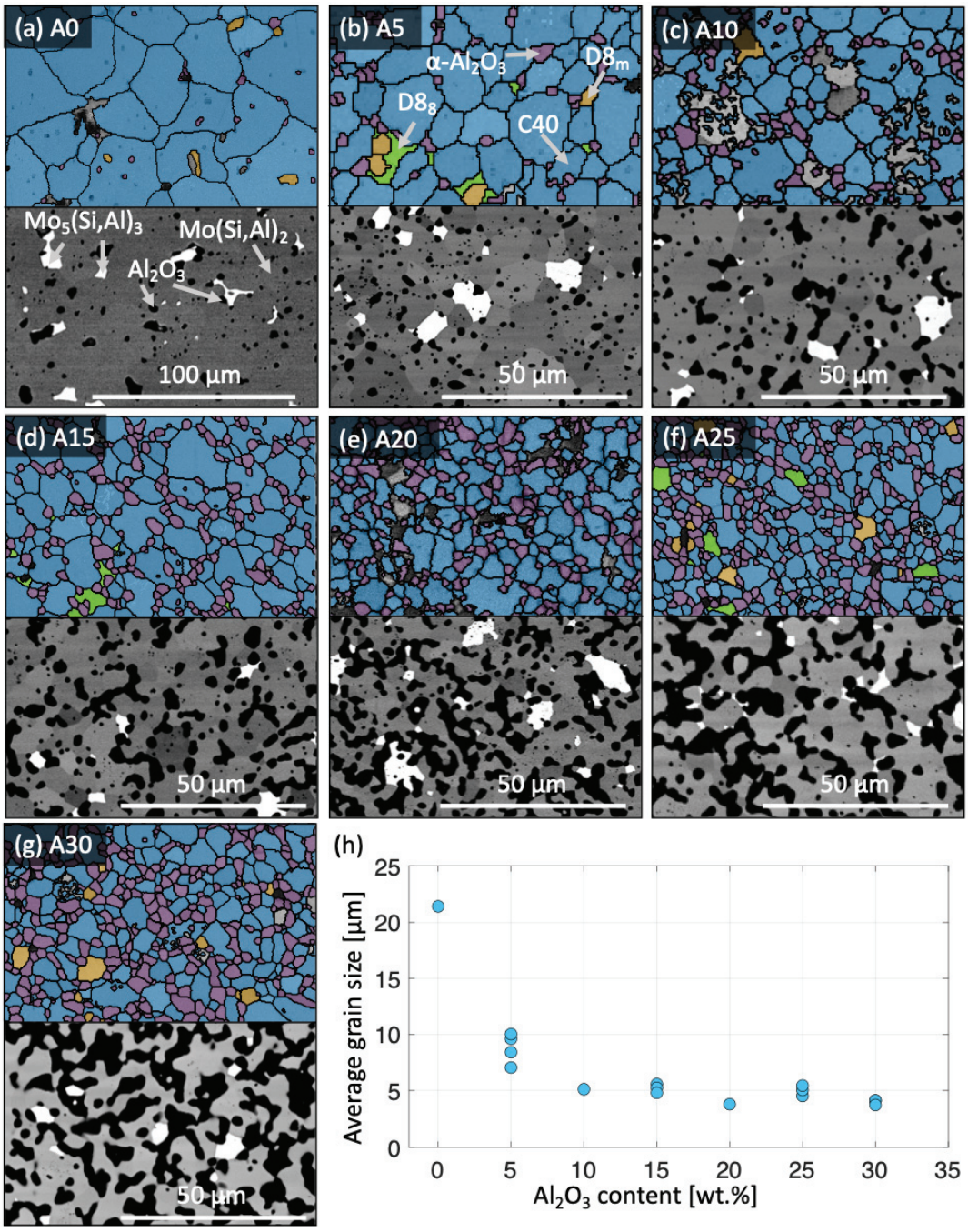

Figure 5.10: (a)-(g) EBSD maps and BSE images of A0-A30, (h) average $Mo(Si,Al)_2$ grain size as a function of added Al_2O_3.

The materials containing at least 15 wt.% Al_2O_3 exhibit a more homogeneous microstructure, with a lower scattering of data points in Figure 5.10(h).

Figure 5.11 presents histograms of the grain size distribution, confirming the trends discussed above: the Al_2O_3-lean materials, especially A0, but also A5 and A10, exhibit a broader grain size distribution than the Al_2O_3-rich mate-

rials. The histograms were created using data from Papers II and III.

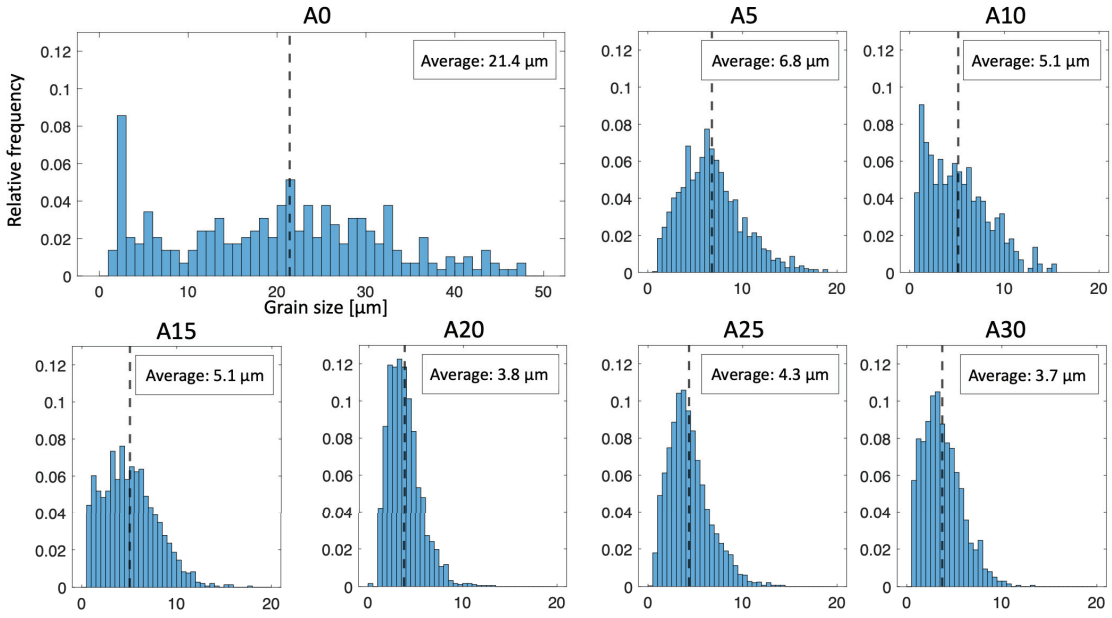

Figure 5.11: Grain size distribution of the as-sintered $Mo(Si,Al)_2$-Al_2O_3 composites.

5.2.2 Mechanical properties of $Mo(Si,Al)_2$-Al_2O_3 composites

The A5–A25 composites underwent compression testing at 1300 °C using the same setup as the Al_2O_3-free $Mo(Si,Al)_2$ material. The resulting stress-strain curves are shown in Figure 5.12. The maximum stress gradually decreases as the Al_2O_3 content increases from 0 to 15 wt.%. A slight increase is observed when the Al_2O_3 content rises from 15 to 20 wt.%, and the material containing 25 wt.% performs almost as well as the Al_2O_3-free material.

A similar trend was observed when A5, A15, A25 and A30 were tested in four-point bending at 1300 °C. The stress required to plastically deform A15 was lower than that required for the other materials. The stress-displacement curves from the four-point bending tests are shown in Figure 5.13. Also included in this figure are lines indicating the offset yield corresponding to a permanent displacement of the loading rolls of 0.04 and 0.4 mm.

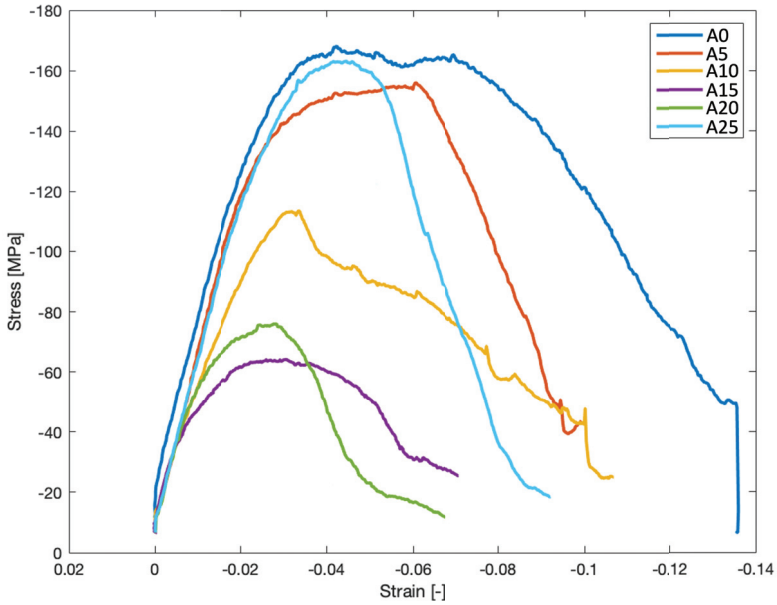

Figure 5.12: Stress-strain curves of A0–A25 tested in compression at 1300 °C.

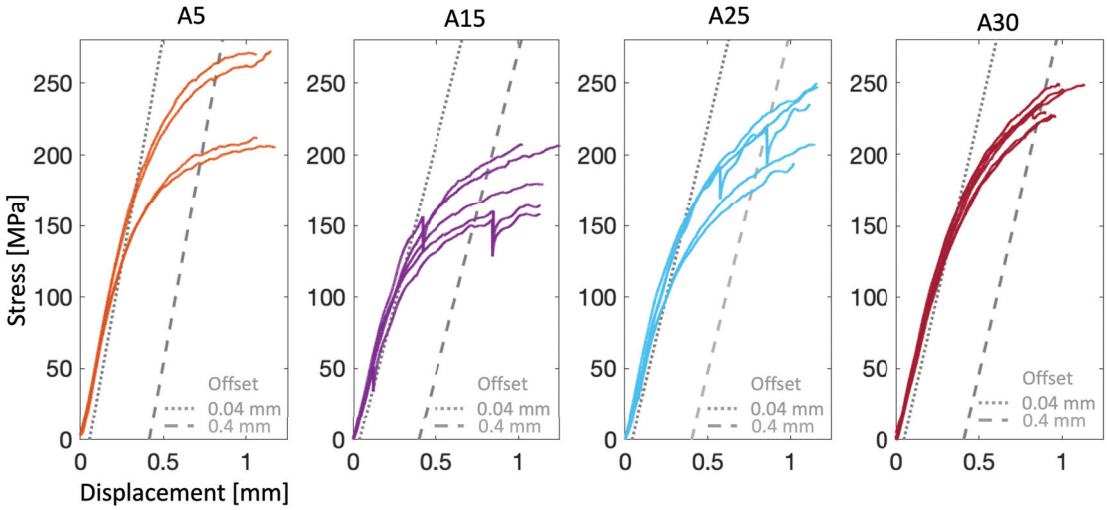

Figure 5.13: Stress-displacement curves from flexural testing at 1300 °C of $Mo(Si,Al)_2$-Al_2O_3 composites.

By combining the results from the two types of tests, the graph shown in Figure 5.14 was created. The figure clearly illustrates that the effect of Al_2O_3 on strength depends on the amount of added particles: at low additions (up to 15 wt.%), the strength decreases, while at higher additions (up to 30 wt.%), the strength increases. The four-point bending results also show that the effect is more pronounced at higher deformation levels, indicating that the particles not only affect the yield stress, but also the work hardening behaviour.

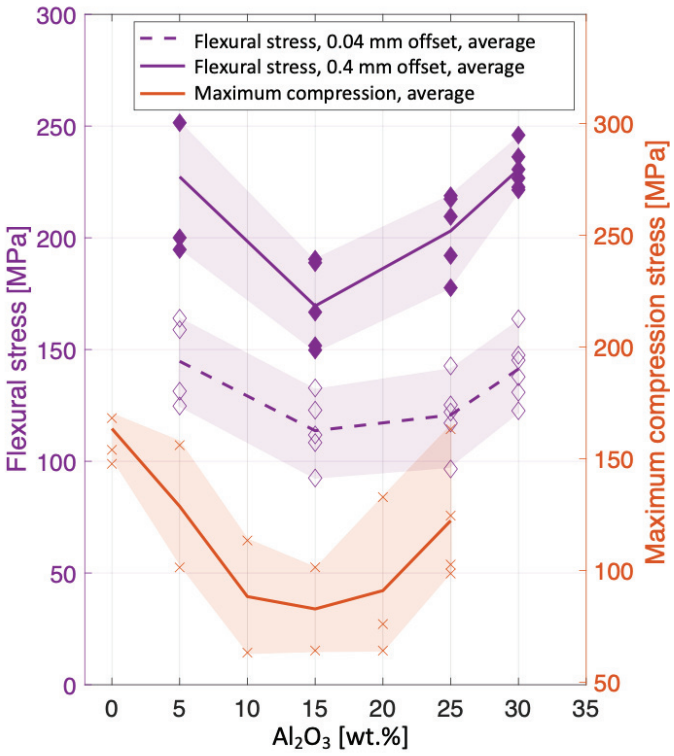

Figure 5.14: Maximum stress from compression testing, and flexural stress at 0.4 and 0.04 mm displacement from four-point bending testing of $Mo(Si,Al)_2$-Al_2O_3 composites.

The decrease in stress observed from A0 to A15 is attributed to the reduction in grain size. As the grain size decreases, the total area of grain boundaries increases, which makes the material more susceptible to grain boundary sliding. This mechanism was suggested to be the primary deformation mechanism in $Mo(Si,Al)_2$ in Section 5.1.5.

In contrast to A0, EBSD investigations of the composites revealed no evidence of dislocation-induced deformation mechanisms, such as high GOS or GROD values, formation of LAGBs, or onset of DRX. This could partly be because the composites were tested to slightly lower strains. However, this could also indicate a transition from a deformation behaviour involving both the glide of dislocations and grain boundary sliding, to being dominated by grain boundary sliding. A similar behaviour has been reported for $C11_b$-structured $MoSi_2$ tested in creep [38], where coarse-grained (27 µm) $MoSi_2$ predominantly underwent deformation through dislocation creep, whereas fine-grained materials were more prone to deform through grain boundary sliding. Due to the low solubility ($MoSi_2$ being a line compound), and restricted motion of Mo and Si atoms in the lattice, it was suggested that the grain boundary sliding was accommodated by grain boundary diffusion (Coble creep) rather than lattice dif-

fusion (Nabarro-Herring creep) [38]. Diffusion at grain boundaries likely plays a crucial role in the deformation of $Mo(Si,Al)_2$ as well. However, additional research is required to thoroughly investigate the underlying mechanisms.

At high Al_2O_3 contents, when the $Mo(Si,Al)_2$ grain size has stabilised, the stress required for plastic deformation increases with further addition of Al_2O_3. The EBSD maps in Figure 5.10 show that Al_2O_3 particles are predominantly located at $Mo(Si,Al)_2$ grain boundaries. Consequently, it is plausible that these particles enhance the strength of the material by acting as obstacles, impeding grain boundary sliding.

The impact of Al_2O_3 addition is summarised by three curves in Figure 5.15. The decrease in grain size attributed to the addition of Al_2O_3 particles initially has a detrimental effect on the strength, which stabilises when the decrease in grain size saturates. The particle strengthening effect increases with the Al_2O_3 content. However, it is proposed that the slope of this curve will diminish as the grain boundaries begin to fill up with Al_2O_3. The net effect exhibits a curvature resembling those shown in Figure 5.14, with an initial negative impact on the strength that, at a critical Al_2O_3 content, becomes positive. In the research conducted for this thesis, the critical content was found to be approximately 15 wt.%.

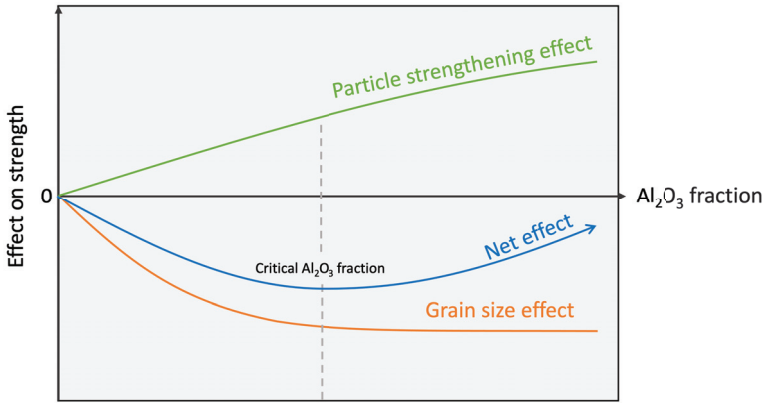

Figure 5.15: Schematic illustration of the effect of Al_2O_3 particles on the strength of $Mo(Si,Al)_2$.

In paper II, presenting the compression data on the composites, it was discussed whether the decrease in strength when increasing the Al_2O_3 content from 0 to 15 wt.% was influenced by the heating method. The specimens were heated by Joule heating, which could lead to electroplasticity, a phenomenon where materials show lower strength when a current is applied [74–77]. It was suggested that local heating of grain boundaries, leading to softening of the material, would be more pronounced in the fine-grained composites than in the coarse-grained A0 material, which could explain the decrease in stress when adding Al_2O_3. However, when the materials were tested in four-point

bending (Paper III), the same trend was observed, even though the specimens were externally heated. Therefore, it can be concluded that the results were not influenced by the heating method.

5.2.2.1 Other effects of Al_2O_3 addition

The results from the mechanical testing of the $Mo(Si,Al)_2$-Al_2O_3 composites indicated that, given a constant grain size, the strength increases with Al_2O_3 content (up to 30 wt.%). The addition of Al_2O_3 might also affect other properties of the material, for example, its oxidation behaviour. Oxidation studies on the composites have been conducted, with preliminary results indicating that the oxidation behaviour is indeed affected by the addition. However, the effect of Al_2O_3 particles on the thickness of the oxide scale and the $Mo_5(Si,Al)_3$ layer, as well as oxide spallation, seem to be temperature dependent. Further research is needed before any results can be reported.

Additionally, the electrical resistivity of the heating element is expected to increase with the Al_2O_3 content, which can be deemed advantageous from a heating perspective. However, it is important to keep in mind that a too high content of Al_2O_3 (sufficient to continuously cover the grain boundaries) could transform the heating element from a high-resistivity component to an electrical insulator.

5.3 Research question 3 - Is quaternary alloying of C40 possible, and how does it affect the strength?

Before this thesis: Alloying of C40-structured $Mo(Si,Al)_2$ has received limited attention previously. Similar to mechanical properties, research on alloying of $C11_b$-structured $MoSi_2$ has been more thoroughly explored. For example, W alloying of $MoSi_2$ has been reported successful with high solid solubility of W in $C11_b$ and improved mechanical properties [78].

In this thesis: In Paper IV, Nb, Ta, and V alloying of $Mo(Si,Al)_2$ was reported to be possible, albeit with very low solid solubility in $Mo(Si,Al)_2$. A higher solid solubility was observed in the case of W alloying (results not yet published). It was also shown that the high temperature strength was slightly improved by W alloying.

In Section 5.3.1, the microstructure of $Mo(Si,Al)_2$ alloyed with Nb, Ta, and V alloying is discussed. The effect of W alloying on the microstructure and high temperature flexural stress is discussed in Sections 5.3.2 and 5.3.3, respectively.

5.3.1 Nb, Ta, and V alloying of $Mo(Si,Al)_2$

Nb, Ta, and V alloying of $Mo(Si,Al)_2$ is interesting as the C40-structured disilicides $NbSi_2$, $TaSi_2$, and VSi_2 possess an anomalous increase in yield stress at high temperature. As this type of alloying has not been investigated in $Mo(Si,Al)_2$, the first step within this topic, before testing the mechanical properties, is to investigate if the alloying is feasible or not.

In this thesis (and in Paper IV), four alloyed materials, with the initial powder composition of $(Mo_{0.95}Nb_{0.05})(Si,Al)_2$, $(Mo_{0.9}Ta_{0.1})(Si,Al)_2$, $(Mo_{0.95}V_{0.05})(Si,Al)_2$, and $(Mo_{0.90}V_{0.10})(Si,Al)_2$, referred to as 5Nb, 10Ta, 5V, and 10V, respectively, were prepared according to Table 3.1 in Section 3. Unalloyed $Mo(Si,Al)_2$ was used as a reference.

The as-sintered materials were investigated using SXRD, EPMA/WDS and EBSD. As can be seen from the BSE images in Figure 5.16, and the SXRD diffractograms in Figure 5.17(a), the alloyed materials resemble the reference material with C40 being the matrix phase. Similar to the $Mo(Si,Al)_2$-Al_2O_3 composites, the alloyed materials also contain other phases. From the SXRD diffractograms in Figure 5.17(a) and the close up in Figure 5.17(b), $D8_m$- and $D8_8$-structured $(Mo,X)_5(Si,Al)_3$, and Al_2O_3 can be observed. Based on Rietveld refinements and BSE/SE image analysis, the materials contain around 75–85 vol.% C40, 10–15 vol.% Al_2O_3, and minor amounts of $D8_m$ and $D8_8$.

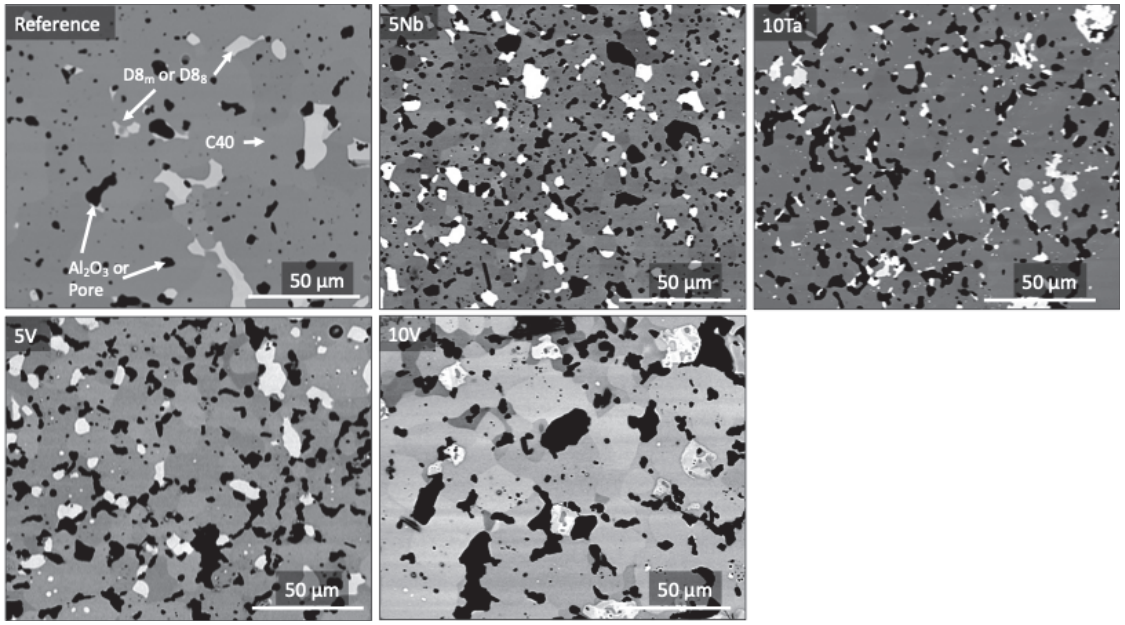

Figure 5.16: BSE images of the alloyed materials. The grey matrix phase is C40, the bright phase $D8_m$ or $D8_m$, and dark regions Al_2O_3. The C54 phase in 5V and 10V is not visible due to a similar contrast as C40.

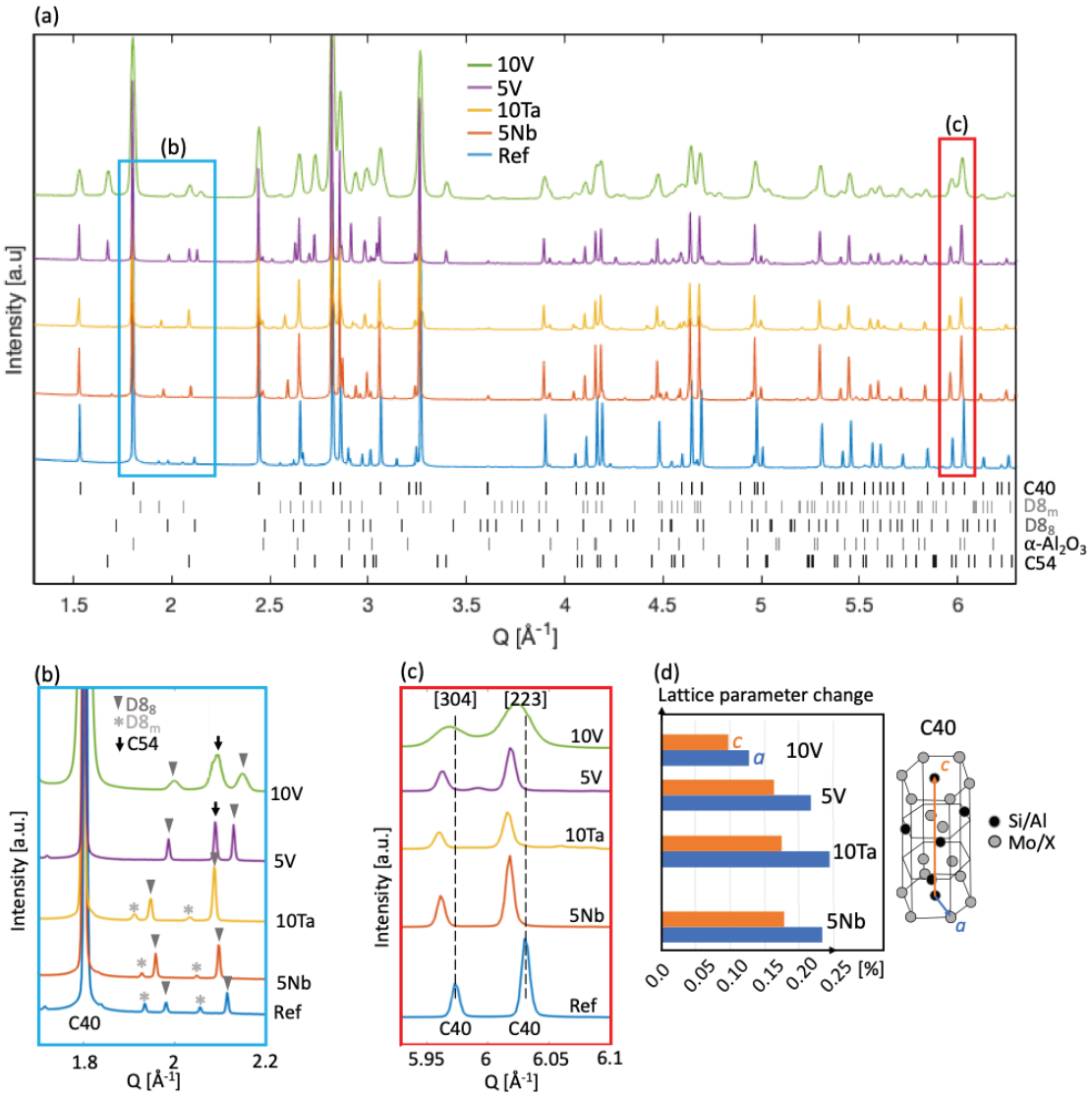

Figure 5.17: (a) SXRD diffractogram of references and Nb, Ta, and V alloyed $Mo(Si,Al)_2$. (b) Close-up of two C40 peaks, the vertical line shows the position of the peak in the reference material, (c) Change in lattice parameters, obtained from Rietveld refinements, (d) close-up showing the presence of $D8_m$, $D8_8$, and C54.

The SXRD experiments also revealed that the C40 phase was affected by alloying. This can be seen from the close-up in Figure 5.17(c), where the position of two C40 peaks in the alloyed materials has moved to lower Q relative to the reference material, indicating an increase in lattice parameters. As the alloying elements occupy the same atomic sites in the corresponding C40-structured silicides ($NbSi_2$, $TaSi_2$, and VSi_2), as Mo does in $Mo(Si,Al)_2$, it is expected that the alloying element substitutes Mo in $(Mo,X)(Si,Al)_2$. Since the atomic radius of Nb and Ta is larger than that of Mo, the increase in lattice parameters was expected for these materials, but not for V, which has a smaller radius than Mo. Rietveld refinement of the SXRD data indicated

Table 5.5: Chemical composition of C40 and C54 in (Mo,X)(Si,Al)$_2$ materials (from EPMA/WDS).

Material	**Phase**	**Chemical composition (at.%)**					
		Mo	**X**	**Si**	**Al**	**C**	**O**
Ref	C40	31	-	36	32	0.8	0.7
5Nb	C40	33	0.5Nb	33	30	2.4	0.6
10Ta	C40	32	1.5Ta	33	28	3.1	1.4
5V	C40	36	0.4V	28	34	0.7	1.2
	C54	30	0.3V	33	35	0.5	0.9
10V	C40	28	0.8V	35	31	3.2	1.3
	C54	27	1.6V	30	37	2.9	1.4

that the increase in lattice parameters was very small, below 0.25 % in all materials, see Figure 5.17(d).

EPMA/WDS analysis of the materials showed that the content of alloying element was low in C40, see Table 5.5. Also shown in Table 5.5 is that the concentration of other elements varies slightly between the materials, which also could influence the lattice parameters. The powder mixtures used for the alloyed materials were prepared to obtain materials where 5 % (5Nb and 5V) or 10 % (10Ta and 10V) of the Mo atoms were substituted by the alloying element. This corresponds to materials containing 1.65 and 3.3 at.% alloying elements in total. However, the measured concentrations of alloying elements in C40 were only 20–50 % of the intended values, see Table 5.5. Therefore, it can be concluded that the Nb, Ta, and V alloying potential of C40-structured Mo(Si,Al)$_2$ is limited. Instead, the alloying elements were enriched in the (Mo,X)$_5$(Si,Al)$_3$ phases. This is illustrated in the EPMA/WDS V map of 10V presented in Figure 5.18(b) ((Mo,X)$_5$(Si,Al)$_3$ grains are marked in the BSE image in Figure 5.18(a)). The content of alloying element in (Mo,X)$_5$(Si,Al)$_3$ was found to be up to 38 at.% depending on phase and material. However, as the concentration of V in C40 is higher in 10V than in 5V (Table 5.5), the maximum solubility has probably not been reached in this study. Increasing the initial powder portion of the alloying elements, a higher concentration could probably be achieved, if the formation of (Mo,X)$_5$(Si,Al)$_3$ could be restricted.

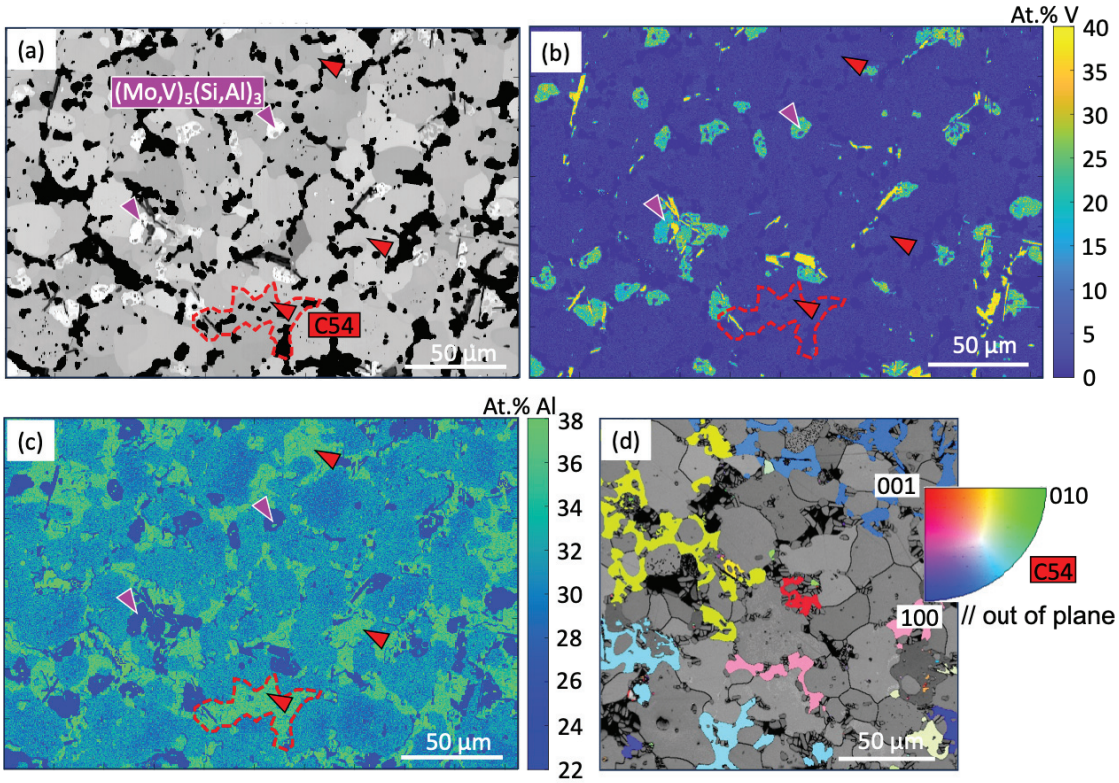

Figure 5.18: (a) BSE image of 10V, (b) EPMA/WDS V map, and (c) Al map of the same region. (d) EBSD IPF map of 10V, where the colour indicates the crystallographic axis aligned with the out-of-plane direction.

In the case of the V-alloyed materials, an additional phase, C54, was observed. Its presence can be seen in the SXRD diffractograms presented in Figure 5.17(a) and (b). However, due to a similar chemical composition as C40-structured $Mo(Si,Al)_2$, the C54 phase is hardly distinguishable in the BSE images in Figures 5.16 and 5.18(a). Nevertheless, the Al content is slightly higher in C54 compared to C40, making it visible in the EPMA/WDS Al-map shown in Figure 5.18(c). As discussed in Section 2.2, this phase has previously been reported in Al-rich $Mo(Si,Al)_2$ materials [20], and has been suggested to form via a peritectic reaction between C40, Mo_5Si_3, and liquid [79, 80]. As can be seen from the EBSD IPF map in Figure 5.18(d), the C54 grains have a network-like structure surrounding the C40 grains, which supports the anticipated formation from a melt during cooling after sintering. Since this phase was present only in the V-alloyed materials, and in a higher fraction in 10V than in 5V, its formation seems to be promoted by V. The V content in C54 is similar to that in C40, see Table 5.5 and Figure 5.18(b).

The alloying behaviour of $Mo(Si,Al)_2$ resembles that of the Mo-Si system, where the solid solubility in $C11_b$-structured $MoSi_2$ has been reported to be much lower (in the case of Nb, Ta, V, Cr, Ti, and Zr [81]) than that in $D8_m$-structured Mo_5Si_3 [82, 83]. In the case of Nb and V alloying, multiphased

microstructures have been reported, consisting of $C11_b$-structured $MoSi_2$, C40-structured $(Mo,X)Si_2$, and $D8_m$ structured $(Mo,X)_5Si_3$, with X being V or Nb [81]. Similarly, a duplex C40+$C11_b$ microstructure has been reported for Ta alloying of $MoSi_2$ [55].

In contrast to the previous alloying studies of $MoSi_2$, Al is present in the C40 phase in the present study. Therefore, it could be hypothesised that Al influences the solid solubility of Nb, Ta, and V, and potentially prevents the formation of an additional Nb-, Ta-, or V-rich C40 phase. However, further studies are needed to fully understand the alloying behaviour of $Mo(Si,Al)_2$. One suggestion is to study the materials after each step in the synthesis process. This could lead to insights into how the phases are formed. Additionally, adjusting the temperature and duration of sintering, or including additional heat treatment, may be worthwhile to ensure that equilibrium is reached.

5.3.2 W alloying of $Mo(Si,Al)_2$

W alloying of $MoSi_2$ has previously been explored with promising results: the solid solubility of W in $C11_b$-structured $(Mo,W)Si_2$ has been reported to be high, and the high temperature strength increases with W content [41, 84]. In the present study, three W-containing materials, $(Mo_{1-x},W_x)(Si,Al)_2$, with x being 0.05, 0.25, and 0.5, as well as a W-free $Mo(Si,Al)_2$ material, were prepared.

LXRD investigations revealed no significant difference between the W-alloyed materials and the reference material, as depicted in Figure 5.19. The same phases, C40, $D8_m$ and α-Al_2O_3, however, not $D8_8$, are present in all materials. Due to similar atomic radius of Mo and W, no shift in peak position can be observed in the diffractograms. The different phases can also be seen in the BSE images presented in Figure 5.20.

Using EBSD, the $(Mo,W)(Si,Al)_2$ grain size was determined to be approximately 6 µm in the W-containing materials, and slightly larger, 7.9 µm, in the reference material. Grain size histograms are shown in Figure 5.21.

The chemical composition was analysed using EDS. In contrast to Nb, Ta, and V alloying, the solid solubility of W in C40-structured $Mo(Si,Al)_2$ was shown to be high. The W content presented in Table 5.6 reaches approximately 90 % of the intended levels in the three materials. Once again, the results align with those on alloying of $C11_b$-structured $MoSi_2$, in which the solid solubility of W has been reported to be complete [41, 42].

However, as can be seen in the BSE images in Figure 5.20, particularly in the

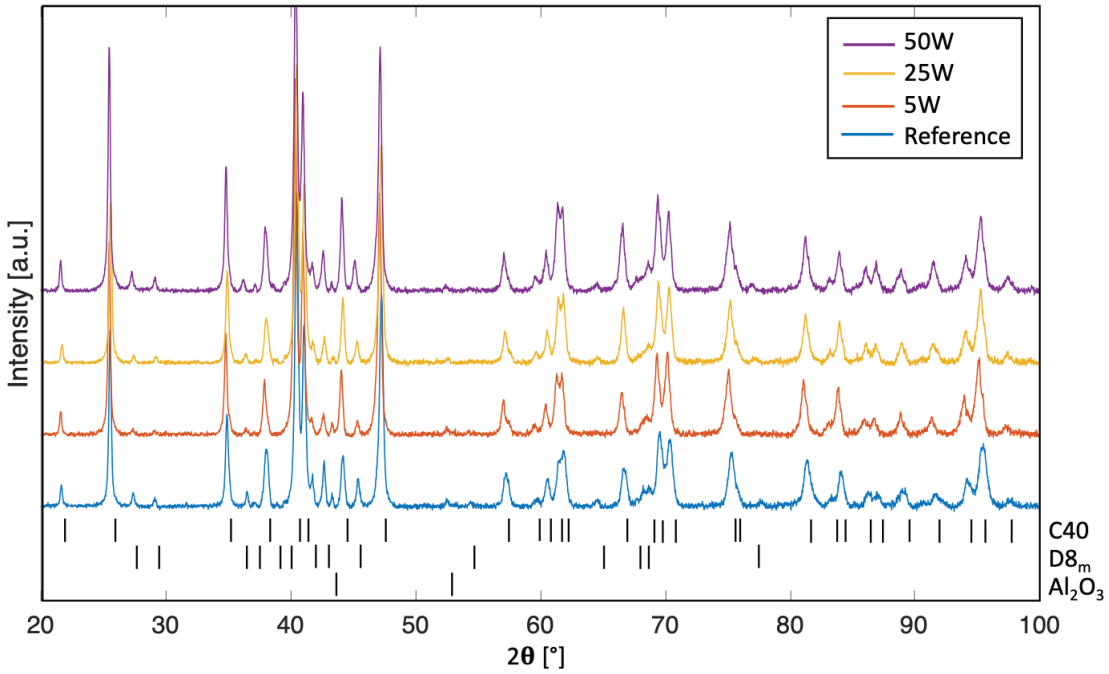

Figure 5.19: LXRD diffractograms of W-alloyed materials.

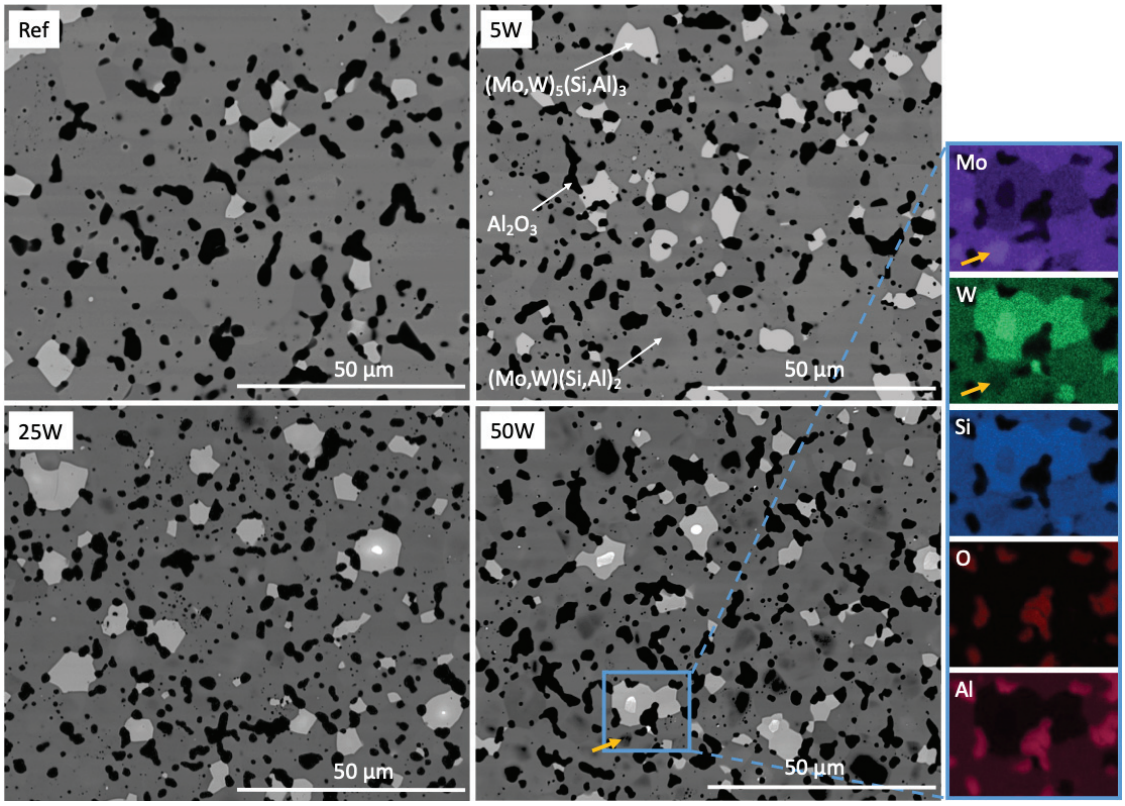

Figure 5.20: BSE images of all $(Mo,W)(Si,Al)_2$ materials, and EDS maps of 50W. The yellow arrows indicate a Mo-rich C40 grain.

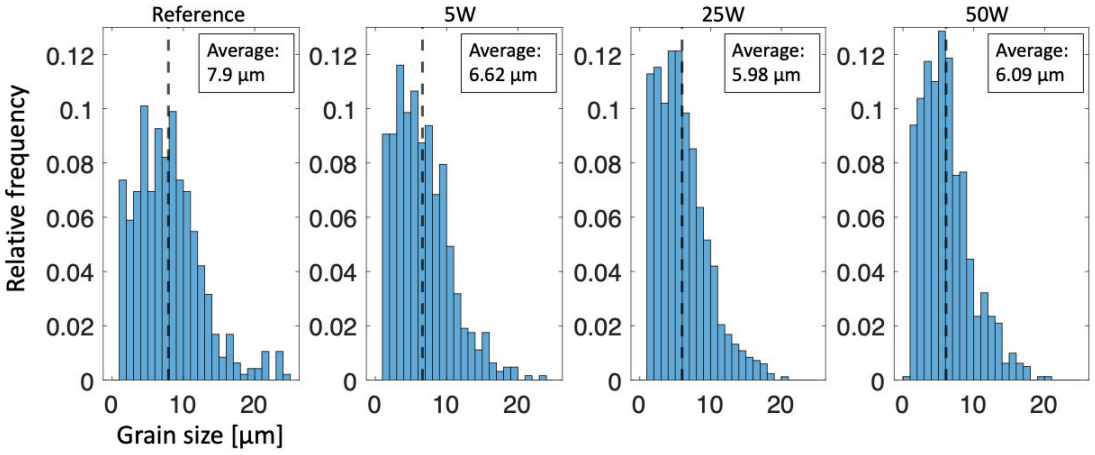

Figure 5.21: Grain size distribution of the reference and W-alloyed materials.

Table 5.6: Chemical composition of C40-structured $(Mo,W)(Si,Al)_2$ and $D8_m$-structured $(Mo,W)_5(Si,Al)_3$ phases in the W-alloyed materials.

Material	**Phase**	**Chemical composition (at.%)**				
		Mo	**W**	**Si**	**Al**	**O**
Ref	C40	33	-	34	30	4
	$D8_m$	59	-	31	6	3
5W	C40	32	2	34	30	3
	$D8_m$	54	7	30	7	4
25W	C40	26	8	33	30	3
	$D8_m$	34	27	28	7	4
50W	C40	19	15	34	29	3
	$D8_m$	19	42	29	7	4

higher alloyed materials, the C40 phase exhibits some variation in contrast, with some grains appearing darker than others. The yellow arrow in the image of the 50W material indicates such a grain. As can be seen from the EDS map on the corresponding region, this grain has a higher Mo content and a lower W content compared to the surrounding grains. The inhomogeneity is likely a result of equilibrium not being reached during sintering, probably due to slow diffusion of W in the material.

W was also shown to form solid solution with $D8_m$-structured $(Mo,W)_5(Si,Al)_3$, with a W:Mo ratio slightly higher than that of the C40-structured $(Mo,W)(Si,Al)_2$ phase. The composition of the $D8_m$ phase can be seen in Table 5.6. The results resemble those reported on W alloying of $MoSi_2$, where W tends to substitute Mo in $D8_m$ to a greater extent than in $C11_b$ [41]. Nevertheless, the present work shows that W is much more evenly

distributed between the two phases than Nb, Ta, and V are.

In 25W and 50W, several larger $D8_m$ grains contain W-rich grains, visible in bright contrast in Figure 5.20. The chemical composition of the W-rich grains varies to some extent but is approximately 90 at.% W, with small amounts of O, Al, and Mo, and little to no Si. Due to the low volume fraction of this phase, it is not visible in the LXRD diffractogram (Figure 5.19). Some grains were by EBSD indexed as bcc-structured W, which is likely correct as W was added as elemental powder during material synthesis. A longer sintering time, or an additional heat treatment, is probably needed to reach equilibrium in the material.

5.3.3 Four-point bending of $(Mo,W)(Si,Al)_2$

The mechanical properties of the $(Mo,W)(Si,Al)_2$ materials were tested using the same four-point bending equipment as used for testing the $Mo(Si,Al)_2$-Al_2O_3 composites. The resulting stress-displacement curves are shown in Figure 5.22. As can be seen from the figure, the difference in deformation response between the specimens is small. However, 25W reaches slightly higher stress values than the materials having both higher and lower W contents. Also shown in Figure 5.22 are lines indicating the offset yield corresponding to the displacements of 0.04 and 0.4 mm of the loading points.

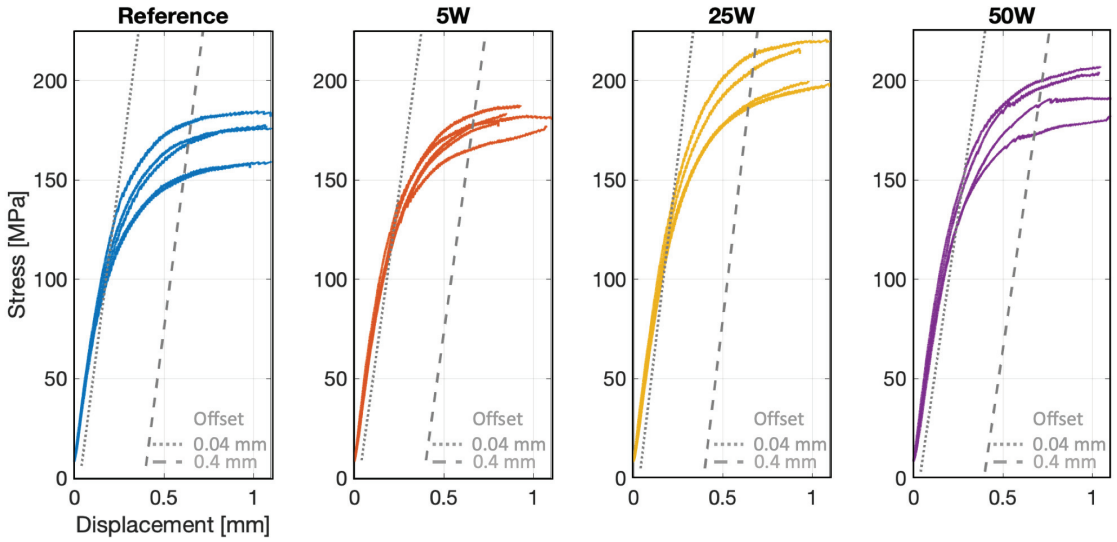

Figure 5.22: Stress-displacement curves from four-point bending of $(Mo,W)(Si,Al)_2$ materials.

The flexural stress values corresponding to the offset yield of 0.4 and 0.04 mm are shown in Figure 5.23. Similar to the $Mo(Si,Al)_2$-Al_2O_3 composites, the effect of W alloying is more pronounced at the higher deformation level,

suggesting that the influence of W alloying primarily affects the plastic deformation rather than the elastic deformation.

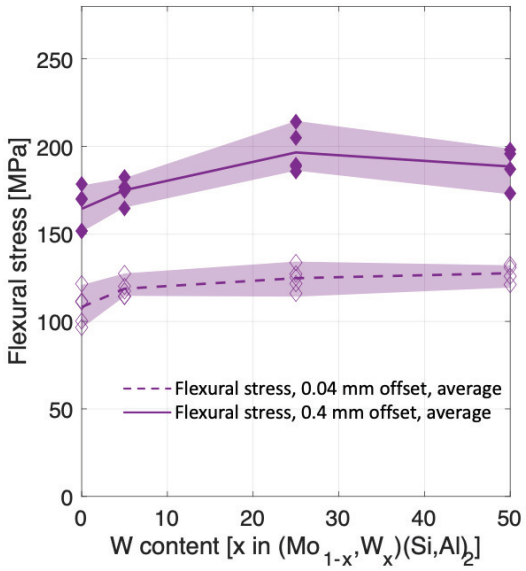

Figure 5.23: Flexural stress at 0.04 and 0.4 mm displacement from four-point bending of $(Mo,W)(Si,Al)_2$ materials.

5.4 Research question 4 - How does alloying with yttrium affect the high temperature oxidation behaviour of $Mo(Si,Al)_2$?

Before this thesis: The high temperature oxidation behaviour of $Mo(Si,Al)_2$ has been well-studied and is widely regarded as excellent. Nevertheless, spallation of the oxide may occur, particularly on heating elements with large diameters.

In this thesis: To address the oxide spallation, an oxidation study of Y-alloyed materials was conducted and presented in Paper IV. Y alloying has previously been shown to improve oxide adhesion on other Al_2O_3 forming materials. However, in this thesis, it was shown that the addition did not improve the oxidation properties of $Mo(Si,Al)_2$.

5.4.1 Microstructure before oxidation

Four materials containing 0.1, 0.5, 1 and 2 at.% Y, referred to as 0.1Y, 0.5Y, 1Y and 2Y, respectively, were synthesised according to Table 3.1. A Y-free

$Mo(Si,Al)_2$ material was synthesised similarly. The materials were studied using LXRD, SEM imaging and EDS. A BSE image of the 2Y material is shown in Figure 5.24(a) and diffractograms of all materials are presented in Figure 5.24(b). The figures reveal the presence of C40-structured $Mo(Si,Al)_2$, $D8_m$-structured $Mo_5(Si,Al)_3$, and α-Al_2O_3 in all materials. An additional phase, Yttrium Aluminium Garnet (YAG, $Y_3Al_5O_{12}$), is present in the Y-alloyed materials.

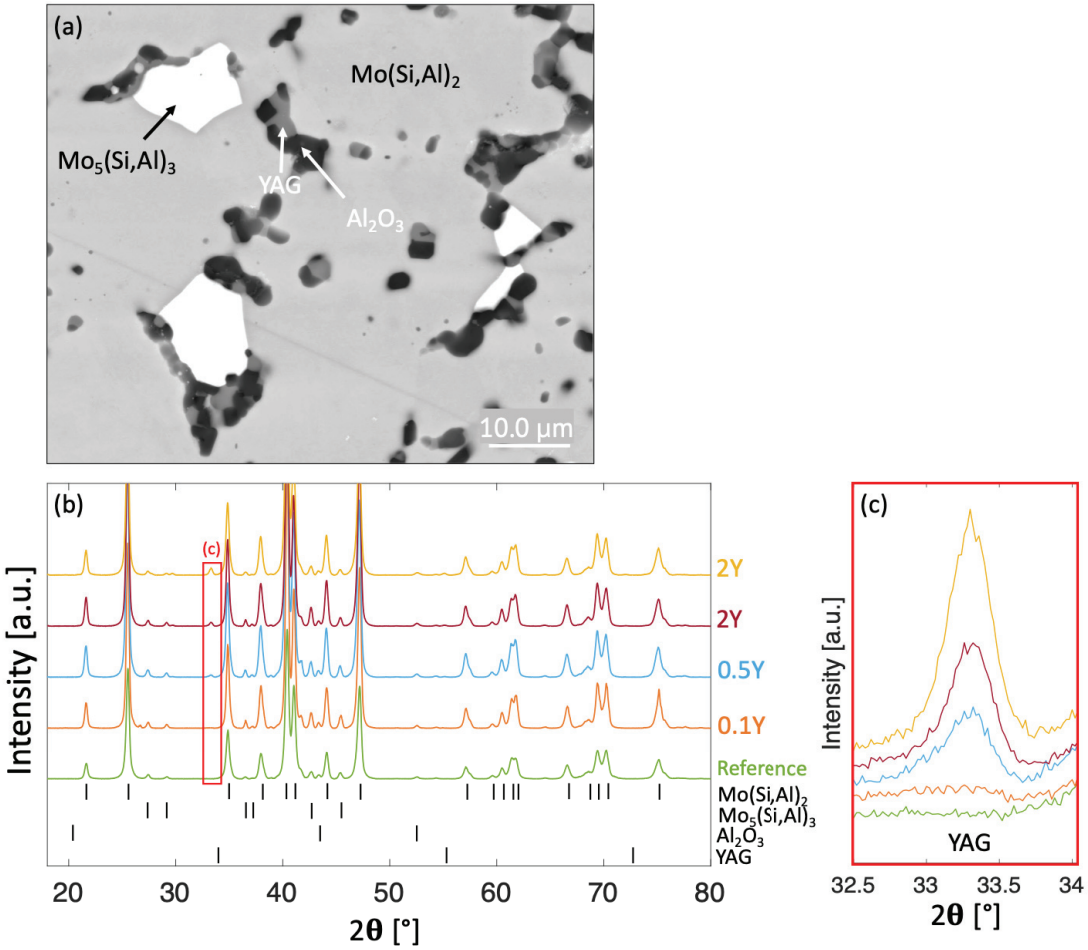

Figure 5.24: (a) BSE of the 2Y material, (b) LXRD diffractograms of the Y-alloyed $Mo(Si,Al)_2$ materials, (c) close up showing a YAG peak.

As indicated by the close-up in Figure 5.24(c), the volume fraction of YAG increases with the Y content. This observation was confirmed through BSE/SE image analysis, see Table 5.7. The volume fractions of the other phases were similar in all materials (approximately 79 vol.% $Mo(Si,Al)_2$, 7 vol.% $Mo_5(Si,Al)_3$, and 14 vol.% Al_2O_3).

Table 5.7: Volume fraction of YAG phase in the Y-alloyed materials.

Material	**Reference**	**0.1Y**	**0.5Y**	**1Y**	**2Y**
Vol.% YAG	-	0.1	0.5	1.4	2.6

The chemical composition was investigated using EDS. It was shown that Y was exclusively present in the YAG phase. This observation indicates that Y alloying of $Mo(Si,Al)_2$ is not feasible using the synthesis route employed in this work. Instead of forming a solid solution with $Mo(Si,Al)_2$, Y oxidises to YAG. The composition of the YAG particles varied, some were close to stoichiometric (15 at.% Y, 25 at.% Al, and 60 at.% O), while others were contaminated with small amounts of Mo and Si. The average composition of all phases can be seen in Table 5.8. The presence of Mo and Si in the YAG particles provides clues on their formation. It is suggested that Y is initially present in a mixed Mo-Si-Al-Y phase which then spontaneously oxidises by Al_2O_3, resulting in the formation of YAG. This hypothesis is supported by the BSE image in Figure 5.24(a), which shows that the YAG grains tend to be in contact with Al_2O_3.

Table 5.8: Chemical composition of the phases in the Y-alloyed materials.

Phase	**Chemical composition (at.%)**				
	Mo	**Si**	**Al**	**O**	**Y**
$Mo(Si,Al)_2$	32	35	29	3	-
$Mo_5(Si,Al)_3$	59	34	6	2	-
YAG	4	3	25	57	12

5.4.2 Oxidation at 1500 °C

The specimens were oxidised in air at 1500 °C for up to 250 hours as described in Section 4.2. The specimens were weighed after 24, 50, 100, and 250 hours of exposure, and SEM analysis was performed after 24, 50, and 250 hours.

5.4.2.1 Mass gain study

The mass gain curve of the Y-free $Mo(Si,Al)_2$ material, shown in Figure 5.25(a), exhibits a parabolic shape resembling the behaviour observed in oxidation studies of the $Mo(Si,Al)_2$ material Kanthal Super ER [60], suggesting the formation of a protective oxide scale. The mass of spalled oxide, collected in alumina crucibles, was minimal for the reference material, see Figure 5.25(b).

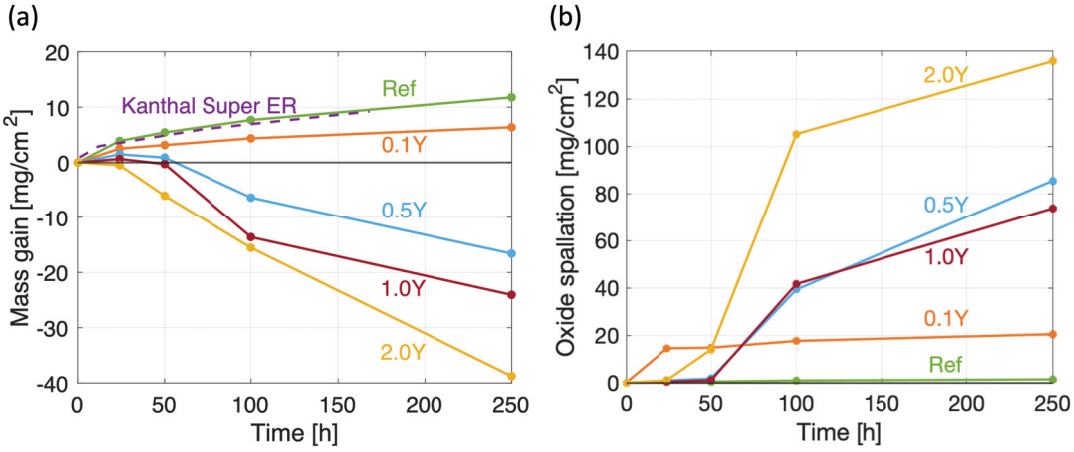

Figure 5.25: (a) The mass gain of Y-alloyed $Mo(Si,Al)_2$ materials oxidised in air at 1500 °C, and Kanthal Super ER oxidised in dry air at 1500 °C [60]. (b) The mass of spalled oxide from the Y-alloyed materials.

Figure 5.25(a) shows that the oxidation behaviour of $Mo(Si,Al)_2$ is severely affected by Y alloying, resulting in substantial mass losses for 0.5Y, 1Y, and 2Y. The mass loss can partly be explained by high spallation (Figure 5.25(b)). However, the mass loss in Figure 5.25(a) exceeds the mass of the collected spalled oxide, indicating either evaporation of oxide (MoO_3) or incomplete collection of all spalled oxide.

5.4.2.2 Oxide and material microstructure

Despite the mass loss of the Y-alloyed materials, SEM investigations of the specimens showed that the thickness of the oxide scale increases with the Y content. The oxide thickness as a function of oxidation time is shown in Figure 5.26(a).

Additionally, it was shown that the composition of the scales in the alloyed materials differed from that of the reference material. While the oxide on the reference material primarily consisted of Al_2O_3 with minor amounts of mullite, as shown in Figure 5.26(b), the Y-alloyed materials exhibited a much higher content of mullite in the outer part of the oxide, as can be seen in Figure 5.26(c). An additional oxide, yttrium silicate (YS), was present in the oxides on the alloyed materials. The dendritic structure of YS, depicted in Figure 5.27, indicates that it has crystalised from a melt during cooling after exposure.

Due to the preferential oxidation of Al in $Mo(Si,Al)_2$ [53], a $Mo_5(Si,Al)_3$ layer was formed underneath the oxide scale on all materials. The Al content in this

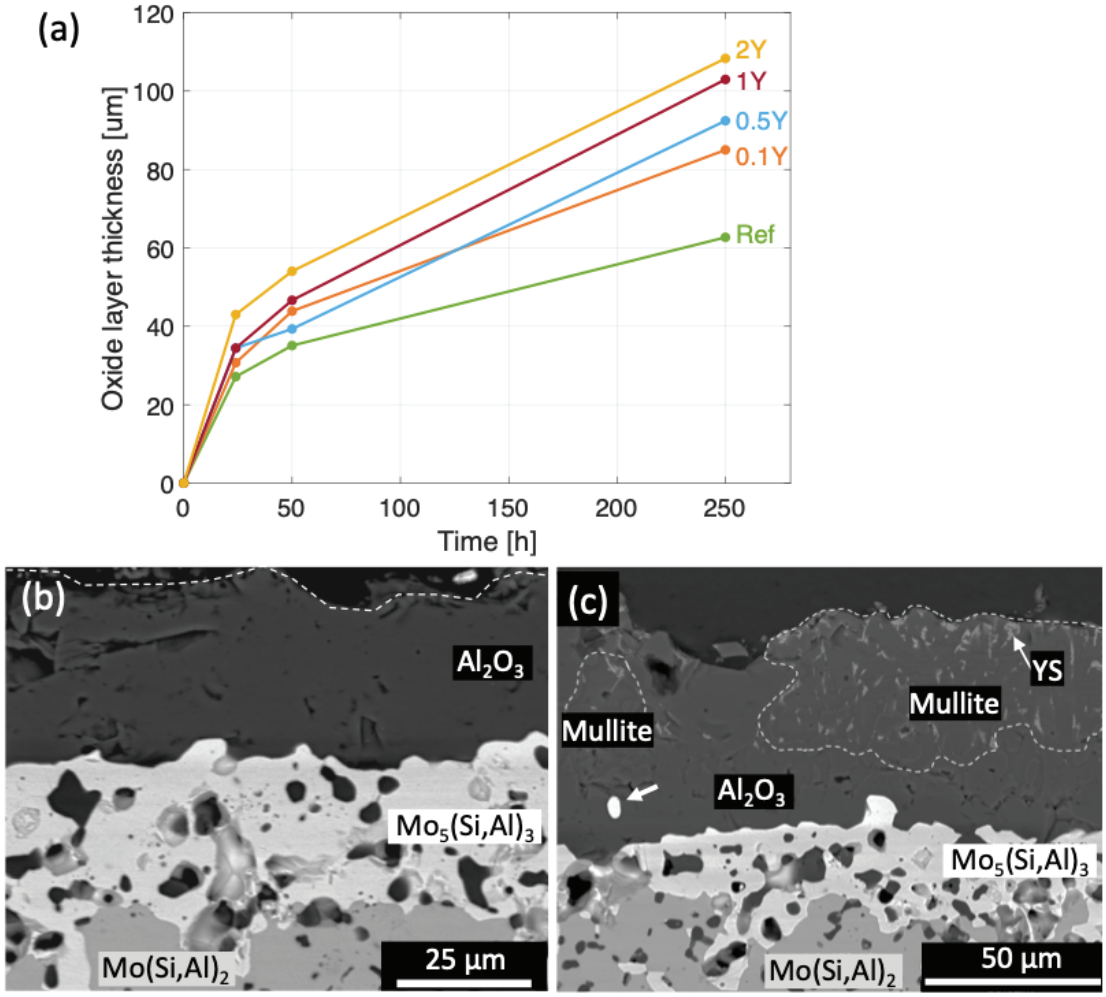

Figure 5.26: (a) Oxide thickness as a function of exposure time, (b) BSE image of the reference material, (c) BSE image of 2Y oxidised for 50 h at 1500 °C. A detached $Mo_5(Si,Al)_3$ grain is indicated by the arrow.

layer was much lower than that in the $Mo_5(Si,Al)_3$ grains in the bulk material (approximately 3 and 5.9 at.% Al, respectively). In the unalloyed material, the thickness of this layer was approximately the same as the oxide scale thickness, consistent with previous research [53, 59, 60]. In the Y-containing materials, the thickness was much thinner than the corresponding oxide scale.

The $Mo_5(Si,Al)_3$ layer has been previously identified as the source of Si, present as mullite, in the oxide scale [53, 59, 60]. During oxidation, particles may detach from the $Mo_5(Si,Al)_3$ layer and incorporate into the oxide scale. Over time, these particles oxidise to form SiO_2, which then react with Al_2O_3 to form mullite. Mo oxidises to MoO_3, which evaporates due to its high vapour pressure at elevated temperatures [53, 59, 60]. Detached and partly oxidised $Mo_5(Si,Al)_3$ particles were found in both the Y-free material and the alloyed materials (see Figure 5.26(c)). However, as the number (or the size) of such

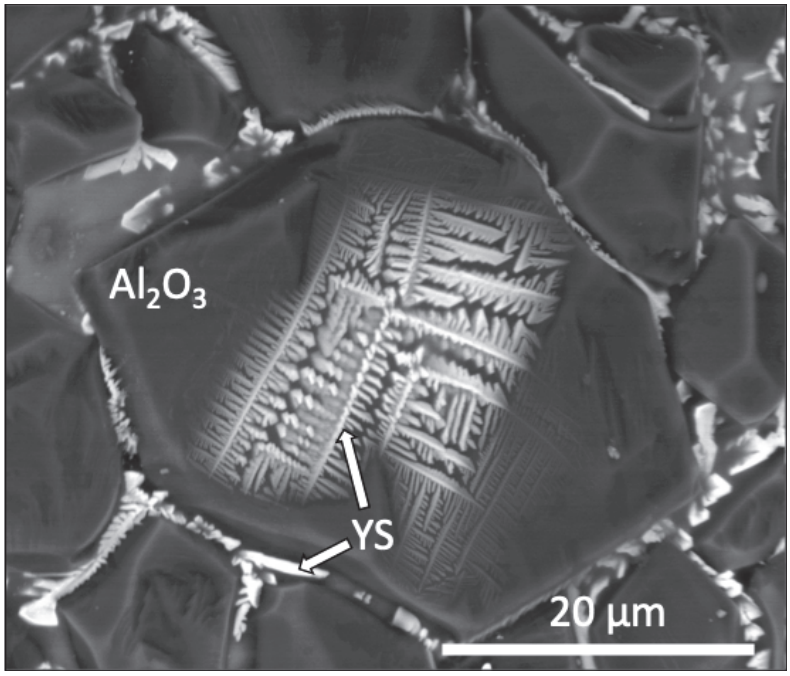

Figure 5.27: BSE image of oxide surface showing the dendritic structure of YS on Al_2O_3 grains.

particles was not higher in the Y-alloyed materials than in the reference, it is unlikely that the thinner $Mo_5(Si,Al)_3$ layer and the higher mullite content are solely due to these detached particles. Instead, it is argued that Y affects the preferential oxidation of $Mo(Si,Al)_2$, leading to an increased oxidation rate of Si and Mo. As a consequence, the $Mo_5(Si,Al)_3$ will be thinner than in the unalloyed material.

As mentioned, it is suggested that a melt forms in the outer part of the oxide scale of the Y-alloyed materials during oxidation at 1500 °C. Since oxygen can easily be transported within the melt, the oxides formed on the Y-alloyed materials are less protective than the Al_2O_3 scale on the reference material. Therefore, it is proposed that the melt is the major factor contributing to the increased oxidation rate and the thicker oxides. The thicker oxides are also likely responsible for the pronounced spallation of the Y-alloyed materials. Due to different coefficients of thermal expansion (CTE) between the oxide scale and the bulk material, stresses are introduced in the oxide during heating and cooling. Additionally, the multi-phase oxide introduces variations in CTE within the scale, further contributing to increased spallation.

CHAPTER 6

Conclusions and future research

The aim of this thesis is to answer the research questions presented in the first chapter. The most important conclusions are summarised in the first section of this chapter. In the second section, suggestions for future work on $Mo(Si,Al)_2$ are presented.

6.1 Conclusions

1. **How does polycrystalline C40-structured $Mo(Si,Al)_2$ deform at high temperature?**

   - $Mo(Si,Al)_2$ deforms plastically when tested in both compression and four-point bending at 1300 °C. A pronounced softening is observed at high strain.
   - The primary deformation mechanism in $Mo(Si,Al)_2$-based materials is grain boundary sliding, and the strength of the material is grain-size sensitive.
   - In coarse-grained $Mo(Si,Al)_2$, deformation is inhomogeneous on both the intragranular and intergranular scales. In addition to grain boundary sliding, dislocation-induced deformation is active. Grains with high Schmid factor generally show high deformation levels,

with deformation patterns aligned with specific crystallographic directions.

- In coarse-grained $Mo(Si,Al)_2$, DRX and the formation of LAGB contribute to softening.

2. **Can the high temperature strength be improved through particle strengthening by adding Al_2O_3?**

   - The effect on strength depends on the amount of added Al_2O_3. At low Al_2O_3 contents, up to 10–15 wt.%, the strength decreases due to grain refinement. At higher contents, the decrease in grain size saturates, and the strength increases due to grain boundary strengthening.

3. **Is quaternary alloying of C40 possible, and how does it affect the strength?**

   - The solid solubility of Nb, Ta, and V is limited in C40-structured $Mo(Si,Al)_2$. Instead, the alloying elements are enriched in $D8_m$- and $D8_8$-structured $Mo_5(Si,Al)_3$.
   - V alloying promotes the formation of C54-structured $Mo(Si,Al)_2$.
   - W has high solid solubility in both $Mo(Si,Al)_2$ and $Mo_5(Si,Al)_3$.
   - The high temperature flexural stress is slightly improved by W-alloying.

4. **How does the alloying with yttrium affect the high temperature oxidation behaviour of $Mo(Si,Al)_2$?**

   - Y alloying of $Mo(Si,Al)_2$ does not improve high temperature oxidation resistance. Contrarily, both the oxidation rate and the tendency of oxide spallation increase with the Y content.

6.2 Suggestions for future research

In this thesis, several questions regarding the deformation behaviour and the feasibility of alloying $Mo(Si,Al)_2$ have been addressed. However, the list of unresolved questions continues to grow as more details on the topic are unfolded. In this section, potential directions for future research, of interest from both scientific and commercial perspectives, are outlined.

From a scientific standpoint, a thorough investigation into the deformation behaviour is of particular interest. As discussed in this thesis, there is a proposed activation of slip systems other than the traditional $(0001)\langle 1\bar{2}10\rangle$ system. To study this further, dedicated TEM-studies on highly deformed grains, preferably those with a low Schmid factor, are needed. STEM could be employed

to investigate the influence of the nano-sized intragranular Al_2O_3 particles on the strength of the material. As shown in Section 5.1.4.1, the observation of dislocation traces in the vicinity of such particles suggests a potential impact on deformation behaviour.

As presented in the discussion connected to Research questions 1 and 2, the deformation behaviour of $Mo(Si,Al)_2$ is grain size sensitive with a creep-like behaviour, and grain boundary sliding was proposed as the primary deformation mechanism. It was suggested, albeit not confirmed, that the grain boundary sliding is accommodated by grain boundary diffusion. Therefore, a suggestion for future research is to further investigate grain boundary sliding and its associated mechanisms. This could be achieved by subjecting materials with different grain sizes to creep testing under different loads.

Regarding the quaternary alloying of $Mo(Si,Al)_2$, the preliminary results on W alloying indicated a slight increase in high temperature strength for the $(Mo_{0.75}W_{0.25})(Si,Al)_2$ material. In addition to further analysis of the results from the four-point bending experiments, it could also be interesting to combine the results of this study with that of the Al_2O_3 and grain size project. A suggestion is to prepare a coarse-grained $(Mo_{0.75}W_{0.25})(Si,Al)_2$ material and test it in compression similar to the A0 material. Furthermore, it would be worthwhile to investigate whether the strength could be further enhanced by incorporating higher concentrations of Al_2O_3 particles into the W-containing material.

Conducting mechanical testing at different temperatures is crucial for both scientific understanding and practical applications. This holds particular significance as the service temperature for current $Mo(Si,Al)_2$ heating elements reaches up to 1580 °C. This temperature approaches the sintering temperature (1600 °C), at which the material with the highest strength in this work, the Al_2O_3-free $Mo(Si,Al)_2$, undergoes grain growth. The possible occurrence of grain growth during creep testing is expected to impact the mechanical response.

Beyond mechanical properties, other characteristics of the modified $Mo(Si,Al)_2$ materials must be investigated before assessing their potential as heating elements. As mentioned in Section 5.2.2.1, the addition of Al_2O_3 may influence both the oxidation behaviour and electrical resistivity. Since heating elements depend on the formation of a protective oxide scale and high resistivity, the effects on these properties need to be investigated.

The long-term goal of the work conducted in this project is to enhance the properties of $Mo(Si,Al)_2$-based materials used in resistive heating elements. As the materials investigated in this thesis were prepared in the laboratory, the synthesis route differs from that used in commercial production. Consequently,

upscaling and modifications of the synthesis steps outlined in this thesis are needed before producing commercial heating elements with similar properties.

Acknowledgements

I would like to express my sincere appreciation to all those who have supported me during my journey as a PhD student at Kanthal and Chalmers.

My deepest gratitude goes to my main supervisor Docent Magnus Hörnqvist Colliander for his outstanding support, guidance, and patience throughout this project. His exceptional ability to explain both complicated dislocation concepts and basic mechanical properties in a clear and accessible manner has been invaluable to me.

I am equally grateful to my co-supervisor Dr. Erik Ström at Kanthal. He is a true expert on $Mo(Si,Al)_2$-based materials. The way he addresses all of my challenging (and sometimes seemingly trivial) questions regarding the material and its synthesis process is impressive.

I would like to thank all of my colleagues at the R&D Department at Kanthal and the Division of Microstructure Physics at Chalmers. A special thanks to both current and previous members of 'Magnus' Group': Dr. Olof Bäcke, Dr. Kristine Bakken, Yao Hu, Dr. Emil Eriksson, Dr. Ren Qiu, and Dr. Anand H.S. Iyer, for their invaluable assistance with laboratory work and advanced synchrotron experiments. We have also had a lot of fun together, for example, exploring the cuisines in Hamburg (a lot of meat) and San Diego (tacos, tacos, and tacos).

I am grateful to Jörgen Sahlström, Niklas Andersson, and Toni Syrjälä for their assistance with materials synthesis at Kanthal. Additionally, thanks to Dr.

Anand Rajagopal at Alleima for his support with EPMA/WDS investigations, to Prof. Farid Akthar and Lars Frisk at Luleå University of Technology for their collaboration on compression tests, and to Ola Löfgren for his invaluable assistance with computer-related issues. I also want to express my gratitude to my former colleagues at the Division of Environmental Inorganic Chemistry at Chalmers for their support and collaboration.

Finally, I would like to thank my family for always supporting me. A special thanks to Henrik, for always being there for me, and supporting me with love, laughter and unforgettable adventures.

Bibliography

[1] The Paris Agreement - What is the Paris Agreement? https://unfccc.int/process-and-meetings/the-paris-agreement/the-paris-agreement. Accessed: 2021-11-13.

[2] Hannah Ritchie, Pablo Rosado, and Max Roser. Emissions by sector: where do greenhouse gases come from? *Our World in Data*, 2020. https://ourworldindata.org/emissions-by-sector.

[3] S. Madeddu, F. Ueckerdt, M. Pehl, J. Peterseim, M. Lord, Karthik A. Kumar, C. Krüger, and G. Luderer. The CO_2 reduction potential for the European industry via direct electrification of heat supply (power-to-heat). *Environmental Research Letters*, 15(12), 2020. doi: 10.1088/1748-9326/abbd02.

[4] Kanthal. Kanthal Super heating elements. https://www.kanthal.com/en/products/furnace-products/electric-heating-elements/molybdenum-disilicide-heating-elements/.

[5] Kanthal. Metallic heating elements. https://www.kanthal.com/en/products/furnace-products-and-heating-systems/electric-heating-elements/metallic-heating-elements/.

[6] Kanthal. Kanthal Super ER. https://www.kanthal.com/en/products/furnace-products/electric-heating-elements/molybdenum-disilicide-heating-elements/element-grades/kanthal-super-er/, 2021.

[7] Sandvik Group. Sandvik Materials Technology. Resistance heating alloys for electric home appliances. www.kanthal.com/Global/Downloads/-Materialsinwireandstripform/Resistanceheatingwireandstrip/S-KA026-B-ENG-2012-01.pdf. Accessed: 2021-11-13.

[8] R. W. Davidge. *Mechanical behaviour of ceramics.* Cambridge solid state science series. Cambridge U.P., 1979.

[9] R. Pampuch. *An Introduction to Ceramics*. Lecture Notes in Chemistry: 86. Springer International Publishing, 2014. doi:10.1007/978-3-319-10410-2.

[10] Z. Yao, J. Stiglich, and T. S. Sudarshan. Molybdenum silicide based materials and their properties. *Journal of Materials Engineering and Performance*, 8(3):291–304, 1999. doi: 10.1361/105994999770346837.

[11] R. Mitra. Silicides and Silicide Matrix Composites for High-Temperature Structural Applications. In Y. Mahajan and Johnson R., editors, *Handbook of Advanced Ceramics and Composites*, pages 1–55. Springer Nature Switzerland AG, 2019. doi: 10.1007/978-3-319-73255-8_40-1.

[12] T. Tabaru, K. Shobu, M. Sakamoto, and S. Hanada. Effects of substitution of Al for Si on the lattice variations and thermal expansion of $Mo(Si,Al)_2$. *Intermetallics*, 12(1):33–41, jan 2004. doi: 10.1016/J.INTERMET.2003.07.002.

[13] K. Shobu, T. Watanabe, E. Tani, and M. Akiyama. Ceramic composite material with high heat-resistant property, U.S. Patent 5585313 December 17, 1996.

[14] K. Tanaka, K. Nawata, H. Inui, M. Yamaguchi, and M. Koiwa. Refinement of crystallographic parameters in transition metal disilicides with the $C11_b$, C40 and C54 structures. *Intermetallics*, 9:603–607, 2001.

[15] Y. Du and J. C. Schuster. Experimental reinvestigation of the CrSi-Si partial system and update of the thermodynamic description of the entire Cr-Si system. *Journal of Phase Equilibria*, 21(3):281–286, 2000.

[16] Y. Umakoshi, T. Nakano, K. Kishimoto, D. Furuta, K. Hagihara, and M. Azuma. Strength and deformation mechanism of C40-based single crystal and polycrystalline silicides. *Materials Science and Engineering A*, 261(1-2):113–121, mar 1999. doi: 10.1016/s0921-5093(98)01056-9.

[17] S.V.N. Naidu, C. F. Mays, and C.R. Houska. Integrated Intensities and Lattice Parameters for Mo_5Si_3. *Journal of the American Ceramic Society*, 65(4):58–59, 1982. doi.org/10.1111/j.1151-2916.1982.tb10419.x.

[18] Y. Suzuki and K. Niihara. Syntheis and mechanical properties of $Mo_{\leq 5}Si_{\leq 3}C_{\leq 1}$ and $Mo_{\leq 5}Si_{\leq 3}C_{\leq 1}$-based composites. *Intermetallics*, 6:7–13, 1998.

[19] A. R. West. *Basic solid state chemistry*. Wiley, Chichester, 2 edition, 2010.

[20] M. Esmaeili Ghayoumabadi, A. Saidi, and M. H. Abbasi. Lattice variations and phase evolutions during combustion reactions in Mo-Si-Al system. *Journal of Alloys and Compounds*, 472(1-2):84–90, 2009.

[21] Z. Ding, J. C. Brouwer, C. Kwakernaak, M. J.M. Hermans, V Popovich, W. J. Quadakkers, and W. G. Sloof. Selective oxidation of aluminium in $Mo(Al,Si)_2$. *Corrosion Science*, 211:110884, 2023.

[22] K. Hagihara, T. Nakano, and Y. Umakoshi. Mechanical properties of C40-based ternary $Mo(Si,Al)_2$ and quaternary $(Mo,Zr)(Si,Al)_2$ silicides. *Scripta Materialia*, 38(3):471–476, 1998. doi: 10.1016/S1359-6462(97)00432-6.

[23] H. Inui, M. Moriwaki, K. Ito, and M. Yamaguchi. Plastic deformation of single crystals of $Mo(Si,Al)_2$ with the C40 structure. *Philosophical Magazine A: Physics of Condensed Matter, Structure, Defects and Mechanical Properties*, 77(2):375–394, 1998. doi: 10.1080/01418619808223759.

[24] K. Tanaka, K. Nawata, H. Inui, M. Yamaguchi, and M. Koiwa. Temperature dependence of single-crystal elastic constants of $Mo(Si,Al)_2$. *Intermetallics*, 6(7-8):607–611, 1998. doi: 10.1016/s0966-9795(98)00057-0.

[25] H. Inui and M. Yamaguchi. Deformation mechanisms of transition-metal disilicides with the hexagonal C40 structure. *Intermetallics*, 9(10-11):857–862, 2001. doi: 10.1016/S0966-9795(01)00082-6.

[26] R. Mitra, N. E. Prasad, S. Kumari, and A. V. Rao. High-temperature deformation behavior of coarse- and fine-grained $MoSi_2$ with different silica contents. *Metallurgical and Materials Transactions A: Physical Metallurgy and Materials Science*, 34 A(5):1069–1088, 2003. doi: 10.1007/s11661-003-0127-8.

[27] M. Moriwaki, K. Ito, H. Inui, and M. Yamaguchi. Plastic deformation of single crystals of $NbSi_2$ with the C40 structure. *Materials Science and Engineering A*, 239-240(1-2):69–74, 1997. doi: 10.1016/S0921-5093(97)00562-5.

[28] H. Inui, M. Moriwaki, S. Ando, and M. Yamaguchi. Plastic deformation of single crystals of $CrSi_2$ with the C40 structure. *Materials Science and*

Engineering A, 239-240(1-2):63–68, dec 1997. doi: 10.1016/s0921-5093(97)00561-3.

[29] T. Nakano, M. Azuma, and Y. Umakoshi. Tensile deformation and fracture behaviour in $NbSi_2$ and $MoSi_2$ single crystals. *Acta Materialia*, 50(14):3731–3742, 2002. doi: 10.1016/S1359-6454(02)00185-4.

[30] H. Inui, M. Moriwaki, and M. Yamaguchi. Plastic deformation of single crystals of VSi_2 and $TaSi_2$ with the C40 structure. *Intermetallics*, 6(7-8):723–728, 1998. doi: 10.1016/s0966-9795(98)00045-4.

[31] R. Mitra. Mechanical behaviour and oxidation resistance of structural silicides. *International Materials Reviews*, 51(1):13–64, 2006. doi: 10.1179/174328006X79454.

[32] K. Kishida, S. Nakatsuka, H. Nose, and H. Inui. Room-temperature deformation of single crystals of transition-metal disilicides ($TMSi_2$) with the $C11_b$ (TM=Mo) and C40 (TM=V, Cr, Nb and Ta) structures investigated by micropillar compression. *Acta Materialia*, 223:117468, 2021. doi: 10.1016/j.actamat.2021.117468.

[33] K. Ito, H. Inui, Y. Shirai, and M. Yamaguchi. Plastic deformation of $MoSi_2$ single crystals. *Philosophical Magazine A: Physics of Condensed Matter, Structure, Defects and Mechanical Properties*, 72(4):1075–1097, 1995. doi: 10.1080/01418619508239954.

[34] K. Ito, K. Matsuda, Y. Shirai, H. Inui, and M. Yamaguchi. Brittle-ductile behavior of single crystals of $MoSi_2$. *Materials Science and Engineering A*, 261(1-2):99–105, 1999. doi: 10.1016/S0921-5093(98)01054-5.

[35] R. Gibala, A. K. Ghosh, D. C. Van Aken, D. J. Srolovitz, A. Basu, H. Chang, D. P. Mason, and W. Yang. Mechanical behavior and interface design of $MoSi_2$-based alloys and composites. *Materials Science and Engineering A*, 155(1-2):147–158, 1992. doi: 10.1016/0921-5093(92)90322-R.

[36] R. M. Aikin. On the ductile-to-brittle transition temperature in $MoSi_2$. *Scripta Metallurgica et Materiala*, 26:1025–1030, 1992. doi.org/10.1016/0956-716X(92)90224-3.

[37] K. Sadananda and C. R. Feng. Effect of carbon addition on the creep of molybdenum disilicide composites. *Materials Science and Engineering A*, 192-193:862–867, 1995. doi: 10.1016/0921-5093(94)03337-4.

[38] R. Mitra, K. Sadananda, and C. R. Feng. Effect of microstructural parameters and Al alloying on creep behavior, threshold stress and activation volumes of molybdenum disilicides. *Intermetallics*, 12(7-9 SPEC. ISS.):827–836, 2004. doi: 10.1016/j.intermet.2004.02.033.

[39] K. Sadananda, C. R. Feng, R. Mitra, and S. C. Deevi. Creep and fatigue properties of high temperature silicides and their composites. *Materials Science and Engineering: A*, 261(1):223–238, 1999. doi: https://doi.org/10.1016/S0921-5093(98)01070-3.

[40] J. D. French, S. M. Wiederhor, and J. J. Petrovic. *High Temperature Silicides and Refractory Alloys, Mat. Res. Soc. Symp. Proc.*, 322:203–208, 1993.

[41] B A Gnesin, P A Gurzhiyants, and E B Borisenko. (Mo,W)$_5$ Si$_3$–(Mo,W)Si$_2$ Eutectics : Properties and Application in Composite Materials. *Inorganic Materials*, 39(7):701–709, 2003.

[42] H Inui, Takayuki Nakamoto, K. Ishikawa, and Masaharu Yamaguchi. Plastic deformation of single crystals of $(Mo_{1-X}W_X)Si_2$ with the $C11_b$ structure. *Materials Science and Engineering*, A2611:131–138, 1999.

[43] A. A. Sharif, A. Misra, J. J. Petrovic, and T. E. Mitchell. Alloying of $MoSi_2$ for improved mechanical properties. *Intermetallics*, 9(10-11):869–873, oct 2001.

[44] V. A. Gorshkov, V. I. Yukhvid, P. A. Miloserdov, N. V. Sachkova, and D. Yu Kovalev. Cast silicides of molybdenum, tungsten, and niobium by combustion synthesis. *International Journal of Self-Propagating High-Temperature Synthesis*, 20(2):100–106, 2011.

[45] P. S. Kisly and V. Yu Kodash. The mullite coatings on heaters made of molybdenum disilicide. *Ceramics International*, 15(3):189–191, 1989. doi.org/10.1016/0272-8842(89)90015-1.

[46] T. Maruyama, K. Yanagihara, and K. Nagata. High temperature oxidation of intermetallic compounds of $Mo(Si_{1-x}Al_x)_2$. *Corrosion Science*, 35(5-8):939–944, 1993. 10.1016/0010-938X(93)90312-5.

[47] D. A. Berztiss, R. R. Cerchiara, E. A. Gulbransen, F. S. Pettit, and G. H. Meier. Oxidation of $MoSi_2$ and comparison with other silicide materials. *Materials Science and Engineering: A*, 155(1-2):165–181, 1992. 10.1016/0921-5093(92)90324-T.

[48] S. K. Ramasesha, P. Srikari Tantri, and A. Bhattacharya. $MoSi_2$ and $MoSi_2$ - Based Materials as Structural Ceramics. *Metals Materials And Processes*, 12(2 3):181–190, 2000.

[49] K. Yanagihara, T. Maruyama, and K. Nagata. Effect of third elements on the pesting suppression of Mo-Si-X intermetallics (X = Al, Ta, Ti, Zr and Y). *Intermetallics*, 4(SUPPL. 1), 1996. doi: 10.1016/0966-9795(96)00019-2.

[50] A. A. Sharif. High-temperature oxidation of $MoSi_2$. *Journal of Materials Science*, 45(4):865–870, 2 2010. doi: 10.1007/s10853-009-4012-8.

[51] L. Ingemarsson, M. Halvarsson, J. Engkvist, T. Jonsson, K. Hellström, L. G. Johansson, and J. E. Svensson. Oxidation behavior of a Mo $(Si,Al)_2$-based composite at 300–1000 °C. *Intermetallics*, 2010. doi: 10.1016/j.intermet.2009.10.019.

[52] L. Ingemarsson. *Oxidation of $MoSi_2$ based materials*. PhD thesis, Chalmers University of Technology, Göteborg, Sweden, 2010.

[53] L. Ingemarsson, K. Hellström, S. Canovic, T. Jonsson, M. Halvarsson, L. G. Johansson, and J. E. Svensson. Oxidation behavior of a $Mo(Si,Al)_2$ composite at 900–1600 °C in dry air. *Journal of Materials Science*, 48(4):1511–1523, 2 2013. doi: 10.1007/s10853-012-6906-0.

[54] M. Sundberg, G. Malmqvist, A. Magnusson, and T. El-Raghy. Alumina forming high temperature silicides and carbides. In *Ceramics International*, volume 30, pages 1899–1904, 2004. doi: 10.1016/j.ceramint.2003.12.046.

[55] A. Stergiou, P. Tsakiropoulos, and A. Brown. The intermediate and high-temperature oxidation behaviour of $Mo(Si_{1-x}Al_x)_2$ intermetallic alloys. *Intermetallics*, 5(1):69–81, 1997. doi: 10.1016/S0966-9795(96)00068-4.

[56] C. E. Ramberg and W. L. Worrell. Oxidation Kinetics and Composite Scale Formation in the System $Mo(Al,Si)_2$. *Journal of the American Ceramic Society*, 85(2):444–452, 12 2004. doi: 10.1111/j.1151-2916.2002.tb00109.x.

[57] K. Yanagihara, K. Przybylski, and T. Maruyama. The Role of Microstructure on Pesting During Oxidation of $MoSi_2$ and $Mo(Si,Al)_2$ at 773 K. Technical report, 1997.

[58] R. Mitra, V. V. Rama Rao, and A. Venugopal Rao. Effect of small aluminum additions on microstructure and mechanical properties of molybdenum di-silicide. *Intermetallics*, 7(2):213–232, feb 1999. doi: 10.1016/S0966-9795(98)00064-8.

[59] M. Halvarsson, T. Jonsson, L. Ingemarsson, M. Sundberg, J. E. Svensson, and L. G. Johansson. Microstructural investigation of the initial oxidation at 1450 °C and 1500 °C of a $Mo(Si,Al)_2$-based composite. *Materials at High Temperatures*, 26(2):137–143, 2009. doi: 10.3184/096034009X464195.

[60] L. Ingemarsson, K. Hellström, L. G. Johansson, J. E. Svensson, and M. Halvarsson. Oxidation behaviour of a $Mo(Si,Al)_2$ based composite at

1500 °C. *Intermetallics*, 19(9):1319–1329, 9 2011. doi: 10.1016/j.intermet.2011.05.002.

[61] F. Liu, H. Götlind, J.E. Svensson, L.G Johansson, and M. Halvarsson. TEM investigation of the microstructure of the scale formed on a FeCrAlRE alloy at 900 °C: The effect of Y-rich RE particles. *Oxidation of Metals*, 74(1-2):11–32, 8 2010. doi: 10.1007/s11085-010-9195-5.

[62] P. Y. Hou. Beyond the Sulfur Effect. *Oxidation of Metals*, 52:337–351, 1999.

[63] A. Strawbridge and P. Y. Hou. The role of reactive elements in oxide scale adhesion. *Materials at High Temperatures*, 12(2-3):177–181, 1994. doi: 10.1080/09603409.1994.11689484.

[64] Gleeble 3800-GTC. https://www.gleeble.com/products/gleeble-systems/gleeble-3800.html. Accessed: 2021-12-12.

[65] J.I. Goldstein, D. E. Newbury, J. R. Michael, N. W. M. Ritchie, J. H. J. Scott, and D. C. Joy. *Scanning Electron Microscopy and X-Ray Microanalysis*. Springer, New York, NY, 4 edition, 2018. doi: 10.1007/978-1-4939-6676-9.

[66] GIMP - Gnu Image Manipulating Program. https://www.gimp.org.

[67] W.S. Rasband. ImageJ. https://imagej.nih.gov/ij/.

[68] D. B. Williams and C. B Carter. *Book on Electron Microscopy*, volume 53. 2013. doi: 10.1017/CBO9781107415324.004.

[69] A. Arsenlis and D. M. Parks. Crystallographic aspects of geometrically-necessary and statistically-stored dislocation density. *Acta Materialia*, 47(5):1597–1611, 1999. doi: 10.1016/S1359-6454(99)00020-8.

[70] MTEX Toolbox. https://mtex-toolbox.github.io/.

[71] GJ Zhang and XM Yue. In situ synthesis of $Mo(Si,Al)_2$-SiC composites. *Journal of materials science*, 35:4729–4733, 2000.

[72] Erwin Parthe and Wolfhart Rieger. Nowotny Phases and Apatites: A Comparative Study. *Journal of Dental Research*, 47(5):829–835, 1968.

[73] D.A. Hardwick and P.L. Martin. Microcracking, strain rate and large strain deformation effects in molybdenum disilicide. In *MRS Proceedings: Silicides and Refractory Metals*, 1993.

[74] Brandt J. Ruszkiewicz, Laine Mears, and John T. Roth. Investigation of Heterogeneous Joule Heating as the Explanation for the Transient Electroplastic Stress Drop in Pulsed Tension of 7075-T6 Aluminum. *Journal of Manufacturing Science and Engineering, Transactions of the ASME*, 140(9):1–11, 2018.

[75] A. Majumdar, J. P. Carrejo, and J. Lai. Thermal imaging using the atomic force microscope. *Applied Physics Letters*, 62(20):2501–2503, 1993.

[76] Rong Fan, James Magargee, Ping Hu, and Jian Cao. Influence of grain size and grain boundaries on the thermal and mechanical behavior of 70/30 brass under electrically-assisted deformation. *Materials Science and Engineering A*, 574:218–225, 2013.

[77] A. Nicolaÿ, J. M. Franchet, J. Cormier, R. E. Logé, G. Fiorucci, J. Fausty, M. Van Der Meer, and N. Bozzolo. Influence of Joule Effect Heating on Recrystallization Phenomena in Inconel 718. *Metallurgical and Materials Transactions A: Physical Metallurgy and Materials Science*, 52(10):4572–4596, 2021.

[78] J J Petrovic and R E Honnell. SiC Reinforced-$MoSi_2$/WSi_2 Alloy Matrix Composites. In *Ceramic Engineering and Science Proceedings*, volume 11, pages 734–744, 1990.

[79] Y. Liu, G. Shao, and P. Tsakiropoulos. Thermodynamic reassessment of the Mo-Si and Al-Mo-Si systems. *Intermetallics*, 2000. doi: 10.1016/S0966-9795(00)00068-6.

[80] Norbert Ponweiser, Werner Paschinger, Anna Ritscher, Julius C. Schuster, and Klaus W. Richter. Phase equilibria in the Al–Mo–Si system. *Intermetallics*, 19:409–418, mar 2011.

[81] Danqing Yi, Zonghe Lai, Changhai Li, Om Akselsen, and JH Ulvensoen. Ternary Alloying Study of $MoSi_2$. *Metallurgical and Materials Transactions A*, 29A:119—-129, 1998.

[82] Erik Ström. *Role of alloying elements in Mo5Si3 intermetallics Role of alloying elements in Mo_5Si_3 intermetallics Department of Materials Science and Engineering*. PhD thesis, Chalmers University of Technology, 2004.

[83] E. Ström. Mechanical properties of Mo_5Si_3 intermetallics as a function of composition. *Materials Characterization*, 55(4-5):402–411, nov 2005. doi: 10.1016/j.matchar.2005.09.001.

[84] K. Ito, T. Yano, T. Nakamoto, H. Inui, and M. Yamaguchi. Plastic deformation of single crystals of WSi_2 with the $C11_b$ structure. *Acta Materialia*, 47(3):937–949, 1999.